UNIVERSITY OF CALIFORNIA,
IRVINE

Beyond the Random-Phase Approximation: Theory, Efficient Implementations, and Applications to Rare-Earth and Actinide Chemistry

DISSERTATION

submitted in partial satisfaction of the requirements
for the degree of

DOCTOR OF PHILOSOPHY

in Chemistry

by

Guo Chen

Dissertation Committee:
Professor Filipp Furche, Chair
Professor Kieron Burke
Professor William J. Evans

2019

TABLE OF CONTENTS

LIST OF FIGURES

LIST OF TABLES

LIST OF ABBREVIATIONS

2RDM	two-electron reduced density matrix
AC	adiabatic connection
AO	atomic orbital
AXK	approximate exact exchange
B3LYP	Becke 3-parameter, Lee–Yang–Parr functional
BSE	Bethe–Salpeter equation
CBS	complete basis set
CCD	coupled-cluster doubles
CCSD	coupled-cluster singles and doubles
COSMO	conductor-like screening model
DFT	density functional theory
ECP	effective core potential
EPR	electron paramagnetic resonance
ERI	electron repulsion integral
FDT	fluctuation–dissipation theorem
GGA	generalized gradient approximation
HOMO	highest occupied molecular orbital
KS	Kohn–Sham
LUMO	lowest unoccupied molecular orbital
MAE	mean absolute error
ME	mean error
MLCT	metal-to-ligand charge transfer
MO	molecular orbital
MP2	second-order Møller–Plesset perturbation theory
MXE	maximum absolute error
PBE	Perdew–Burke–Ernzerhof functional
PBE0	PBE hybrid functional with 25% exact exchange
QZVPP	quadruple-zeta valence plus double polarization
RI	resolution-of-the-identity
RPA	random-phase approximation
SOSEX	second-order screened exchange
SOX	second-order exchange
STLS	Singwi–Tosi–Land–Sjölander
SVP	split valence plus polarization
SVPD	split valence with polarization and diffuse functions
SV(P)	split valence with polarization on non-hydrogen atoms
TDDFT	time-dependent density functional theory
TDKS	time-dependent Kohn–Sham
THF	tetrahydrofuran

TPSS	Tao–Perdew–Staroverov–Scuseria functional
TPSSh	TPSS hybrid functional with 10% exact exchange
TZVP	triple-zeta valence plus polarization
UV	ultraviolet
UV/vis/NIR	UV/visible/near-infrared
XC	exchange–correlation

ACKNOWLEDGMENTS

I would like to thank all the students, postdocs, and alumni of the Furche group. Brandon Krull, Jordan Vincent, Jefferson Bates, and Asbjörn Burow, you guys are partly the reason why I joined UCI and the Furche group, and it is a wonderful choice. Sree Balasubramani, Saswata Roy, Matthew Agee, Nambi Mohanam, Brian Nguyen, Jason Yu, Alan Chan, Alex Le, Kimberly Zhang, Jasper Hu, Johnny Choi, Mikko Muuronen, Shane Parker, Vamsee Voora, Eva von Domaros, and Enrico Tapavicza, I want to express my deepest gratitude to all of you for your continued support and inspiration. And thank you, Prof. Filipp Furche, for being a great mentor and role model.

I would like to thank the Burke group, particularly Li Li, Raphael Ribeiro, Justin Smith, Aurora Pribram-Jones, Miles Stoudenmire, Francisca Sagredo, Ryan McCarty, David Feinblum, Thomas Baker, and Attila Cangi. I really enjoyed the conversations we had about DFT and physics in general. My interactions with you all are not just "local effects." I would like to thank Prof. Antonio Cancio, with whom I collaborated on the asymptotically corrected GGA project. I want to especially thank Prof. Kieron Burke for paying for the flights when I first visited UCI from China and for your guidance and enlightenment.

I also want to thank the Evans group. Our collaborations have led to many exciting discoveries. The discussions, meetings, and email conversations we had are of tremendous help to me. I would not be able to think like a real chemist without our collaborations. I would like to thank David Woen, Cory Windorff, Ryan Langeslay, Chad Palumbo, Megan Dumas, Samuel Moehring, Dan Huh, Austin Ryan, and Megan Fieser. The outstanding works from you all have been a source of inspiration for me. Special thanks to Prof. William Evans. You are one of the best chemists that I have ever met. It is a great experience of mine to learn from you and work with you.

Many thanks to all my other collaborators, particularly to Dr. Andrew Gaunt and Dr. Stosh Kozimor. Even though we have never met in person, I have learned a lot from you two through all the revisions we had.

As a developer of Turbomole, I would like to thank the developer community and TURBOMOLE GmbH for support and traveling opportunities. In particular, I want to show my gratitude to Dr. Uwe Huniar for his service.

I am grateful to all the professors that I have taken courses from, Prof. Ioan Andricioaei, Prof. Shaul Mukamel, Prof. Douglas Tobias, Prof. Steven White, Prof. Patrick Guidotti, Prof. Craig Martens, Prof. Abel Klein, and of course, Prof. Filipp Furche, Prof. Kieron Burke, and Prof. William Evans.

The Department of Chemistry has been very supportive during my PhD study. Thank you to all the staff, particularly Tenley Dunn, Jaime Albano, Jenny Du, and Dr. Nathan Crawford. I really appreciate the wonderful working environment created by you all. Thanks are also due to the many professors that has helped me over the years, including Prof. Sergey

Nizkorodov, Prof. Rachel Martin, Prof. Vladimir Mandelshtam, and Prof. Ara Apkarian.

I have been financially supported by the Department of Chemistry, the National Science Foundation, and the Regents' Dissertation Fellowship. I also received travel grants from the School of Physical Sciences and from UCI Associated Graduate Students. I would like to thank all the funding sources.

I am lucky to have met many other friends in Irvine: Fan Liu, Qi Shi, Lianxi Cheng, Yiheng Qiu, Yunning Yang, Joel Langford, Wanyi Li, Chengcen Sha, Ming Gu, Andrew Geragotelis, Ilya Vinogradov, Li Xiao, Omar Hamido, and Guilherme Matos, thank you all. Many thanks to friend from my badminton club, Rui Wang, Wanxin Yue, Kiam Tey, Chee Lim, and Karin Lim. I am also indebted to all the people that helped me when, or even before, I first arrived in Irvine. Thank you, Hanxiang Zeng, Yu Zhang, and Zhenfei Liu.

I would like to thank my uncle and aunt, Cheng Chih and Terri Yang. It is lucky of me to have families nearby. Thank you for your kind help and guidance. And my parents, Li Chen and Yu Wang, I cannot thank you enough for your unconditional love and support. I also want to thank my girlfriend, Yi Li. Having met you is one of the best things that happened to me during my years at UCI. Your love and encouragement have made me a better person.

This dissertation contains verbatim excerpts as they appear in *Annu. Rev. Phys. Chem.*, *J. Chem. Theory Comput.*, *J. Am. Chem. Soc.*, and *Angew. Chem. Int. Ed.*. Permission to use copyrighted material in the dissertation has been grant by 2017 Annual Reviews, 2017 John Wiley & Sons, Inc., and 2017 & 2018 American Chemical Society. The co-authors listed in these publications directed, supervised, or conducted part of the research which forms the basis for the dissertation.

CURRICULUM VITAE

Guo Chen

EDUCATION

Doctor of Philosophy in Chemistry — **Mar. 2019**
University of California — *Irvine, California*

Master of Science in Chemistry — **Jul. 2013**
Tsinghua University — *Beijing, China*

Bachelor of Science in Chemistry — **Jul. 2010**
Tsinghua University — *Beijing, China*

REFEREED JOURNAL PUBLICATIONS

Using Diamagnetic Yttrium and Lanthanum Complexes to Explore Ligand Reduction and C-H Bond Activation in a Tris(Aryloxide)Mesitylene Ligand System
C. T. Palumbo, D. P. Halter, V. K. Voora, G. P. Chen, J. W. Ziller, M. Gembicky, A. L. Rheingold, F. Furche, K. Meyer, W. J. Evans
Inorg. Chem., 57:12876, **2018**

Performance and Scope of Perturbative Corrections to Random-Phase Approximation Energies
G. P. Chen, M. M. Agee, F. Furche
J. Chem. Theory Comput., 14:5701, **2018**

Fitting a Round Peg into a Round Hole: Asymptotically Correcting the Generalized Gradient Approximation for Correlation
A. Cancio, G. P. Chen, B. T. Krull, K. Burke
J. Chem. Phys., 149:084116, **2018**

Synthesis, Structure, and Magnetism of Tris(Amide) $[Ln\{N(SiMe_3)_2\}_3]^{1-}$ Complexes of the Non-Traditional +2 Lanthanide Ions
A. J. Ryan, L. E. Darago, S. G. Balasubramani, G. P. Chen, J. W. Ziller, F. Furche, J. R. Long, W. J. Evans
Chem. Eur. J., 24:7702, **2018**

Metal versus Ligand Reduction in Ln^{3+} Complexes of a Mesitylene-Anchored Tris(Aryloxide) Ligand
C. T. Palumbo, D. P. Halter, V. K. Voora, G. P. Chen, A. K. Chan, M. E. Fieser, J. W. Ziller, W. Hieringer, F. Furche, K. Meyer, W. J. Evans
Inorg. Chem., 57:2823, **2018**

Synthesis and Reductive Chemistry of Bimetallic and Trimetallic Rare-Earth Metallocene Hydrides with $(C_5H_4SiMe_3)^{1-}$ Ligands
M. T. Dumas, G. P. Chen, J. Y. Hu, M. A. Nascimento, J. M. Rawson, J. W. Ziller, F. Furche, W. J. Evans
J. Organomet. Chem., 849–850:38, **2017**

End-On Bridging Dinitrogen Complex of Scandium
D. H. Woen, G. P. Chen, J. W. Ziller, T. J. Boyle, F. Furche, W. J. Evans
J. Am. Chem. Soc., 139:14861, **2017**

Random-Phase Approximation Methods
G. P. Chen, V. K. Voora, M. M. Agee, S. G. Balasubramani, F. Furche
Annu. Rev. Phys. Chem., 68:421, **2017**

Identification of the Formal +2 Oxidation State of Plutonium: Synthesis and Characterization of $\{Pu^{II}[C_5H_3(SiMe_3)_2]_3\}^-$
C. J. Windorff, G. P. Chen, J. N. Cross, W. J. Evans, F. Furche, A. J. Gaunt, M. T. Janicke, S. A. Kozimor, B. L. Scott
J. Am. Chem. Soc., 139:3970, **2017**

Synthesis, Structure, and Reactivity of the Sterically Crowded Th^{3+} Complex $(C_5Me_5)_3Th$ Including Formation of the Thorium Carbonyl, $[(C_5Me_5)_3Th(CO)][BPh_4]$
R. R. Langeslay, G. P. Chen, C. J. Windorff, A. K. Chan, J. W. Ziller, F. Furche, W. J. Evans
J. Am. Chem. Soc., 139:3387, **2017**

Solution Synthesis, Structure, and CO_2 Reduction Reactivity of a Scandium(II) Complex, $\{Sc[N(SiMe_3)_2]_3\}^-$
D. H. Woen, G. P. Chen, J. W. Ziller, T. J. Boyle, F. Furche, W. J. Evans
Angew. Chem. Int. Ed., 56:2050, **2017**

Bonding Trends across the Series of Tricarbonato-Actinyl Anions $[(AnO_2)(CO_3)_3]^{4-}$ (An = U-Cm): The Plutonium Turn
J-B Liu, G. P. Chen, H. Huang, D. L. Clark, W. H. E. Schwarz, J. Li
Dalton Trans., 46:2542, **2017**

Quadruple Bonding of Carbon in Terminal Carbides
Y. Qiu, H. Hu, G. Chen, J. Li
Sci. China Chem., 57:426, **2014**

CONFERENCE TALKS

Efficient Implementation of the Approximate Exchange Kernel Method **Mar. 2018**
American Physical Society March Meeting, Los Angeles, California

Cubic Scaling Random Phase Approximation **Jun. 2015**
Recent Advances in Electronic Structure Theory, Nanjing, China

Theoretical Investigation of Nuclear Magnetic Shieldings in Uranyl Carbonate Complex Ions **Oct. 2012**
1st International Workshop on Theoretical Aspects of Advanced Nuclear Fuels, Beijing, China

POSTER PRESENTATIONS

Low-Scaling Algorithms for the Approximate Exchange Kernel Method **Jun. 2018**
Low-scaling and Unconventional Electronic Structure Techniques, Telluride, Colorado

Low-Scaling Algorithms for the Approximate Exchange Kernel Method **May 2018**
3rd Annual Southern California Theoretical Chemistry Symposium, Pasadena, California

Computational Study of Rare-Earth and Actinide Complexes with Unconventional Oxidation States **May 2017**
2nd Annual Southern California Theoretical Chemistry Symposium, Irvine, California

Computational Study of Transuranic Actinides with +2 Oxidation State **Mar. 2016**
251st American Chemical Society National Meeting, San Diego, California

Cubic Scaling Random Phase Approximation **Jun. 2015**
15th International Congress of Quantum Chemistry, Beijing, China

Cubic Scaling Random Phase Approximation **Jun. 2014**
Low-scaling and Unconventional Electronic Structure Techniques, Telluride, Colorado

TEACHING EXPERIENCE

Time-Dependent Density Functional Theory (Chem 254) **Spring 2017**
University of California *Irvine, California*

Electron Correlation in Molecules (Chem 254) **Winter 2017**
University of California *Irvine, California*

Molecular Quantum Mechanics (Chem 235) **Winter 2015**
University of California *Irvine, California*

Classical Mechanics and Electromagnetic Theory (Chem 230) **Fall 2014**
University of California *Irvine, California*

Honors General Chemistry (Chem H2B) **Winter 2014**
University of California *Irvine, California*

General Chemistry Laboratory (Chem 1LD) **Fall 2013**
University of California *Irvine, California*

Introduction to Computational Chemistry **Fall 2012**
Tsinghua University *Beijing, China*

Introduction to Computational Chemistry **Fall 2011**
Tsinghua University *Beijing, China*

HONORS AND AWARDS

Regents' Dissertation Fellowship **2018**
University of California *Irvine, California*

Tsinghua Scholarship for Academic Excellence **2009**
Tsinghua University *Beijing, China*

CNPC Scholarship **2008**
Tsinghua University *Beijing, China*

Kwang-Hua Scholarship **2007**
Tsinghua University *Beijing, China*

ABSTRACT OF THE DISSERTATION

Beyond the Random-Phase Approximation: Theory, Efficient Implementations, and Applications to Rare-Earth and Actinide Chemistry

By

Guo Chen

Doctor of Philosophy in Chemistry

University of California, Irvine, 2019

Professor Filipp Furche, Chair

The random-phase approximation (RPA) incorporates many appealing features absent in semilocal density functional theory (DFT) without excessively increasing computational cost. The first half of this thesis addresses the question: Can one achieve a similar balance between accuracy and speed for beyond-RPA corrections? To this end, low-scaling algorithms are developed for the most common perturbative corrections to RPA, including the bare second-order exchange (SOX), second-order screened exchange (SOSEX), and approximate exchange kernel (AXK) methods. The implementations are based on the resolution-of-the-identity (RI) approximation, Clenshaw–Curtis numerical frequency quadrature, and optionally, integral prescreening. These implementations afford benchmark calculations on medium- and large-size molecules with size-independent accuracy. The benchmark results show that the AXK method systematically improves RPA and surpasses SOX and SOSEX for reaction barrier heights, reaction energies, and noncovalent interaction energies of main-group compounds, confirming conclusions drawn from previous small-molecule calculations. The superior accuracy of AXK compared with SOX and SOSEX suggests that the strong screening of bare SOX in AXK is important. Nevertheless, benchmark calculations on $3d$ transition metal compounds show that RPA and its perturbative corrections eventually break down for systems with strong static correlation, such as metal dimers. The reliability

of RPA methods can be estimated using an effective coupling strength $\bar{\alpha}$ proposed herein. The second half of the thesis demonstrates the use of electronic structure methods for the identification and characterization of $\{Sc[N(SiMe_3)_2]_3\}^-$, $\{[(R_2N)_3Sc]_2[\mu\text{-}\eta^1\text{:}\eta^1\text{-}N_2]\}^{2-}$, and $\{Pu[C_5H_3(SiMe_3)_2]_3\}^-$: DFT and time-dependent DFT calculations played an important role in characterizing the electron configurations, bonding, and UV-visible spectroscopy of these unconventional rare-earth and actinide compounds. The applicability of RPA and AXK to these compounds is assessed, using the Pu^{2+} complex as an example.

Chapter 1

Background and Theory

This chapter contains verbatim excerpts, reprinted with permission, from G. P. Chen, V. K. Voora, M. M. Agee, S. G. Balasubramani, and F. Furche, *Annu. Rev. Phys. Chem.* **68**, 421–445, 2017. Copyright 2017 Annual Reviews. Section 1.5 also contains verbatim excerpts, reprinted with permission, from G. P. Chen, M. M. Agee, and F. Furche, *J. Chem. Theory Comput.* **14**, 5701–5714, 2018. Copyright 2018 American Chemical Society. This material is based upon work supported by the National Science Foundation under CHE-1213382, CHE-1464828, and CHE-1800431.

1.1 Introduction

Density functional theory (DFT) with semilocal and hybrid approximations is the most broadly applied electronic structure method to date, owing to its semiquantitative accuracy and modest computational cost [1–3]. The reliability of semilocal approximations partially depends on the cancellation of error between their exchange and correlation parts [4, 5]. However, this cancellation breaks down for systems with significant static correlation such as dissociating closed-shell molecules [6]. Moreover, due to the exponential decay of the density, semilocal functionals cannot account for long-range dispersion interactions, which decays polynomially. Empirical corrections developed by Grimme and co-workers [7, 8] provide a remedy to this problem, but the system under consideration is artificially partitioned into atoms.

Modern random-phase approximation (RPA) in the context of DFT [9–12] provides an alternative to semilocal approximations. Formulated within the framework of adiabatic-connection fluctuation–dissipation theorem [13, 14], the RPA correlation energy functional is compatible with the exact exchange. RPA is robust for small- and zero-gap systems and is accurate for the uniform electron gas in the high-density or weak-coupling limit [15, 16]. It even partially accounts for static correlation within the spin-restricted formalism [6, 17, 18]. The RPA correlation energy also captures the leading contributions to mid- and long-range dispersion interactions without ad hoc partitioning the system [19, 20]. RPA has received increasing attention recently, largely due to the advent of fast and robust implementations [21, 22]. From a correlated wavefunction theory perspective, these implementations afford low-scaling computation of a simplified coupled-cluster doubles (CCD) correlation energy without explicitly computing the amplitudes [23, 24]. Using the RPA implementation in Turbomole [25], molecules with well over 100 atoms and large basis sets can be routinely computed on a single workstation computer (see, e.g., [26]). Benchmark calculations for molecules of various sizes are thus possible [10, 26, 27]. RPA has shown good performance

for energetics such as noncovalent interaction energies, reaction barrier heights, and energies of reactions that conserve the numbers of electron pairs [10, 28], gaining popularity in both method development and applications.

RPA was first developed by Bohm and Pines in the early 1950s for the uniform electron gas as an approximation to decouple long-range plasma oscillations and screened quasi-electrons [29–32]. In 1957, Gell-Mann and Brueckner computed the correlation energy of the uniform electron gas by summing over the most divergent terms in each order of the many-body perturbation theory [15]. The two approaches are equivalent in the high-density limit, so the Gell-Mann–Brueckner method became synonymous with RPA and was generalized to nonuniform systems. RPA may also be derived from the quasi-boson approximation [16, 33], Green's function or propagator methods [34–36], and the equation-of-motion method [37], yet most modern implementations of RPA follows the formalism within adiabatic-connection DFT introduced by Langreth and Perdew in the 1970s [13, 14]. The multifaceted origin of RPA offers different conceptual understandings thereof, which in turn may inspire improvements from various perspectives.

The description of electron correlation from RPA is not accurate across all interaction ranges. Particularly, RPA suffers from self-correlation and unphysical pair density at short electron separations [38], which lead to overestimation of the magnitudes of correlation energies and poor performance for energetics of processes where short-range electron–electron interactions change significantly, e.g., ionization and atomization [10]. The leading correction to RPA is the bare second-order exchange (SOX), which was included in Gell-Mann and Brueckner's calculation for the uniform electron gas [15]. However, as a perturbative correction with respect to the Kohn–Sham (KS) noninteracting system, SOX is sensitive to the KS HOMO-LUMO gap and tends to overcorrect RPA. Renormalized perturbative corrections such as second-order screened exchange (SOSEX) [23, 39–41] and approximate exchange kernel (AXK) [42] methods correctly recover SOX and also contain higher-order corrections due

to screening. Particularly, benchmark calculations show that AXK systematically corrects RPA for small molecules [42]. Nevertheless, the absence of fast and robust implementations has hindered further assessment of AXK and the other perturbative RPA correction methods for larger molecules in the past.

The purpose of this thesis is twofold: The first is to develop efficient and robust implementations of beyond-RPA perturbative corrections, including the SOX, SOSEX, and AXK methods, and to assess their accuracies using benchmarks containing medium- and large-size molecules. The second is to show the role of electronic structure calculations in the discoveries of unconventional rare-earth and actinide complexes and to suggest the usefulness of RPA methods for these systems.

The thesis is organized as follows. Chapter 1 introduces the necessary theoretical background for RPA methods, with an emphasis on the theoretical framework, the physical picture, and approximation methods for low-scaling implementations. Chapter 2 focuses on algorithmic development and implementations of fast computations of beyond-RPA perturbative corrections. Detailed error analyses and benchmark results are reported, showing the systematic improvement of AXK over RPA independent of system size. Cases where RPA and its perturbative corrections fail are identified, and an effective coupling strength is proposed to indicate reliability of RPA and AXK results. Chapter 3 presents three discoveries of non-traditional rare-earth and actinide compounds from a computational perspective: The first isolable Sc^{2+} and Pu^{2+} complexes, and the end-on bridging dinitrogen complex of Sc^{3+}. Remarks on the validity of RPA and AXK for these systems are provided.

1.2 Theory

1.2.1 Adiabatic Connection

The adiabatic connection (AC) uses a single coupling strength parameter α to switch continuously from the noninteracting KS system [43] ($\alpha = 0$) to the physical many-electron system of interest ($\alpha = 1$). A key aspect of the AC that distinguishes it from other deformations of the physical system is the constraint that the ground-state density be equal to the physical ground-state density ρ for all α. The AC Hamiltonian is thus [13, 44]

$$\hat{H}_\alpha[\rho] = \hat{T} + \hat{V}_\alpha[\rho] + \alpha\hat{V}_{\mathrm{ee}}, \tag{1.1}$$

where $\hat{T}$ is the electron kinetic energy operator, $\hat{V}_\alpha[\rho]$ is the sum over electron indices of the one-electron local potential operator $\hat{v}_\alpha[\rho]$ uniquely determined (up to a constant, if existence is established) by the density constraint [45], and $\hat{V}_{\mathrm{ee}}$ is the operator of the electron–electron Coulomb interaction. Atomic (Hartree) units are used throughout this thesis, i.e., the electron mass, the elementary charge, and reduced Planck's constant are set to unity. By construction, $\hat{v}_\alpha[\rho]$ turns into the external potential for $\alpha = 1$ and into the KS potential for $\alpha = 0$. Moreover, the ground-state wavefunction Ψ_α becomes the KS determinant Φ at zero coupling strength.

The energy of the physical ground state E is the sum of the energy expectation value of the KS determinant and the correlation energy,

$$E = \langle\Phi|\hat{H}|\Phi\rangle + E^{\mathrm{C}}. \tag{1.2}$$

This definition of the correlation energy is appropriate in a density functional context, whereas the traditional definition in wavefunction theory uses the HF determinant [46].

Using the density constraint, the AC correlation energy may be recast as a coupling strength integral [13, 44]:

$$E^{\mathrm{C}}[\rho] = \int_0^1 \mathrm{d}\alpha \big(\langle \Psi_\alpha[\rho] \,|\, \hat{V}_{\mathrm{ee}} \,|\, \Psi_\alpha[\rho] \rangle - \langle \Phi[\rho] \,|\, \hat{V}_{\mathrm{ee}} \,|\, \Phi[\rho] \rangle \big). \tag{1.3}$$

Equation (1.3) expresses the correlation energy entirely as an expectation value of the electron–electron Coulomb repulsion $\hat{V}_{\mathrm{ee}}$; the coupling strength integration accounts for the kinetic correlation energy.

1.2.2 Fluctuation–Dissipation Theorem

The zero-temperature fluctuation–dissipation theorem (FDT) relates ground-state fluctuations to dissipation in the linear response regime [47]. Because electron correlation is related to ground-state density fluctuations [10], the FDT may be used to express the correlation energy as [13, 14]

$$E^{\mathrm{C}}[\rho] = -\frac{1}{2\pi} \int_0^1 \mathrm{d}\alpha \, \Im \int_0^\infty \mathrm{d}\omega \int \mathrm{d}x \, \mathrm{d}x' \, \frac{\chi_\alpha(\omega, x, x') - \chi_0(\omega, x, x')}{|\mathbf{r} - \mathbf{r}'|}, \tag{1.4}$$

where ω denotes frequency and $x = (\mathbf{r}, \sigma)$ space–spin coordinates; χ_α is the frequency-dependent linear density–density response function at coupling strength α,

$$\chi_\alpha(\omega, x, x') = \left. \frac{\delta \rho(\omega, x)}{\delta v(\omega, x')} \right|_{v(\omega,\cdot) = v_\alpha[\rho]} \tag{1.5}$$

A striking feature of Equation (1.4) is that the correlation energy is expressed in terms of one-electron linear response properties, which are accessible from time-dependent perturbation theory and have been well studied because of their importance, e.g., for spectroscopy.

1.2.3 Time-Dependent Density Functional Theory

Computing the ground-state correlation energy from the FDT still requires knowledge of the density–density response function at each coupling strength $0 \leqslant \alpha \leqslant 1$. TDDFT [48, 49] provides a conceptually and computationally simple avenue: χ_α may be obtained from the time-dependent KS (TDKS) system instead of the interacting system because their time-dependent densities are the same by construction. Thus, $\chi_\alpha(\omega, x_1, x_2)$ is the diagonal of the TDKS density-matrix–density-matrix response function $\Pi^{\mathrm{s}}_\alpha(\omega, x_1, x_1', x_2, x_2')$ in real space,

$$\chi_\alpha(\omega, x_1, x_2) = \Pi^{\mathrm{s}}_\alpha(\omega, x_1, x_1, x_2, x_2), \tag{1.6}$$

just as the interacting time-dependent density is the diagonal of the TDKS (one-electron) density matrix.

The TDKS density-matrix–density-matrix response function, or retarded polarization propagator, may be represented by a supermatrix $\mathbf{\Pi}^{\mathrm{s}}_\alpha(\omega)$ of dimension $2N_{\mathrm{h}}N_{\mathrm{p}} \times 2N_{\mathrm{h}}N_{\mathrm{p}}$, where N_{h} and N_{p} denote the numbers of occupied (hole) and virtual (particle) orbitals, respectively [50]. The physical picture is clear for the bare KS polarization propagator $\mathbf{\Pi}_0$, which equals $\mathbf{\Pi}^{\mathrm{s}}_\alpha$ at zero coupling strength: A perturbation at the frequency of a pole of $\mathbf{\Pi}_0$ excites an electron from a KS occupied orbital ϕ_i to a virtual orbital ϕ_a. In the particle–hole picture, the electron is excited from the KS reference state, or Fermi vacuum, leaving behind a positively charged hole below the Fermi level and creating a negatively charged electron or particle above the Fermi level. The resulting KS particle–hole pair is described by the orbital product $\phi_i(x)\phi_a(x')$, whose diagonal, known as the zeroth-order transition density, integrates to zero because the excitation conserves the total electron number. Throughout this thesis, indices $i, j, \ldots$ denote occupied (hole), $a, b, \ldots$ virtual (particle), and $p, q, \ldots$ general KS molecular orbitals. All orbitals are assumed to be real.

Density-matrix response theory yields an expression for the TDKS polarization propagator

familiar from time-dependent Hartree–Fock theory [51–53]:

$$\boldsymbol{\Pi}^{\mathrm{s}}_{\alpha}(\omega) = -\left[\begin{pmatrix} \mathbf{A}_{\alpha}(\omega) & \mathbf{B}_{\alpha}(\omega) \\ \mathbf{B}_{\alpha}(\omega) & \mathbf{A}_{\alpha}(\omega) \end{pmatrix} - (\omega + i\eta) \begin{pmatrix} \mathbf{1} & \mathbf{0} \\ \mathbf{0} & -\mathbf{1} \end{pmatrix} \right]^{-1}. \tag{1.7}$$

The $i\eta$ contour distortion makes $\boldsymbol{\Pi}^{\mathrm{s}}_{\alpha}$ analytic in the upper half of the complex frequency plane and thus guarantees causality [54]; the limit $\eta \to 0^{+}$ is taken after a possible frequency integration. $\mathbf{A}_{\alpha}(\omega)$ and $\mathbf{B}_{\alpha}(\omega)$ are the TDKS orbital rotation Hessians,

$$(A_{\alpha} + B_{\alpha})_{iajb}(\omega) = D_{iajb} + 2\alpha B^{\mathrm{H}}_{iajb} + 2B^{\mathrm{XC}}_{\alpha iajb}(\omega), \tag{1.8}$$

$$(A_{\alpha} - B_{\alpha})_{iajb}(\omega) = D_{iajb}, \tag{1.9}$$

where $\mathbf{D}$ is a $N_{\mathrm{h}}N_{\mathrm{p}} \times N_{\mathrm{h}}N_{\mathrm{p}}$ diagonal supermatrix whose diagonal elements are KS orbital energy differences,

$$D_{iajb} = (\epsilon_a - \epsilon_i)\delta_{ij}\delta_{ab}; \tag{1.10}$$

$\mathbf{B}^{\mathrm{H}}$ and $\mathbf{B}^{\mathrm{XC}}_{\alpha}$ are $N_{\mathrm{h}}N_{\mathrm{p}} \times N_{\mathrm{h}}N_{\mathrm{p}}$ supermatrices that describe the coupling between bare particle–hole pairs, where

$$B^{\mathrm{H}}_{iajb} = (ia|jb) = \int \mathrm{d}x_1 \, \mathrm{d}x_2 \, \phi_i(x_1)\phi_a(x_1) \frac{1}{|\mathbf{r}_1 - \mathbf{r}_2|} \phi_j(x_2)\phi_b(x_2) \tag{1.11}$$

is a four-center electron repulsion integral (ERI) in Mulliken notation, and

$$B^{\mathrm{XC}}_{\alpha iajb}(\omega) = \int \mathrm{d}x_1 \, \mathrm{d}x_2 \, \phi_i(x_1)\phi_a(x_1) f^{\mathrm{XC}}_{\alpha}(\omega, x_1, x_2)\phi_j(x_2)\phi_b(x_2) \tag{1.12}$$

is a frequency-dependent matrix element of the exchange–correlation (XC) kernel at coupling strength α; f^{XC}_{α} is the exchange–correlation kernel in real-space representation.

Equation (1.7) may be written in different forms emphasizing different physical aspects. Defining the supermatrices of the bare Coulomb or Hartree interaction and of the XC kernel, respectively, as

$$\mathbf{V} = \begin{pmatrix} \mathbf{B}^{\mathrm{H}} & \mathbf{B}^{\mathrm{H}} \\ \mathbf{B}^{\mathrm{H}} & \mathbf{B}^{\mathrm{H}} \end{pmatrix}, \qquad \mathbf{F}_{\alpha}^{\mathrm{XC}}(\omega) = \begin{pmatrix} \mathbf{B}_{\alpha}^{\mathrm{XC}}(\omega) & \mathbf{B}_{\alpha}^{\mathrm{XC}}(\omega) \\ \mathbf{B}_{\alpha}^{\mathrm{XC}}(\omega) & \mathbf{B}_{\alpha}^{\mathrm{XC}}(\omega) \end{pmatrix}, \tag{1.13}$$

we arrive at the Bethe–Salpeter equation (BSE) for $\mathbf{\Pi}_{\alpha}^{\mathrm{s}}$ [36, 55, 56]:

$$\mathbf{\Pi}_{\alpha}^{\mathrm{s}}(\omega) = \big(\mathbf{\Pi}_0(\omega)^{-1} - \alpha\mathbf{V} - \mathbf{F}_{\alpha}^{\mathrm{XC}}(\omega)\big)^{-1}, \tag{1.14}$$

or formally equivalently,

$$\mathbf{\Pi}_{\alpha}^{\mathrm{s}}(\omega) = \mathbf{\Pi}_0(\omega) + \mathbf{\Pi}_0(\omega)\big(\alpha\mathbf{V} + \mathbf{F}_{\alpha}^{\mathrm{XC}}(\omega)\big)\mathbf{\Pi}_{\alpha}^{\mathrm{s}}(\omega). \tag{1.15}$$

This form emphasizes the screening of $\mathbf{\Pi}_0$ resulting from Hartree and XC interactions. Alternatively, one may focus on the poles of $\mathbf{\Pi}_{\alpha}^{\mathrm{s}}$, which occur at excitation energies of the α-coupled interacting system. At these excitation energies, the inverse of $\mathbf{\Pi}_{\alpha}^{\mathrm{s}}$ becomes singular, leading to the TDKS eigenvalue problem:

$$\left[\begin{pmatrix} \mathbf{A}_{\alpha}(\Omega_{\alpha n}) & \mathbf{B}_{\alpha}(\Omega_{\alpha n}) \\ \mathbf{B}_{\alpha}(\Omega_{\alpha n}) & \mathbf{A}_{\alpha}(\Omega_{\alpha n}) \end{pmatrix} - \Omega_{\alpha n}\begin{pmatrix} \mathbf{1} & \mathbf{0} \\ \mathbf{0} & -\mathbf{1} \end{pmatrix}\right]\begin{pmatrix} \mathbf{X}_{\alpha n} \\ \mathbf{Y}_{\alpha n} \end{pmatrix} = \mathbf{0}, \quad \mathbf{X}_{\alpha n}^{\mathrm{T}}\mathbf{X}_{\alpha n} - \mathbf{Y}_{\alpha n}^{\mathrm{T}}\mathbf{Y}_{\alpha n} = 1. \tag{1.16}$$

For $\alpha = 1$, the eigenvalues equal electronic excitation energies of the physical system, and the eigenvectors yield the corresponding transition densities,

$$\rho_{0n}(x) = \sum_{ia}(\mathbf{X}_n + \mathbf{Y}_n)_{ia}\phi_i(x)\phi_a(x), \tag{1.17}$$

which is key for TDDFT applications to electronic spectroscopy [49].

Finally, the correlation energy may be expressed in terms of $\mathbf{\Pi}^{\mathrm{s}}_{\alpha}$,

$$E^{\mathrm{C}} = -\frac{1}{2\pi}\int_0^1 \mathrm{d}\alpha\, \Im \int_0^\infty \mathrm{d}\omega \big\langle \mathbf{V}\big(\mathbf{\Pi}^{\mathrm{s}}_{\alpha}(\omega) - \mathbf{\Pi}_0(\omega)\big)\big\rangle, \tag{1.18}$$

where angle brackets denote the trace operation. However, computation of $\mathbf{\Pi}^{\mathrm{s}}_{\alpha}$ requires knowledge of the XC kernel. As explained below, Equation (1.18) is more than a complicated reformulation of the problem that shifts the difficulty from the XC energy to the kernel; even the simplest approximation to $\mathbf{\Pi}^{\mathrm{s}}_{\alpha}$ captures important physics of the system at coupling strength α.

1.3 Random-Phase Approximation

1.3.1 Time-Dependent Density Functional Theory Perspective

Within RPA, the XC kernel in Equation (1.15) is set to zero; this is equivalent to the time-dependent Hartree approximation. Thus, $\mathbf{\Pi}^{\mathrm{s}}_{\alpha}$ is approximated by

$$\mathbf{\Pi}^{\mathrm{RPA}}_{\alpha}(\omega) = \mathbf{\Pi}_0(\omega) + \alpha\mathbf{\Pi}_0(\omega)\mathbf{V}\mathbf{\Pi}^{\mathrm{RPA}}_{\alpha}(\omega). \tag{1.19}$$

Defining the dimensionless generalized dielectric function [54] within RPA as

$$\boldsymbol{\kappa}^{\mathrm{RPA}}_{\alpha}(\omega) = \mathbf{1} - \alpha\mathbf{\Pi}_0(\omega)\mathbf{V}, \tag{1.20}$$

the BSE for $\mathbf{\Pi}^{\mathrm{RPA}}_{\alpha}$ (Equation (1.19)) becomes

$$\mathbf{\Pi}^{\mathrm{RPA}}_{\alpha}(\omega) = \big(\boldsymbol{\kappa}^{\mathrm{RPA}}_{\alpha}(\omega)\big)^{-1}\mathbf{\Pi}_0(\omega). \tag{1.21}$$

This affords an appealing physical interpretation: $\boldsymbol{\kappa}_\alpha^{\mathrm{RPA}}(\omega)$ accounts for screening of bare KS particle–hole pairs resulting from other induced particle–hole pairs, i.e., polarization, through the Hartree interaction. In other words, $\boldsymbol{\Pi}_\alpha^{\mathrm{RPA}}$ is dressed or renormalized by the interaction between particle–hole pairs. Alternatively, the effect of screening may be illustrated by defining the RPA effective interaction

$$\mathbf{V}_\alpha^{\mathrm{RPA}}(\omega) = \mathbf{V} + \alpha \mathbf{V} \boldsymbol{\Pi}_0(\omega) \mathbf{V}_\alpha^{\mathrm{RPA}}(\omega) = \mathbf{V} \big(\boldsymbol{\kappa}_\alpha^{\mathrm{RPA}}(\omega) \big)^{-1}. \tag{1.22}$$

Without screening, $\boldsymbol{\kappa}_0^{\mathrm{RPA}} = 0$, and $\mathbf{V}_\alpha^{\mathrm{RPA}}(\omega)$ reduces to the Hartree interaction, which is instantaneous. However, for finite α, $\mathbf{V}_\alpha^{\mathrm{RPA}}(\omega)$ acquires frequency dependence because of screening by induced particle–hole pairs.

To avoid the poles of the polarization propagators near the real axis, we may perform the frequency integration in Equation (1.18) along the imaginary axis using Cauchy's integral theorem [57]. Analytically integrating over the coupling strength then yields an expression for the RPA correlation energy solely in terms of the KS polarization propagator and the Hartree interaction [14]:

$$E^{\mathrm{C\ RPA}} = \frac{1}{2\pi} \int_0^\infty \mathrm{d}\omega \, \big\langle \ln\big(\mathbf{1} - \boldsymbol{\Pi}_0(i\omega) \mathbf{V} \big) + \boldsymbol{\Pi}_0(i\omega) \mathbf{V} \big\rangle. \tag{1.23}$$

For closed-shell systems at large separation, Equation (1.23) correctly reproduces the leading-order dispersion energy, thereby providing a generalization of dispersion interactions for systems of finite size (see References [19, 20]).

1.3.2 Plasmon Perspective

A particularly simple representation of the RPA correlation energy results from performing both the frequency and coupling strength integrations in Equation (1.18) analytically [58],

$$E^{\mathrm{C\ RPA}} = \frac{1}{2}\sum_{n}\left(\Omega_n^{\mathrm{RPA}} - \Omega_n^{\mathrm{RPA1}}\right); \tag{1.24}$$

here Ω_n^{RPA} and Ω_n^{RPA1} are the RPA electronic excitation energies and those up to first order in α, respectively, and the summation runs over all excitations. In the spirit of Bohm and Pines's work, the plasmon formula (Equation (1.24)) states that the RPA correlation energy is the difference between the zero-point energies of electronic excitations at full coupling and those up to first order in the electron interaction. In this picture, each excitation represents one harmonic degree of freedom. The sum in Equation (1.24) is dominated by excitations whose energies change most as the interaction is turned on; this is a key characteristic of plasmons [59]. Plasmons are long-wavelength oscillations of an electron gas and are highly collective, i.e., they involve oscillations of the entire electron gas and cannot be described by single KS particle–hole pairs or single-electron excitations.

The connection between the RPA correlation energy and collective excitations becomes especially clear by introducing the plasmonic Hessian $\mathbf{W}^{\mathrm{p}}$ and further rewriting Equation (1.24) as

$$E^{\mathrm{C\ RPA}} = -\frac{1}{2}\langle \mathbf{W}^{\mathrm{p}} \rangle = -\frac{1}{2}\sum_{n}\Omega_n^{\mathrm{p}}, \tag{1.25}$$

where Ω_n^{p} are the eigenvalues of $\mathbf{W}^{\mathrm{p}}$, and

$$\mathbf{W}^{\mathrm{p}} = -\Big((\mathbf{M}^{\mathrm{RPA}})^{1/2} - \mathbf{D} - \mathbf{T}\Big), \tag{1.26}$$

$$\mathbf{M}^{\mathrm{RPA}} = \mathbf{M}_\alpha^{\mathrm{RPA}}\big|_{\alpha=1}, \tag{1.27}$$

$$\mathbf{M}_\alpha^{\mathrm{RPA}} = (\mathbf{A}_\alpha^{\mathrm{RPA}} - \mathbf{B}_\alpha^{\mathrm{RPA}})^{1/2}\,(\mathbf{A}_\alpha^{\mathrm{RPA}} + \mathbf{B}_\alpha^{\mathrm{RPA}})(\mathbf{A}_\alpha^{\mathrm{RPA}} - \mathbf{B}_\alpha^{\mathrm{RPA}})^{1/2}. \tag{1.28}$$

$\mathbf{A}_\alpha^{\mathrm{RPA}}$ and $\mathbf{B}_\alpha^{\mathrm{RPA}}$ are the RPA orbital rotation Hessians; see Equations (1.8) and (1.9). $\mathbf{D}$ and $\mathbf{T}$ are, respectively, the zeroth- and first-order terms of $(\mathbf{M}_\alpha^{\mathrm{RPA}})^{1/2}$ with respect to α. It is shown in Appendix A that

$$T_{iajb} = \frac{2(\epsilon_a - \epsilon_i)^{1/2} B^{\mathrm{H}}_{iajb} (\epsilon_b - \epsilon_j)^{1/2}}{\epsilon_a - \epsilon_i + \epsilon_b - \epsilon_j} \tag{1.29}$$

and $\mathbf{W}^{\mathrm{p}}$ is positive definite. Typically, a few large eigenvalues of $\mathbf{W}^{\mathrm{p}}$ dominate the RPA correlation energy, and the corresponding eigenvectors may be interpreted as plasmonic modes describing collective excitations of the electrons that give rise to large zero-point energies.

We illustrate the plasmonic mode analysis of the RPA correlation energy for the tetrahedral Ag_{20} cluster [60] in Table 1.1 and Figure 1.1. The modes with the largest 10 eigenvalues make up over 90% of the total RPA correlation energy in a split valence plus polarization (SVP) atomic orbital (AO) basis (Table 1.1). Visualization of the modes (Figure 1.1) shows that those with the largest contributions to the correlation energy are highly collective, i.e., they involve oscillations of the entire electron cloud of the cluster. These collective modes have few nodes, in accord with the notion that plasmons are low-wavelength excitations. The plasmonic modes are poorly described by either KS single-orbital or RPA excitations, but they provide an efficient representation of the RPA correlation energy.

Table 1.1: Plasmonic modes of Ag_{20} with the 10 largest eigenvalues (in hartree) and their percentage contribution to $E^{\mathrm{C\ RPA}}$. def2-SVP basis set [61] along with scalar relativistic small-core pseudopotentials [62] were used; orbitals were generated using the TPSS functional [63] and quadrature grids of size m5 [64].

Mode	Eigenvalue	% of $E^{\mathrm{C\ RPA}}$
$1A_1$	0.2070	11.5
$2A_1$	0.1836	10.2
$3A_1$	0.1612	8.9
$4A_1$	0.1118	6.6
$1E$	0.1702	9.4
$1T_1$	0.1658	9.2
$1T_2$	0.1728	9.6
$2T_2$	0.1666	9.2
$3T_2$	0.1338	9.1
$4T_2$	0.1467	8.1

1.3.3 Diagrammatic Perspective

An alternative approach to the density–density response function χ_α uses the interacting polarization propagator $\mathbf{\Pi}_\alpha$ [50]. Although both $\mathbf{\Pi}_\alpha$ and the TDKS polarization propagator $\mathbf{\Pi}^{\mathrm{s}}_\alpha$ yield the same density–density response function and thus the same correlation energy through the FDT, the two are not equal [65]. $\mathbf{\Pi}_\alpha$ satisfies its own BSE [66],

$$\mathbf{\Pi}_\alpha(\omega) = \mathbf{\Pi}_0(\omega) + \mathbf{\Pi}_0(\omega)\big(\alpha\mathbf{V} + \mathbf{K}_\alpha(\omega)\big)\mathbf{\Pi}_\alpha(\omega), \tag{1.30}$$

where $\mathbf{K}_\alpha$ is a frequency-dependent kernel accessible, e.g., through many-body perturbation theory and Green's function methods [36, 54]. In this many-body theory approach, RPA amounts to neglecting $\mathbf{K}_\alpha$.

In keeping with the Feynman–Dyson diagrammatic approach [67, 68], polarization propagators and the Hartree interaction are represented by pairs of arrowed lines and horizontal wiggly lines, respectively (Figure 1.2*a*), and the BSE within RPA takes the form shown in Figure 1.2*b*. The RPA correlation energy can be represented by the bubble diagrams in Fig-

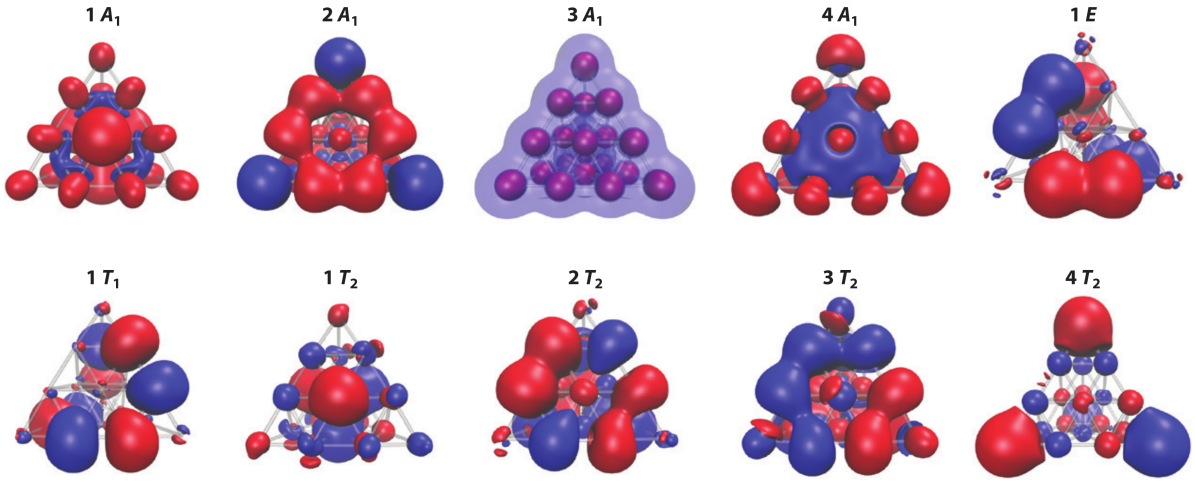

Figure 1.1: Contour plots of the 10 dominant plasmonic modes of Ag_{20}. Contour values of 0.001 (*red*) and −0.001 (*blue*) were used; only one column is shown for degenerate modes. For further details, see Table 1.1.

ure 1.2*c*, again suggesting a physical picture of vacuum fluctuations giving rise to correlation. Substituting Figure 1.2*b* into Figure 1.2*c* and integrating over coupling strength produces the series of ring diagrams first identified by Gell-Mann and Brueckner [15] (Figure 1.2*d*).

1.4 Kernel Corrections

The RPA is equivalent to the Hartree approximation for the TDDFT and BSE kernels, and thus lacks any second- or higher-order exchange. As a result, same-spin particle–hole pairs do not experience Pauli repulsion and are screened as much as opposite-spin particle–hole pairs. This makes the RPA on-top correlation hole too negative and leads to overcorrelation of electrons at short interelectron distances [38]. In other words, RPA contains spurious self-correlation error, which underlies, e.g., its failure to correctly dissociate odd-electron systems such as H_2^+ [42, 70]. The unphysical short-range behavior of RPA also explains its relatively poor performance for nonisogyric processes, such as atomization, ionization, and spin-flip processes, which break up electron pairs and lead to large changes in the short-range

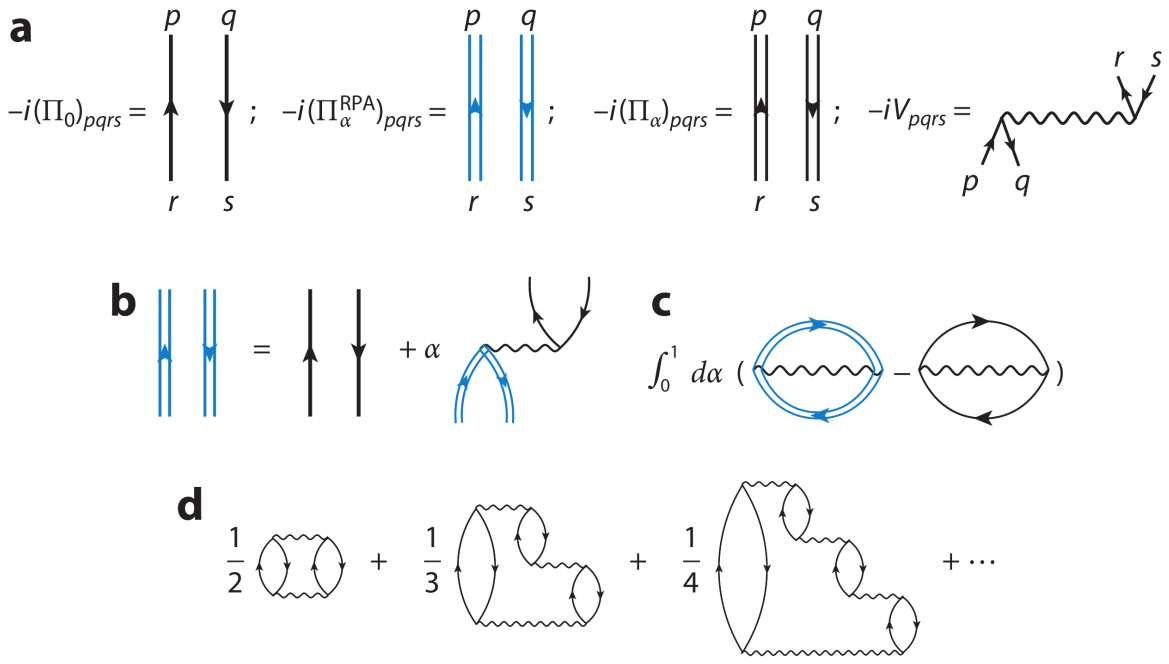

Figure 1.2: Feynman diagrams for (a) noninteracting and interacting polarization propagators and the bare Coulomb interaction, (b) the BSE for $\mathbf{\Pi}_\alpha^{\mathrm{RPA}}$, and ($c$,$d$) the RPA correlation energy before (c) and after (d) coupling strength integration. All closed-loop diagrams are Feynman instead of Goldstone [69] diagrams; because vertices in Feynman diagrams are not time-ordered, each Feynman diagram may correspond to several Goldstone diagrams with different time ordering [54]. For illustrative purposes, we use blue and black double lines to indicate RPA and exact renormalization, respectively; a pair of disconnected double lines should not be understood as a product of single-particle quantities.

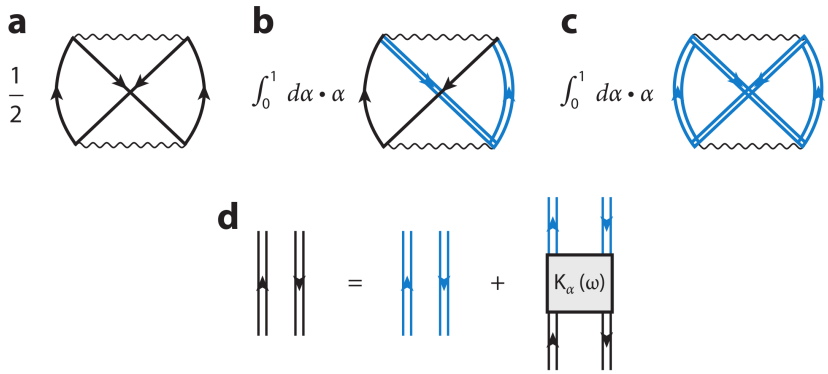

Figure 1.3: Feynman diagrams for (*a*) bare second-order exchange energy, (*b*) AC-SOSEX beyond-RPA correlation energy, (*c*) AXK beyond-RPA correlation energy, and (*d*) RPA-renormalized BSE.

correlation energy [10].

The second-order screened exchange (SOSEX) method by Freeman [23] and Grüneis et al. [39] completely eliminates self-correlation error for one-electron systems. AC-SOSEX beyond-RPA correlation energy [40, 41] is

$$\Delta E^{\text{C AC-SOSEX}} = -\frac{1}{2\pi}\int_0^1 \mathrm{d}\alpha \Big(\alpha\, \Im \int_0^\infty \mathrm{d}\omega \left\langle \mathbf{V\Pi}_\alpha^{\text{RPA}}(\omega)\mathbf{K\Pi}_0(\omega)\right\rangle\Big), \tag{1.31}$$

where

$$\mathbf{K} = \begin{pmatrix} \mathbf{B}^{\text{X}} & \mathbf{B}^{\text{X}} \\ \mathbf{B}^{\text{X}} & \mathbf{B}^{\text{X}} \end{pmatrix} \tag{1.32}$$

is an approximation to the first-order exchange kernel and $B^{\text{X}}_{iajb} = -(ib|ja)$ is the corresponding particle–hole exchange integral. SOSEX partially screens the second-order exchange (Figure 1.3*b*), and is thus useful for small-gap systems and even metals, as opposed to unscreened perturbation theory [39, 71]. However, SOSEX does not consistently improve RPA atomization energies, and it worsens the description of reaction barriers and systems with strong static correlation compared with RPA [42].

Systematic improvement is possible by RPA-renormalized many-body perturbation theory [42]. The key idea is to expand the exact polarization propagator in terms of the RPA polarization propagator

$$\mathbf{\Pi}_\alpha(\omega) = \mathbf{\Pi}_\alpha^{\mathrm{RPA}}(\omega) + \mathbf{\Pi}_\alpha^{\mathrm{RPA}}(\omega)\mathbf{K}_\alpha(\omega)\mathbf{\Pi}_\alpha(\omega), \tag{1.33}$$

diagrammatically represented in Figure 1.3*d*. Because RPA is well-behaved for small-gap systems, this expansion avoids the instabilities of conventional many-body perturbation theory by RPA-renormalizing all particle–hole pairs. Using a frequency-independent approximate exchange kernel (AXK), $\mathbf{K}_\alpha^{\mathrm{AXK}} = \alpha\mathbf{K}$, and truncating the series expansion of $\mathbf{\Pi}_\alpha$ with respect to $\mathbf{K}_\alpha^{\mathrm{AXK}}$ at first order, we obtain the AXK (second-order) beyond-RPA correlation energy (Figure 1.3*c*):

$$\Delta E^{\mathrm{C\ AXK}} = -\frac{1}{2\pi}\int_0^1 \mathrm{d}\alpha \Big(\alpha\, \Im \int_0^\infty \mathrm{d}\omega \left\langle \mathbf{V}\mathbf{\Pi}_\alpha^{\mathrm{RPA}}(\omega)\mathbf{K}\mathbf{\Pi}_\alpha^{\mathrm{RPA}}(\omega) \right\rangle \Big). \tag{1.34}$$

Although AXK still contains some self-correlation error, it dissociates covalent bonds correctly and consistently improves upon RPA [42].

1.5 Implementation of Random-Phase Approximation Correlation Energy

Brute-force computation of the RPA correlation energy using the plasmon formula (Equation (1.24)) requires diagonalization of the $N_\mathrm{h}N_\mathrm{p} \times N_\mathrm{h}N_\mathrm{p}$ supermatrix $\mathbf{M}^{\mathrm{RPA}}$ [17]. Because both N_h and N_p increase linearly with the system size N in a finite basis set, the operation count of this approach scales as $\mathcal{O}(N^6)$ and quickly becomes prohibitive. Alternatively, the RPA correlation energy may be obtained by retaining only ring contractions in a CCD implementation [24], which scales as $\mathcal{O}(N^6)$ in each CCD iteration. RPA correlation energy

calculations using Equation (1.23) also scales as $\mathcal{O}(N^6)$ for each frequency point.

The key to lowering the computational complexity of the RPA correlation energy is to employ low-rank approximations for the ERIs, i.e.,

$$\mathbf{B}^{\mathrm{H}} = \mathbf{S}\mathbf{S}^{\mathrm{T}}. \tag{1.35}$$

This form of decomposition is permitted by the positive definiteness and Hermiticity of $\mathbf{B}^{\mathrm{H}}$. Before discussing specific approximations, we first assume the decomposition is full-rank for analysis purposes. We may now write

$$\mathbf{V} = \boldsymbol{\eta}\boldsymbol{\eta}^{\mathrm{T}}, \tag{1.36}$$

where

$$\boldsymbol{\eta} = \begin{pmatrix} \mathbf{S} \\ \mathbf{S} \end{pmatrix}. \tag{1.37}$$

Using the Sherman–Morrison–Woodbury formula [72, 73], the RPA polarization propagator (Equation (1.19)) can then be written as

$$\boldsymbol{\Pi}_{\alpha}^{\mathrm{RPA}}(\mathrm{i}\omega) = \big(\boldsymbol{\Pi}_0(\mathrm{i}\omega)^{-1} - \alpha\mathbf{V}\big)^{-1} \tag{1.38}$$

$$= \boldsymbol{\Pi}_0(\mathrm{i}\omega) + \alpha\boldsymbol{\Pi}_0(\mathrm{i}\omega)\mathbf{W}_{1,\alpha}(\mathrm{i}\omega)\boldsymbol{\Pi}_0(\mathrm{i}\omega), \tag{1.39}$$

where

$$\mathbf{W}_{1,\alpha}(\mathrm{i}\omega) = \boldsymbol{\eta}\big(\mathbf{1} + \mathbf{Q}(\omega)\big)^{-1}\boldsymbol{\eta}^{\mathrm{T}}, \tag{1.40}$$

$$\mathbf{Q}(\omega) = -\boldsymbol{\eta}^{\mathrm{T}}\boldsymbol{\Pi}_0(\mathrm{i}\omega)\boldsymbol{\eta} = 2\mathbf{S}^{\mathrm{T}}\mathbf{G}(\omega)\mathbf{S}, \tag{1.41}$$

$$\mathbf{G}(\omega) = \mathbf{D}(\mathbf{D}^2 + \omega^2\mathbf{1})^{-1}. \tag{1.42}$$

$\mathbf{1} + \alpha\mathbf{Q}(\omega)$ is the Hermitian version of the generalized dielectric function $\boldsymbol{\kappa}_\alpha^{\mathrm{RPA}}(\mathrm{i}\omega)$ defined in Equation (1.20), i.e., $\mathbf{Q}$ may be interpreted as a generalized susceptibility accounting for screening due to induced particle–hole pairs. $\mathbf{W}_{1,\alpha}$ is the RPA effective interaction $\mathbf{V}_\alpha^{\mathrm{RPA}}$ (Equation (1.22)) in Hermitian form.

Defining $\mathbf{Q}_\alpha^{\mathrm{RPA}} = -\boldsymbol{\eta}^{\mathrm{T}}\boldsymbol{\Pi}_\alpha^{\mathrm{RPA}}(\mathrm{i}\omega)\boldsymbol{\eta}$, Equation (1.39) implies

$$\mathbf{Q}_\alpha^{\mathrm{RPA}} = (\mathbf{1} + \alpha\mathbf{Q})^{-1}\mathbf{Q}. \tag{1.43}$$

Therefore,

$$E^{\mathrm{C\ RPA}} = -\frac{1}{2\pi}\int_0^1 \mathrm{d}\alpha \int_0^\infty \mathrm{d}\omega \big\langle \mathbf{V}\big(\boldsymbol{\Pi}_\alpha^{\mathrm{RPA}}(\mathrm{i}\omega) - \boldsymbol{\Pi}_0(\mathrm{i}\omega)\big)\big\rangle \tag{1.44}$$

$$= \frac{1}{2\pi}\int_0^1 \mathrm{d}\alpha \int_0^\infty \mathrm{d}\omega \big\langle \mathbf{Q}_\alpha^{\mathrm{RPA}}(\omega) - \mathbf{Q}(\omega)\big\rangle \tag{1.45}$$

$$= \frac{1}{2\pi}\int_0^\infty \mathrm{d}\omega \langle \ln(\mathbf{1} + \mathbf{Q}(\omega)) - \mathbf{Q}(\omega)\rangle, \tag{1.46}$$

where we have used Equation (1.36) and the cyclic invariance of the trace operation; analytic integration over α has been performed. The frequency integration may be performed numerically using a Clenshaw–Curtis quadrature [74]. If a system-independent energy error is desired, e.g., for reaction energy calculations, finer quadratures are required for larger systems; the number of quadrature points scales as $\mathcal{O}(\ln N)$ due to its exponential convergence [75]. In practice, however, a quadrature of $\leq$100 points is adequate for most small- and medium-size molecules.

A low-rank approximation of $\mathbf{B}^{\mathrm{H}}$ is provided by the resolution-of-the-identity (RI) approximation [76, 77]. This is achieved by introducing an auxiliary basis set of N_{aux} atom-centered Gaussian functions labeled by $P, Q, \ldots$ and setting $S_{iaP} = \sum_Q (ia|Q)[\mathbf{L}^{-1}]_{QP}$ in Equation (1.35), where $(ia|Q)$ is a three-index Coulomb integral and $\mathbf{L}$ is the Cholesky factor of the $N_{\mathrm{aux}} \times N_{\mathrm{aux}}$ matrix of two-index Coulomb integrals $(P|Q)$. Here and henceforth, $\mathbf{S}$

with the RI approximation is employed unless stated otherwise. An important property of RI-RPA is that the RI-RPA correlation energy is variationally bounded from below by the RPA correlation energy obtained without RI. This was first shown in [21] under the assumption that the RI error in the direct ring-CCD amplitudes is negligible. A more rigorous proof free from this assumption is provided in [78] and is detailed in Appendix B. Owing to this property, RI-RPA calculations can be highly accurate with auxiliary basis sets of ∼3–5 times the size of the corresponding AO basis sets. Auxiliary basis sets optimized for RI-MP2 energies [79] lead to errors on the order of 10 microhartree per atom in RPA calculations, which is below the inherent method error in typical applications [21]. The variational boundedness also allows for optimizing auxiliary basis sets specifically for RI-RPA. Historically, the RI approximation is referred to as density fitting in the Coulomb metric, which is equivalent to least-squares fitting of electrostatic fields generated by particle–hole pairs [77]. While density fitting methods in local metrics may lead to more favorable scaling [80–82], their lack of variational boundedness can give rise to larger errors [77, 81, 82]. Schemes to recover [83] or partially recover [84] variational boundedness for density fitting in local metrics are still under active development.

Since the number of auxiliary basis functions N_{aux} scales linearly with the system size N, the computation of $\mathbf{Q}$ at a specific frequency point scales as $\mathcal{O}(N^4)$, resulting in a $\mathbf{O}(N^4 \ln N)$ RI-RPA implementation using Equation (1.46) with system-independent quadrature error. Further lowering of the computational complexity has been achieved by decomposing $\mathbf{\Pi}_0$ using Laplace transform [85, 86] and frequency-domain [87] techniques with density fitting in the least-squares (or overlap) metric [80] or tensor hypercontraction [88], and by local domain coupled-cluster methods [89]. These algorithms scale favorably for large systems with small basis sets, but come at the cost of larger prefactors compared with higher-scaling approaches and, in some cases, additional parameters. Thus, the quartic scaling algorithm may be more efficient than lower-scaling alternatives up to well above 100 atoms in typical applications. Timing results for the S12L benchmark set is provided in Reference [12],

where an effective scaling of $N^{3.49}$ is observed for the $\mathcal{O}(N^4 \ln N)$ RI-RPA implementation in TURBOMOLE 7.0.

Chapter 2

Perturbative Corrections to Random-Phase Approximation Energies

 The material in this chapter is based upon work supported by the National Science Foundation under CHE-1464828 and CHE-1800431.

2.1 Introduction

Electronic structure methods based on the random phase approximation (RPA) [9–12] yield consistent accuracy at reasonable computational cost for a wide range of applications in quantum chemistry and solid-state physics. Compared with finite-order perturbation methods, such as second-order Møller–Plesset (MP2) theory [90], RPA is relatively insensitive to the gap size and free of the divergence problem for metallic systems [91]. RPA captures long-range correlation effects and "seamlessly" accounts for dispersion interactions [27, 92, 93]. While RPA takes into account some of the strong correlation arising in dissociating electron pair bonds [6, 17], it has long been recognized that RPA is qualitatively deficient at higher electron coupling strengths and short interaction range [23, 38], as reflected in its poor performance for ionization and atomization energies [10].

The formal and computational appeal of RPA has triggered a search for simple remedies to these deficiencies. Corrections based on ground-state density functional theory (DFT) [94, 95], including range-separated RPA methods [96–99], incorporate semilocal density functionals to correct RPA [100, 101]. "Local-field corrections" to RPA were pioneered by Singwi, Tosi, Land, and Sjölander (STLS) in the 1960s [38] and may be viewed as an early, physically inspired attempt to devise approximate exchange–correlation (XC) kernels accounting for short-range correlations beyond RPA. Further developments along these lines include the inhomogeneous STLS method [102], semilocal kernels [103], local [104] and nonlocal [105, 106] energy-optimized kernels, as well as model kernels derived from the uniform electron gas by momentum space cutoff [107, 108], frequency-dependent effective interaction models [109], and jellium-with-gap models [110]. While these corrections can be designed to deliver high accuracy for certain applications, uniform improvement upon RPA for a wide range of systems and properties at moderate computational cost has been difficult to achieve.

The notion of "beyond-RPA corrections" is based on the implicit assumption that beyond-

RPA correlation is, in some sense, small compared with correlation effects captured by RPA. For the uniform electron gas, conventional many-body perturbation theory diverges in every order due to the long range of the *bare* electron-electron Coulomb interaction [15]. On the other hand, the effective interaction accounting for beyond-RPA correlation is shorter ranged, at least for high to intermediate densities [32], suggesting that perturbation theory may be an effective means to derive beyond-RPA corrections. This led to the development of second-order perturbative corrections to RPA, starting with the second-order screened exchange (SOSEX) method [23, 39–41]. Unlike RPA, SOSEX is one-electron self-correlation-free [18], but it incorrectly dissociates covalent bonds within spin-restricted formalism [18] and produces less accurate reaction barrier heights than RPA [22, 28, 42]. RPA-renormalized many-body perturbation theory is based on a perturbative expansion of the Bethe-Salpeter equation (BSE) [36, 66] starting from RPA as zero-order solution [42]. The second-order RPA-renormalized perturbation method using the approximate exchange kernel (AXK)—hereafter referred to as the AXK method—yielded more accurate energetics than RPA for small molecules, consistently improving upon RPA for ionization and atomization energies [42]. These results also suggested that AXK preserves the accuracy of RPA and outperforms SOSEX for reaction barrier heights. Nevertheless, the lack of efficient implementations has hampered a thorough assessment of AXK in the past.

In this chapter, we present two AXK algorithms that scale as $\mathcal{O}(N^5 \ln N)$ and $\mathcal{O}(N^4 \ln N)$ with the system size N. These algorithms also enable efficient SOSEX and bare second-order exchange (SOX) calculations. Low-scaling SOSEX and AXK algorithms have been proposed in References [21, 22, 42, 111–114] and a SOSEX implementation with sub-cubic effective scaling for linear alkanes has been recently reported in Reference [114]. Our primary aim is to enable efficient calculations for moderately large molecular systems with constant, predetermined accuracy independent of system size. This enables a critical assessment of second-order beyond-RPA corrections using diverse benchmark sets for reaction barrier heights, reaction energies, and noncovalent interaction energies. We also present tests on dissociation energies

of charged dimers where RPA self-correlation error is pronounced, and of transition-metal compounds that feature diverse bondings. Finally, we discuss whether, and under what circumstances, perturbative corrections to RPA are worthwhile.

2.2 Theory

As introduced in Section 1.4, the AXK beyond-RPA correlation energy

$$\Delta E^{\mathrm{C\ AXK}} = -\frac{1}{2\pi}\int_0^1 \mathrm{d}\alpha \Big(\alpha \int_0^\infty \mathrm{d}\omega \left\langle \mathbf{V}\mathbf{\Pi}_\alpha^{\mathrm{RPA}}(\mathrm{i}\omega)\mathbf{K}\mathbf{\Pi}_\alpha^{\mathrm{RPA}}(\mathrm{i}\omega) \right\rangle \Big) \tag{2.1}$$

correctly recovers the second-order exchange (SOX) energy $\Delta E^{\mathrm{C\ SOX}}$ but also contains higher-order terms that amount to screening at higher coupling strength. Using the Equation (1.39) and the cyclic invariance of the trace operation, we may write

$$\begin{aligned}
\langle \mathbf{V}\mathbf{\Pi}_\alpha^{\mathrm{RPA}}(\mathrm{i}\omega)\mathbf{K}\mathbf{\Pi}_\alpha^{\mathrm{RPA}}(\mathrm{i}\omega) \rangle &= \langle \boldsymbol{\eta}^{\mathrm{T}}\mathbf{\Pi}_\alpha^{\mathrm{RPA}}(\mathrm{i}\omega)\mathbf{K}\mathbf{\Pi}_\alpha^{\mathrm{RPA}}(\mathrm{i}\omega)\boldsymbol{\eta} \rangle \\
&= \langle \big(\mathbf{1} + \alpha\mathbf{Q}(\omega)\big)^{-1}\boldsymbol{\eta}^{\mathrm{T}}\mathbf{\Pi}_0(\mathrm{i}\omega)\mathbf{K}\mathbf{\Pi}_0(\mathrm{i}\omega)\boldsymbol{\eta}\big(\mathbf{1} + \alpha\mathbf{Q}(\omega)\big)^{-1} \rangle \\
&= \langle \boldsymbol{\eta}\big(\mathbf{1} + \alpha\mathbf{Q}(\omega)\big)^{-2}\boldsymbol{\eta}^{\mathrm{T}}\mathbf{\Pi}_0(\mathrm{i}\omega)\mathbf{K}\mathbf{\Pi}_0(\mathrm{i}\omega) \rangle,
\end{aligned}$$

and therefore obtain

$$\Delta E^{\mathrm{C\ AXK}} = -\frac{1}{2\pi}\int_0^1 \mathrm{d}\alpha \int_0^\infty \mathrm{d}\omega \big\langle \alpha\mathbf{W}_{2,\alpha}(\mathrm{i}\omega)\mathbf{\Pi}_0(\mathrm{i}\omega)\mathbf{K}\mathbf{\Pi}_0(\mathrm{i}\omega) \big\rangle \tag{2.2}$$

$$= -\frac{1}{2\pi}\int_0^\infty \mathrm{d}\omega \big\langle \bar{\mathbf{W}}_2(\mathrm{i}\omega)\mathbf{\Pi}_0(\mathrm{i}\omega)\mathbf{K}\mathbf{\Pi}_0(\mathrm{i}\omega) \big\rangle, \tag{2.3}$$

where the effective interaction $\mathbf{W}_{2,\alpha}(\mathrm{i}\omega) = \boldsymbol{\eta}\big(\mathbf{1} + \alpha\mathbf{Q}(\omega)\big)^{-2}\boldsymbol{\eta}^{\mathrm{T}}$ is more strongly screened than the RPA effective interaction $\mathbf{W}_{1,\alpha}(\mathrm{i}\omega)$ defined in Equation (1.40). $\bar{\mathbf{W}}_2$, the coupling-

strength average of $\alpha\mathbf{W}_{2,\alpha}$, can be integrated analytically [42, 105, 114]:

$$\bar{\mathbf{W}}_2(\mathrm{i}\omega) = \int_0^1 \mathrm{d}\alpha\big(\alpha\mathbf{W}_{2,\alpha}(\mathrm{i}\omega)\big) = \boldsymbol{\eta} f_2(\mathbf{Q}(\omega))\boldsymbol{\eta}^{\mathrm{T}}, \tag{2.4}$$

where the function f_2 is defined on $[0,\infty)$ according to Table 2.1. We may rearrange Equation (2.3) and write

$$\Delta E^{\mathrm{C\ AXK}} = -\frac{1}{2\pi}\int_0^\infty \mathrm{d}\omega\big\langle \mathbf{P}_2(\omega)\mathbf{B}^{\mathrm{X}}\big\rangle, \tag{2.5}$$

where

$$\mathbf{P}_2(\omega) = 4\mathbf{G}(\omega)\mathbf{S} f_2(\mathbf{Q}(\omega))\mathbf{S}^{\mathrm{T}}\mathbf{G}(\omega), \tag{2.6}$$

$\mathbf{P}_2(\omega)$ is positive semidefinite due to the positive semidefiniteness of $\mathbf{Q}(\omega)$ and the positivity of the function f_2. As a result, $\Delta E^{\mathrm{C\ AXK}}$ is always positive, mitigating the overcorrelation problem of RPA. $-\frac{1}{\pi}\int_0^\infty \mathrm{d}\omega\mathbf{P}_2(\omega)$ is an exchange-type correction to the coupling-strength-averaged two-electron reduced density matrix (2RDM); it diminishes the 2RDM, and therefore the pair density, when particle–hole pairs interact through exchange. As a result, self-correlation of same-spin electrons is removed exactly to second order, and approximately to higher orders in the correlation energy [42].

Similarly, the SOX and SOSEX beyond-RPA correlation energies within the ACFD theorem can be cast into the forms of Equations (2.2), (2.3), and (2.5) [22], with altered effective interactions labeled by subscripts 0 and 1, respectively. Analytic coupling strength integration can also be performed [21, 111]. The corresponding $\mathbf{W}_\alpha$ and f are defined in Table 2.1. The f functions are plotted in Figure 2.1. It is readily shown that the AXK beyond-RPA correlation correction is always lower than the SOSEX correction, which is in turn lower than the SOX correction.

Table 2.1: Definitions of the effective interaction $\mathbf{W}_\alpha$ and the function f for different second-order beyond-RPA methods

Method	Subscript	$\mathbf{W}_\alpha(\mathrm{i}\omega)$	$f(x)$
SOX	0	$\mathbf{V} = \boldsymbol{\eta}\boldsymbol{\eta}^{\mathrm{T}}$	$1/2$
SOSEX	1	$\boldsymbol{\eta}\big(\mathbf{1} + \alpha\mathbf{Q}(\omega)\big)^{-1}\boldsymbol{\eta}^{\mathrm{T}}$	$-x^{-2}\ln(1+x) + x^{-1}$
AXK	2	$\boldsymbol{\eta}\big(\mathbf{1} + \alpha\mathbf{Q}(\omega)\big)^{-2}\boldsymbol{\eta}^{\mathrm{T}}$	$x^{-2}\ln(1+x) - x^{-1}(1+x)^{-1}$

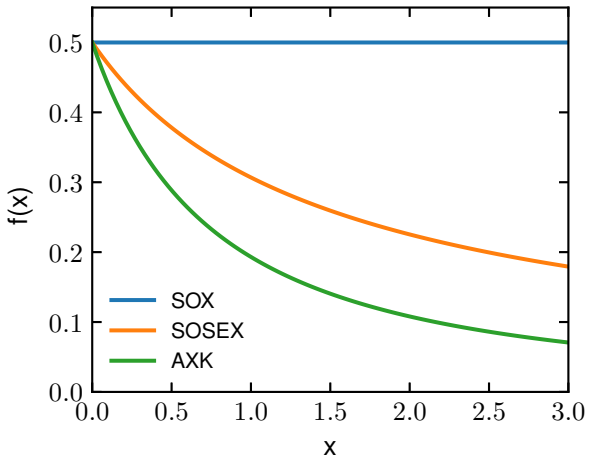

Figure 2.1: The function specifying the coupling-strength-averaged effective interaction for a beyond-RPA exchange correction method (see Table 2.1). Reprinted with permission from Reference [78], Copyright 2018 American Chemical Society.

For each method, f is a function of $\mathbf{Q}(\omega)$ and characterizes the coupling-strength-averaged effective interaction due to screening. As shown in Figure 2.1, the AXK f_2 function decays more rapidly than its SOSEX and SOX counterparts. Since the SOSEX effective interaction $\mathbf{W}_{1,\alpha}(\mathrm{i}\omega)$ is identical to that of RPA, the AXK screening is stronger than the RPA screening particularly for large eigenvalues of $\mathbf{Q}(\omega)$. For the uniform electron gas with high density, large eigenvalues of $\mathbf{Q}(\omega)$ originate from small momentum transfers [115, 116], which correspond to long-range inter-electron distances; therefore, the AXK correction to the pair density in the long-range region is strongly attenuated, and its main effects are in the short-range region. This is consistent with the observation that beyond-RPA correlation in the uniform electron gas is short ranged at high and intermediate densities [14, 116, 117].

2.3 Implementations

2.3.1 Molecular Orbital Based AXK Algorithm

A straightforward evaluation of the integrand of Equation (2.5) scales as $\mathcal{O}(N^6)$ since all the matrices therein are of $N_\mathrm{h}N_\mathrm{p} \times N_\mathrm{h}N_\mathrm{p}$ dimension. The scaling is reduced to $\mathcal{O}(N^5)$ with the RI approximation since $\Delta E^{\mathrm{C\ AXK}}$ may be expressed in terms of matrices that either scale as N^2 or N^3 or may be computed on the fly.

With RI, the dimension of the $\mathbf{Q}(\omega)$ matrix defined in Equation (1.41) is $N_\mathrm{aux} \times N_\mathrm{aux}$ and scales quadratically with N. An eigen decomposition of $\mathbf{Q}(\omega)$ can be readily performed with $\mathcal{O}(N^3)$ operations, yielding

$$\mathbf{Q}(\omega) = \mathbf{X}(\omega)\mathbf{q}(\omega)\mathbf{X}^\mathrm{T}(\omega). \tag{2.7}$$

A symmetric decomposition $\mathbf{P}_2(\omega) = \mathbf{R}(\omega)\mathbf{R}^\mathrm{T}(\omega)$ thereby follows, where

$$\mathbf{R}(\omega) = 2\mathbf{G}(\omega)\mathbf{S}\mathbf{X}(\omega)(f_2(\mathbf{q}(\omega)))^{1/2} \tag{2.8}$$

is a $N_\mathrm{h}N_\mathrm{p} \times N_\mathrm{aux}$ matrix. For a given ω, $\mathbf{R}(\omega)$ and $\mathbf{P}_2(\omega)$ can be constructed with $\mathcal{O}(N^4)$ and $\mathcal{O}(N^5)$ operations, respectively. We drop the subscript 2 in the following, since the same algorithm can also be applied to SOX and SOSEX.

The frequency integration can be performed using the same Clenshaw–Curtis quadrature as in the RI-RPA algorithm [21] with quadrature points and weights denoted as $\{\omega_I\}$ and $\{w_I\}$, respectively, where $I = 1, \ldots, N_\mathrm{g}$. Since the integration is mapped to an equidistant quadrature on the interval $[0, \pi/2]$, a nested quadrature rule can be designed. The error of the Clenshaw–Curtis quadrature decreases exponentially with N_g [74]. Therefore, an extra

$\mathcal{O}(\ln N)$ scaling factor arises if size-independent accuracy is desired.

Algorithm 1: MO based RI-AXK algorithm. Index loops are implied if not explicitly shown. ω_I and w_I are the frequency quadrature points and weights. For simplicity, the ω_I dependence of various quantities are not explicitly indicated.

```
Compute S                                                          (1)
for ω_I do
    Compute and decompose Q                                        (2)
    for 𝓘 block do
        for i ∈ 𝓘 do
            R_iaP ← 2 G_ia S_iaQ X_QP f^{1/2}(q_P)                 (3)
        end
        for j ≥ min 𝓘 do
            R_jbP ← 2 G_jb S_jbQ X_QP f^{1/2}(q_P)                 (4)
            for 𝓘 ∋ i ≤ j do
                P_iajb ← R_iaP R_jbP                               (5)
                (ja|ib) ← S_jaP S_ibP                              (6)
                ΔE^{C AXK} ← w_I P_iajb (ja|ib)/π                  (7)
            end
        end
    end
end
```

Straightforward application of the RI approximation to $\mathbf{B}^{\mathrm{X}}$ leads to $O(N^5 \ln N)$ scaling, as outlined in Algorithm 1. The three-index array $\mathbf{S}$ is precomputed and stored on disk. It is read in asynchronously per block $\mathcal{I}$ of occupied orbitals and per j index in the inner occupied-orbital loop. All other quantities are computed in memory. This algorithm is easily parallelized using shared-memory parallel basic linear algebra subprograms (BLAS) [118]. The frequency integration loop is kept outermost to facilitate future implementations of hierarchical distributed-memory parallelism. The higher asymptotic scaling of this algorithm compared with that of RI-RPA reflects the well-known result that RI methods are significantly less efficient for exchange-type contractions than for direct-type contractions.

2.3.2 Atomic Orbital Based AXK Algorithm

The scaling of evaluating $\Delta E^{\mathrm{C\ AXK}}$ can be further reduced if the exchange-type contraction in Equation (2.5) is computed using integral-direct techniques [119]. This requires transformation of $\mathbf{R}(\omega)$, and therefore $\mathbf{P}(\omega)$, to the atomic orbital (AO) basis according to

$$R_{\lambda\mu P}(\omega) = \sum_{ia} C_{\lambda i} C_{\mu a} R_{iaP}(\omega), \tag{2.9}$$

where $\mathbf{C}$ is the orbital coefficient matrix; Greek indices denote AO basis functions. We use the same symbol for quantities in the molecule orbital (MO) and AO representations; they can be distinguished by the set of indices being used. The AXK correction is obtained by contracting the AO exchange integrals with the transformed $\mathbf{P}$, i.e.,

$$\Delta E^{\mathrm{C\ AXK}} = \frac{1}{2\pi} \int_0^\infty \mathrm{d}\omega \sum_{\kappa\lambda\mu\nu} P_{\lambda\mu\nu\kappa}(\omega)(\kappa\lambda|\mu\nu) \tag{2.10}$$

Both $\mathbf{P}$ and the integrals are prescreened using the Cauchy–Schwarz inequality [120]. However, the screening is mainly due to the sparsity of the integrals; the sparsity of $\mathbf{P}$ is not prominent, as opposed to constructing the exchange part of the Fock matrix, in which sparsity is enhanced by the difference density matrix technique [120]. As a result, the scaling of integral computation is $\mathcal{O}(N^2)$, and the construction of $\mathbf{R}(\omega)$ and $\mathbf{P}(\omega)$ requires $\mathcal{O}(N^4)$ and $\mathcal{O}(N^3)$ operations, respectively, for a given ω. As a trade off between repeated I/O and increasing disk storage requirement, half-transformed $\mathbf{R}(\omega)$ indexed by $i\mu P$ is precomputed and asynchronously read in inside the inner loops. As outlined in Algorithm 2, the computational complexity scales as $\mathcal{O}(N^4 \ln N)$ after numerical frequency integration. The algorithm is parallelized over the κ and λ loops using OpenMP [121]. Again, the numerical frequency integration loop is outermost to enable further parallelism over distributed quadrature points

and to facilitate more effective screening for each frequency point.

Algorithm 2: AO based RI-AXK algorithm. Index loops are implied if not explicitly shown. The screening of $\mu, \nu, \kappa, \lambda$ quadruples on every level of the nested loops is performed.

```
Compute S                                                              (1)
for ω_I do
    Compute and decompose Q                                            (2)
    for I block do
        for i ∈ I do
            R_iaP ← 2 G_ia S_iaQ X_QP f^{1/2}(q_P)                     (3)
            R_iμP ← C_μa R_iaP                                         (4)
        end
    end
    for K block do
        for κ ∈ K do
            R_νκP ← C_νi R_iκP                                         (5)
        end
        for μ ≥ min K do
            R_λμP ← C_λi R_iμP                                         (6)
            for K ∋ κ ≤ μ do
                for λ do
                    for N block do
                        for ν ∈ N do
                            Compute (κλ|μν)                            (7)
                        end
                        P_λμνκ ← R_λμP R_νκP                           (8)
                        ΔE^{C AXK} ← w_I P_λμνκ (κλ|μν)/π              (9)
                    end
                end
            end
        end
    end
end
```

2.4 Computational Details

Both the MO and AO based AXK algorithms were implemented in the `rirpa` module of the TURBOMOLE quantum chemistry program package [25] and are scheduled for a future public release. The SOX and SOSEX beyond-RPA methods were implemented similarly according to Section 2.2. All reference KS calculations were performed in C_1 point-group symmetry using the Tao–Perdew–Staroverov–Scuseria (TPSS) meta-generalized-gradient-approximation (meta-GGA) functional [63], which has been shown to yield uniform accuracy even for transition-metal compounds [122, 123]. For the KS calculations, density matrix and energy convergence criteria were set to 10^{-7} or tighter, and fine density grids of at least m5 quality [64] were used. Core electrons were kept frozen in RPA-type calculations. Coupling-strength-dependent AXK and SOSEX calculations without the RI approximation were performed using the `mpgrad` module in TURBOMOLE 7.2 [42].

Karlsruhe def2-series basis sets of double-ζ (SVP), triple-ζ (TZVP), and quadruple-ζ (QZVPP) quality were used [61, 124]. The corresponding auxiliary basis sets optimized for RI-MP2 [125, 126] were used for the RI approximation in the RPA and beyond-RPA calculations. For validation, complete basis set (CBS) limit of the correlation energy $E^{\mathrm{C}}(\infty)$ is estimated using the two-point extrapolation scheme [127, 128]

$$E^{\mathrm{C}}(X) = E^{\mathrm{C}}(\infty) + A/X^3, \tag{2.11}$$

where X is the cardinal number of the basis set and A is a coefficient to be determined. The correlation consistent basis sets aug-cc-pVXZ (AVXZ; X = T, Q, 5) [129–131] and corresponding auxiliary basis sets [126, 132, 133] were used for the basis set extrapolation calculations. For all the correlation energy calculations using the AVXZ basis sets, the KS energy expectation values were computed using the QZVPP basis set, which yields small basis set superposition errors [124].

2.5 Results

In this section, we first validate our implementations by estimating the errors due to integral prescreening, the RI approximation, and numerical frequency integration. Timings of the algorithms are measured using large mesityl substituted porphyrin molecules[134] as well as benchmark sets from the GMTKN55 database for diverse reaction barrier heights (BH-DIV10), Diels–Alder reaction energies (DARC), and interaction energies of n-alkane dimers (ADIM6) [135, 136]. We then test the accuracy of the AXK methods using these benchmarks as well as a benchmark set for assessing self-interaction error (SIE4x4) [135, 136] and a $3d$ transition-metal reference set proposed in Reference [123]. These benchmark systems contain diverse types of molecules and bonding situations featuring weak to moderately strong correlations.

2.5.1 Integral Prescreening

In the AO based algorithm, the integral prescreening is performed according to

$$\frac{1}{2\pi} w_I \left(P_{\lambda\mu\lambda\mu}(\omega_I) P_{\nu\kappa\nu\kappa}(\omega_I) (\kappa\lambda|\kappa\lambda)(\mu\nu|\mu\nu) \right)^{1/2} \leq \frac{\varepsilon}{N_\mathrm{g}\sqrt{N_\mathrm{bf}}} \tag{2.12}$$

for a shell quadruple $\kappa, \lambda, \mu, \nu$ at a frequency point ω_I. Here ε is the screening threshold, and N_bf is the number of basis functions. The $1/N_\mathrm{g}$ factor guarantees that the screening error does not increase with the number of quadrature points. The $1/\sqrt{N_\mathrm{bf}}$ factor is included to make the screening error size-independent, assuming that entries screened by Equation (2.12) are independent and mean zero [137]. This is opposed to the recent low-scaling SOSEX implementation [114], where a constant screening threshold was used for all systems. Table 2.2 summarizes the integral screening errors with various screening thresholds for $\Delta E^{\mathrm{C\ AXK}}$ of molecules in the DARC benchmark set. $\varepsilon = 10^{-7}$ is chosen for all the following AO based

beyond-RPA calculations.

Table 2.2: Mean errors (ME) and maximum absolute errors (MXE) of $\Delta E^{\mathrm{C\ AXK}}$ (in $\mathrm{E_h}$) due to integral screening for compounds in the DARC benchmark set [138, 139] relative to values obtained with $\varepsilon = 10^{-10}$. The TZVP basis set was used.

ε	10^{-6}	10^{-7}	10^{-8}	10^{-9}
ME	-2.9×10^{-4}	-2.4×10^{-5}	-1.6×10^{-6}	-8.5×10^{-8}
MXE	5.0×10^{-4}	4.2×10^{-5}	2.9×10^{-6}	1.6×10^{-7}

2.5.2 Accuracy of the RI Approximation

Two kinds of RI approximation errors arise in the present implementations. The first originates from the RI approximation of the Hartree kernel in RPA. This kind of RI error is assumed to be similar to that in the RI-RPA algorithm, where the error is bounded thanks to the variational boundedness of $\mathbf{Q}(\omega)$ within the RI approximation (see Appendix B). Here we assess the second kind of RI error, which only exists in the MO based algorithm and is due to the RI approximation of $\mathbf{B}^{\mathrm{X}}$. It is readily shown that this kind of RI approximation is variational and errors are always negative. Table 2.3 summarizes the RI errors of the second kind for molecules in the BHDIV10, DARC, and ADIM6 benchmark sets [135]. The errors are on the order of 100 $\mu\mathrm{E_h}$ for all these systems.

Table 2.3: Mean errors (ME) and maximum absolute errors (MXE) of $\Delta E^{\mathrm{C\ AXK}}$ (in $\mathrm{E_h}$) due to the RI approximation of the exchange integrals. Calculations were performed for all the species in the BHDIV10, DARC, and ADIM6 benchmark sets [135] using the SVP and TZVP basis sets.

	BHDIV10		DARC		ADIM6	
	SVP	TZVP	SVP	TZVP	SVP	TZVP
ME	-3.6×10^{-4}	-1.9×10^{-4}	-5.2×10^{-4}	-2.6×10^{-4}	-4.0×10^{-4}	-2.2×10^{-4}
MXE	6.7×10^{-4}	3.5×10^{-4}	8.3×10^{-4}	4.3×10^{-4}	8.4×10^{-4}	4.6×10^{-4}

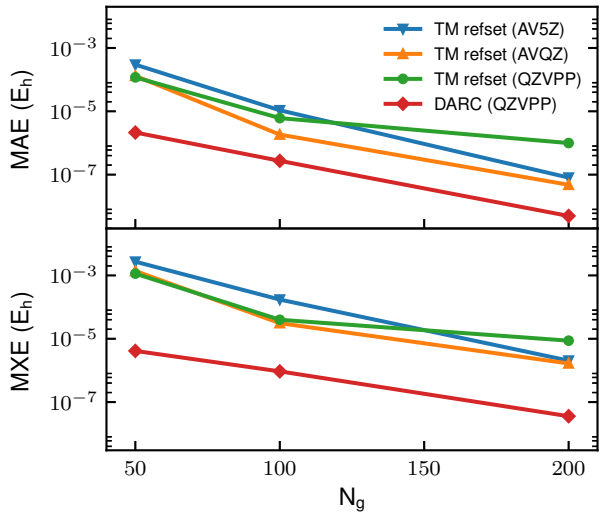

Figure 2.2: Mean absolute errors (MAE) and maximum absolute errors (MXE) of $\Delta E^{\mathrm{C\ AXK}}$ due to the numerical frequency integration with varying number of quadrature points N_{g} for the transition-metal reference set (TM refset)[123] and the Diels–Alder reaction energy (DARC) benchmark set, [138, 139] using the QZVPP, AVQZ, and AV5Z basis sets. Reference values were obtained from calculations with fine quadratures of $N_{\mathrm{g}} = 400$. Reprinted with permission from Reference [78], Copyright 2018 American Chemical Society.

2.5.3 Accuracy of the Quadrature

Figure 2.2 shows the numerical integration errors in AXK beyond-RPA correlation energies for molecules in the DARC benchmark set [138, 139] and the $3d$ transition-metal reference set [123]. The transition-metal reference set contains small-gap open-shell species, which demand large numbers of quadrature points [21]. These results were obtained using the MO based algorithm. For both sets of molecules, the errors decrease rapidly with increasing number of quadrature points. Particularly, the exponential decay of the error is observed for the DARC benchmark set with the QZVPP basis set. Moreover, the numerical integration errors for $\Delta E^{\mathrm{C\ AXK}}$ are almost always positive, whereas the numerical integration errors for $E^{\mathrm{C\ RPA}}$ are almost always negative. The errors in the total correlation energies are on the same order as the errors in $\Delta E^{\mathrm{C\ AXK}}$. Generally, a quadrature with 100 points leads to sub-$m\mathrm{E_h}$ error due to numerical integration. For energy differences, smaller quadratures may be used because of error cancellation. A nested Clenshaw–Curtis rule doubling N_{g} until a

predetermined precision is achieved was also implemented. For benchmark purposes, very fine frequency quadratures with 400 points were used unless otherwise stated.

2.5.4 Performance

We assess the performance of our implementations using all the molecules in the BHDIV10, DARC, and ADIM6 benchmarks from the GMTKN55 database [135] using different basis sets. We also carried out AXK calculations for mesityl substituted porphyrin monomer and dimer [134] with 113 and 224 atoms, respectively, using the SVP basis set. The timing results are shown in Figure 2.3, wherein the effective scalings are also listed. Clearly, the asymptotic quintic and quartic scalings do not show up for these test calculations yet. Although the AO based algorithm scales more favorably, it is less efficient for most of the small- and medium-size molecules due to a large scaling prefactor. The AO based algorithm eventually becomes faster than the MO based algorithm for the large mesityl substituted porphyrin dimer with the SVP basis set, see Table 2.4. However, for calculations with quadruple-ζ basis sets, the AO based algorithm is impractical since the prefactor becomes larger due to inefficient integral screening.

As we shall see in the following benchmark calculations, basis sets of at least triple-ζ quality need to be used for accurate AXK energetics. For this reason, the following benchmark calculations were performed using the MO based algorithm.

Table 2.4: Timing results (wall time in hours) for the mesityl substituted porphyrin monomer ($NiC_{56}H_{52}N_4$) and dimer ($Ni_2C_{112}H_{100}N_{10}$). [134] The calculations were performed on a 20-core Intel Xeon E5-2680 2.80 GHz workstation using a maximum of 80 GiB of memory.

System	N_{bf}	t^{MO}	t^{AO}
$NiC_{56}H_{52}N_4$	1196	8.53	21.20
$Ni_2C_{112}H_{100}N_{10}$	2402	212.45	200.04

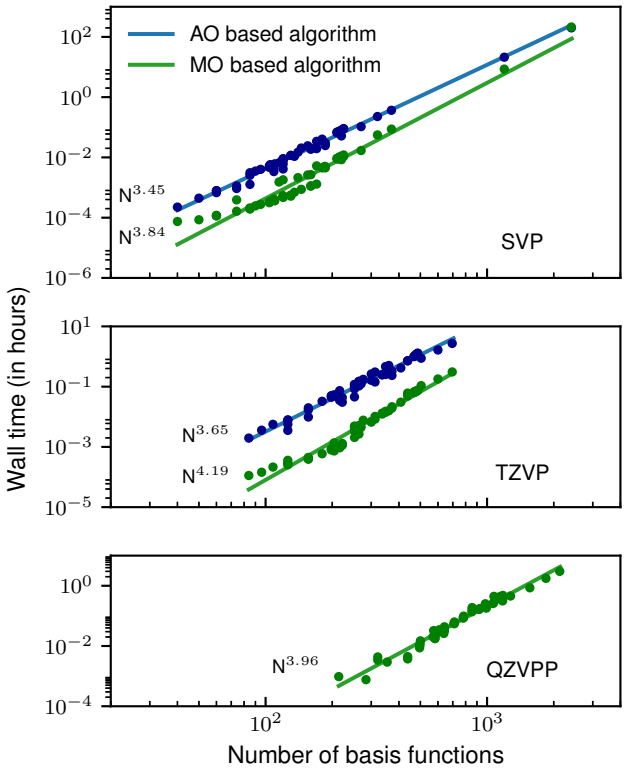

Figure 2.3: Timing results for AXK total energy calculations on molecules in the BHDIV10, DARC, and ADIM6 benchmark sets [135] as well as mesityl substituted porphyrins [134] (SVP only) using the SVP, TZVP, and QZVPP basis sets. The effective scalings are listed next to the fitted lines. The timings were done for calculations with $N_g = 50$. All calculations were performed on a 20-core Intel Xeon E5-2680 2.80 GHz workstation using a maximum of 80 GiB of memory. Reprinted with permission from Reference [78], Copyright 2018 American Chemical Society.

2.5.5 Benchmarks

Reaction Barrier Heights

Accurate prediction of reaction barrier heights requires a balanced treatment of static correlation and self-interaction [140, 141]. Semilocal DFT generally underestimates barrier heights [2], whereas single-reference perturbation methods are prone to overestimation [142, 143]. Here we present benchmark calculations for the BHDIV10 set, [135] which contains 10 reactions of medium-size molecules and features diverse barrier heights ranging from

Table 2.5: Errors of calculated reaction barrier heights in kcal/mol using the QZVPP basis set for the BHDIV10 benchmark set relative to explicitly correlated coupled-cluster results in Reference [135]. The structures of the reactants and transition states are provided in Reference [136].

Reaction	Ref.	TPSS	TPSS-D3	RPA	AXK	SOSEX	SOX
1	25.65	−10.11	−10.37	−2.33	−0.75	1.69	10.05
2	56.90	1.37	0.94	−1.40	0.84	4.27	14.38
3	36.53	−7.82	−7.21	−1.32	−0.43	1.13	5.54
4	96.17	−6.64	−7.51	−1.24	0.64	3.61	13.47
5	15.94	−7.00	−7.23	0.52	0.92	1.22	2.46
6	13.64	−4.39	−4.84	1.79	2.21	2.09	1.74
7	27.49	−2.73	−3.16	−0.18	0.91	1.71	3.77
8	50.24	−10.12	−10.29	2.88	3.38	3.59	3.88
9	65.84	−7.17	−7.19	−1.49	−0.40	1.11	5.12
10	64.93	−3.41	−3.37	−3.29	−2.50	−1.90	−3.32
ME		−5.80	−6.02	−0.61	0.48	1.85	5.71
MAE		6.08	6.21	1.64	1.30	2.23	6.37
MXE		10.12	10.37	3.29	3.38	4.27	14.38

13.64 kcal/mol to 96.17 kcal/mol. Results obtained using the QZVPP basis set are shown in Table 2.5.

As expected, the TPSS meta-GGA functional underestimates the BHDIV10 barrier heights, except for Reaction 2, which is the isomerization from 1,4-azaborine to B-N Dewar benzene. Adding the D3 dispersion correction [7] does not improve the results, indicating that the dispersion interaction energy does not change much from the reactants to the transition states. The RPA barrier heights are significantly more accurate, yet they are still statistically slightly lower than the reference values. Compared with RPA, AXK systematically increases the calculated barrier heights and further reduces the mean absolute error (MAE) from 1.64 kcal/mol to 1.30 kcal/mol. SOSEX yields even larger barrier heights and overcorrects RPA, especially for reactions that break π bonds (Reactions 2, 4, and 8). These results are consistent with previous tests on small-molecule reactions [42]. The barrier heights from the bare SOX correction are too high, as expected from the reduced KS gaps of transition states relative to those of the reactants. The poor accuracy of bare SOX reflects the fact that the

SOX coupling-strength integrand is linear in α (see Equation (2.2) and Table 2.1); thus, bare SOX only works for very weakly correlated systems such as the uniform electron gas in the high-density limit or weak interactions of closed-shell systems at large separation, but falls short even for the slightly stronger correlations present in the transition states in our test calculations.

More extensive tests using different basis sets are summarized in Table S1 in the Supporting information of Reference [78]. The basis set convergence for RPA and AXK is significantly slower than that for semilocal DFT; as a result, basis sets of at least triple-ζ quality are required to make an AXK calculation of energy differences worthwhile.

Diels–Alder Reaction Energies

A Diels–Alder (DA) reaction is an example of pericyclic reaction and involves concertedly breaking and forming π and σ bonds. Semilocal DFT predicts DA reaction energies that are less exothermic than those of explicitly correlated coupled-cluster calculations at CBS limit [135, 138]. It has been suggested that the errors are due to self-interaction [138] and intramolecular dispersion interactions[144]. RPA has been shown to be quite accurate for DA reaction energies; however, the RPA+ short-range semilocal correction method[95] and SOSEX lead to systematic over- and underestimation, respectively [144].

In Table 2.6, we present reaction energy calculations on a set of 14 DA reactions (the DARC benchmark) [138, 139]. We note in passing that basis sets of at least triple-ζ quality are necessary for RPA-type calculations, as shown in Table S2 in the Supporting Information of Reference [78]. As with the results in Reference [138], semilocal DFT calculations with the TPSS functional overestimate the DA reaction energies. The description of dispersion interactions is indeed important as indicated by the TPSS calculations with the D3 dispersion correction. The RPA reaction energies are within chemical accuracy, reflecting that RPA

Table 2.6: Errors of calculated reaction energies in kcal/mol using the QZVPP basis set for the DARC benchmark set [138, 139] relative to explicitly correlated coupled-cluster results from Reference [135].

	Ref.	TPSS	TPSS-D3	RPA	AXK	SOSEX	SOX
1	−45.4	9.23	6.22	0.91	0.31	−4.83	−22.07
2	−60.8	4.66	2.88	1.06	0.05	−4.88	−22.32
3	−29.9	9.49	5.96	−0.24	0.33	−3.12	−15.24
4	−33.6	5.00	2.69	−0.73	−0.03	−2.51	−12.23
5	−37.6	10.64	6.55	0.30	0.42	−3.78	−18.12
6	−49.0	5.90	3.07	0.35	0.07	−3.85	−17.74
7	−14.0	14.36	8.98	−0.96	0.52	−1.58	−10.53
8	−15.9	14.32	9.28	−0.79	0.47	−1.82	−11.25
9	−16.8	14.47	8.97	−0.78	0.56	−1.87	−12.06
10	−18.9	14.28	9.11	−0.53	0.60	−1.99	−12.58
11	−31.7	14.40	8.52	−0.92	0.01	−3.52	−16.77
12	−32.2	14.05	8.26	−0.70	0.18	−3.35	−16.53
13	−34.2	14.47	8.46	−0.65	0.13	−3.72	−18.23
14	−34.6	14.10	8.22	−0.42	0.30	−3.56	−17.99
ME		11.38	6.94	−0.29	0.28	−3.17	−15.98
MAE		11.38	6.94	0.67	0.29	3.17	15.98
MXE		14.47	9.28	1.06	0.60	4.88	22.32

adequately accounts for dispersion interactions and reduces self-interaction error through the exact first-order exchange. Nevertheless, RPA slightly underestimates energies of the reactions that yield bicyclic and tricyclic products with close-lying bridgehead carbons (Reactions 3, 4, 7-14) while overestimating the others. AXK almost uniformly improves upon RPA, reducing the MAE from 0.67 kcal/mol of RPA to 0.29 kcal/mol. The AXK errors are positive except for Reaction 4, for which the AXK error is almost zero. SOSEX, on the other hand, worsens the RPA reaction energies, leading to appreciable negative errors. The SOSEX results are in line with Reference [144], wherein only the first four reactions in the DARC benchmark set were investigated. Bare SOX dramatically underestimates the reaction energies, thus providing another example of the inadequacy of low-order perturbation theory for pericyclic reactions [145]. The trends of SOSEX and SOX errors are similar. This suggests that the screening in SOSEX is too weak to sufficiently correct bare SOX, which becomes unphysical for higher coupling strengths.

Noncovalent Interaction Energies

The accurate prediction of noncovalent interactions is important for, e.g., diastereoselective reactions [146]. Accuracy within a fraction of kcal/mol is often desired for these weak interactions, posing a challenging requirement for electronic structure methods. Here we test our implementations on n-alkane dimers in the ADIM6 benchmark set [7]. Basis set extrapolations using the Dunning basis sets were performed to investigate basis set convergence since RPA noncovalent interaction energies have been shown to be strongly affected by basis set incompleteness [147].

Table 2.7: Errors of calculated noncovalent interaction energies in kcal/mol using the QZVPP basis set and 3-4 extrapolated complete basis set (CBS) limit for n-alkane dimers in the ADIM6 benchmark set [7] relative to explicitly correlated coupled-cluster results in Reference [135].

Dimer	Ref.	TPSS	TPSS-D3	RPA	AXK	SOSEX	SOX
			QZVPP				
$(C_2H_6)_2$	1.34	−1.76	0.22	−0.31	−0.27	−0.29	−0.38
$(C_3H_8)_2$	1.99	−2.71	0.27	−0.37	−0.33	−0.36	−0.51
$(C_4H_{10})_2$	2.89	−4.03	0.38	−0.50	−0.46	−0.50	−0.72
$(C_5H_{12})_2$	3.78	−5.32	0.41	−0.63	−0.57	−0.63	−0.91
$(C_6H_{14})_2$	4.60	−6.59	0.56	−0.68	−0.62	−0.69	−1.05
$(C_7H_{16})_2$	5.55	−8.05	0.40	−0.80	−0.73	−0.80	−1.21
ME		−4.75	0.37	−0.55	−0.50	−0.54	−0.79
MAE		4.75	0.37	0.55	0.50	0.54	0.79
MXE		8.05	0.56	0.80	0.73	0.80	1.21
			3-4 CBS limit				
$(C_2H_6)_2$	1.34			−0.33	−0.28	−0.28	
$(C_3H_8)_2$	1.99			−0.51	−0.42	−0.43	
$(C_4H_{10})_2$	2.89			−0.73	−0.61	−0.62	
$(C_5H_{12})_2$	3.78			−0.95	−0.79	−0.79	
$(C_6H_{14})_2$	4.60			−1.11	−0.92	−0.92	
$(C_7H_{16})_2$	5.55			−1.34	−1.10	−1.09	
ME				−0.83	−0.69	−0.69	
MAE				0.83	0.69	0.69	
MXE				1.34	1.10	1.09	

As shown in Tables 2.7, RPA, AXK, and SOSEX give similar results, with the AXK and

SOSEX results being slightly more accurate than those of RPA. For all the three methods, the AVTZ basis set overbinds the dimers and yields larger errors for larger systems, while the AVQZ basis set fortuitously gives consistently small errors for all systems (Results of AVTZ and AVQZ calculations are provided in Table S3 in the Supporting Information of Reference [78]). In the 3-4 extrapolated CBS limit, the MAEs are below 62%, 51%, and 51% of the smallest interaction energy within the benchmark set for RPA, AXK, and SOSEX, respectively. Table 2.7 also lists the results using the QZVPP basis set. Similar to the RPA case [147], the Karlsruhe quadruple-ζ basis sets provide a good balance between computational cost and accuracy for most practical calculations.

Charged Dimer Dissociation Energies

To assess the magnitude of self-correlation error in RPA and beyond-RPA methods, dissociation energies of radical cations of symmetric dimers contained in the SIE4x4 benchmark set [135] were computed at various inter-monomeric distances, see Table 2.8. In these radical cations, the positive charge is excessively delocalized in semilocal DFT, producing overbinding and artificial barriers along the potential energy surface [148]. The errors are particularly large for stretched dimers, reflecting incorrect fractional charges [149] in the semilocal DFT picture. RPA removes self-interaction to the first order due to exact first-order exchange, but the missing higher-order terms in the RPA correlation energy still cause significant self-correlation error. The AXK results are consistently more accurate than the semilocal DFT and RPA ones. In particular, AXK remains fairly accurate close to the equilibrium structures. SOSEX is constructed to be one-electron self-correlation-free. Indeed, SOSEX is nearly exact for H_2^+; the small errors result from the use of TPSS densities to evaluate the energy. The SOSEX dissociation energies are also more accurate at large dimer separations. Nevertheless, SOSEX is less accurate than RPA and AXK for the dissociations of $(NH_3)_2^+$ and $(H_2O)_2^+$ close to the equilibrium inter-monomeric distances. This illustrates that freedom

Table 2.8: Errors of calculated dissociation energies in kcal/mol using the QZVPP basis set for positively charged dimers in the SIE4x4 benchmark set [135]. The reference is explicitly correlated coupled cluster theory [135]. For each dimer, calculations were performed at four different inter-monomeric distances d_{MM} measured by the ratio $d_{\mathrm{MM}}/d^0_{\mathrm{MM}}$, where d^0_{MM} is the equilibrium distance.

$d_{\mathrm{MM}}/d^0_{\mathrm{MM}}$	Ref.	TPSS	TPSS-D3	RPA	AXK	SOSEX	SOX
			$(\mathrm{H}\cdots\mathrm{H})^+$				
1.00	64.4	4.82	4.82	3.42	0.83	−0.48	−2.56
1.25	58.9	7.81	7.81	4.99	1.75	−0.92	−5.60
1.50	48.7	11.23	11.24	8.22	3.71	−1.48	−12.08
1.75	38.3	14.91	14.95	15.75	9.11	−2.25	−33.41
			$(\mathrm{He}\cdots\mathrm{He})^+$				
1.00	56.9	25.53	25.53	14.49	5.70	−3.30	−21.99
1.25	46.9	32.40	32.41	26.39	13.96	−6.64	−66.59
1.50	31.3	40.39	40.45	41.83	27.94	−9.91	−181.69
1.75	19.1	48.28	48.42	58.36	45.54	−12.47	−460.35
			$(\mathrm{H_3N}\cdots\mathrm{NH_3})^+$				
1.00	35.9	7.75	9.01	4.30	−0.59	−6.81	−25.22
1.25	25.9	14.29	15.25	11.49	4.24	−11.57	−78.69
1.50	13.4	20.42	20.98	20.83	13.09	−16.28	−232.54
1.75	4.9	25.81	26.08	30.49	23.95	−19.75	−658.38
			$(\mathrm{H_2O}\cdots\mathrm{OH_2})^+$				
1.00	39.7	14.19	15.15	7.46	0.17	−11.73	−54.22
1.25	29.1	22.48	23.37	18.43	8.88	−18.80	−178.55
1.50	16.9	29.72	30.27	30.55	21.59	−24.35	−530.66
1.75	9.3	35.32	35.59	41.33	34.38	−27.90	−1462.47
ME		22.21	22.58	21.15	13.39	−10.91	−250.31
MAE		22.21	22.58	21.15	13.46	10.91	250.31
MXE		48.28	48.42	58.36	45.54	27.90	1462.47

from one-electron self-interaction does not necessarily translate to many-electron systems [150, 151].

Radical cations at stretched inter-monomeric distances are highly challenging for beyond-RPA perturbative methods, as reflected by the AXK and SOSEX MAEs being greater than 10 kcal/mol for the SIE4x4 benchmark. The catastrophic failure of bare SOX for these systems also suggests that perturbative corrections are inadequate here, and points to a

need for self-consistent approaches [152].

Transition-Metal Compound Dissociation Energies

Finally, we assess the implemented methods using a set of $3d$ transition-metal dissociation reactions proposed in Reference [123]. This benchmark contains dissociation reactions of 22 transition-metal compounds that represent diverse types of transition-metal bonding. Many species involved in these reactions are small-gap open-shell systems, which provide a demanding test for electronic structure methods. The reference values are based on high-quality experimental data and are corrected for zero-point and thermal vibrational energies and scalar-relativistic effects.

All calculations were performed using TPSS structures reported in Reference [123] except for Fe_2Cl_4 and $CoCl_3$, for which D_{2h} and D_{3h} structures, respectively, were found to yield lower ground-state energies [153]. As summarized in Table 2.9, the accuracy of each method varies considerably with different types of compounds. The TPSS results confirm that the errors from meta-GGA calculations are around 10 kcal/mol per bond [123]. In general, RPA reduces the errors, but there exist cases where RPA gives less accurate results than TPSS, e.g., metal dimers. The AXK MAE is slightly higher than that of RPA, yet this deterioration is due to only a few types of molecules, as will be discussed below. In general, AXK performs well if the corresponding RPA error is already small. SOSEX and SOX are generally less accurate than AXK.

For RPA and the beyond-RPA methods, the metal dimers give rise to the largest errors in the predicted dissociation energies. These dimers, Sc_2, V_2, and Ni_2, exhibit strong static correlation due to the left-right effect and the near degeneracy of the $4s$ and $3d$ subshells. [154] For these systems, semilocal functionals such as TPSS give relatively accurate results in comparison with hybrid functionals[123] and RPA. This trend is related to the XC hole

being short ranged for systems with strong static correlation[155]. The deficiency of RPA in accounting for strong static correlation renders it a poor starting point for perturbative corrections. Consequently, the AXK corrections are in the wrong direction, and both SOSEX and SOX give qualitatively wrong results.

Another type of molecules where the AXK error is significantly larger than that of RPA is the monoxides, particularly MnO. Again, SOSEX and SOX errors are even larger. This trend is consistent with previous calculations on metal monoxides with structures optimized using each respective method. Nevertheless, Reference [42] points out that although AXK worsens RPA for dissociation energies, the former leads to smaller errors in bond lengths and frequencies.

Somewhat surprisingly, for CoH dissociation, bare SOX is more accurate than AXK and SOSEX; A similar trend is observed for the homolytic dissociation of ferrocene, $1/2\mathrm{FeCp}_2 \rightarrow 1/2\mathrm{Fe} + \mathrm{Cp}$. The good accuracy of bare SOX in these cases might result from fortuitous cancellation of higher-order corrections which is incompletely captured by AXK and SOSEX. To further understand this result, we consider the heterolytic dissociation energy of ferrocene, i.e. $1/2\mathrm{FeCp}_2 \rightarrow 1/2\mathrm{Fe}^{2+} + \mathrm{Cp}^{-}$, where the experimental value after correcting for scalar-relativistic, zero-point vibrational, and thermal energies is 318 kcal/mol [156]. With the QZVPP basis set, RPA overestimates the homolytic dissociation energy by 6.8 kcal/mol, while AXK and SOSEX underestimate by 4.4 kcal/mol and 13.8 kcal/mol, respectively. Unlike the homolytic ferrocene dissociation, the heterolytic dissociation energy is severely underestimated by bare SOX, which yields an error of -64.2 kcal/mol. The magnitude of the SOX error is comparable to that of the MP2 CBS calculation in the literature, which is 59 kcal/mol too high. [157] The large negative SOX error suggests that ferrocene is relatively strongly correlated, and thus confirms the error cancellation in the SOX calculation for the homolytic ferrocene dissociation.

Table 2.9: Errors of calculated dissociation energies in kcal/mol for the $3d$ transition-metal reference set relative to back-corrected experimental values from Reference [123].

Reaction	Ref.	TPSS	TPSS-D3	RPA	AXK	SOSEX	SOX
			QZVPP				
$Sc_2 \rightarrow 2Sc$	39.8	−7.51	−7.47	−19.70	−32.43	−48.16	−158.78
$V_2 \rightarrow 2V$	64.6	−0.12	−0.12	−15.97	−34.60	−60.93	−293.63
$Ni_2 \rightarrow 2Ni$	49.7	8.31	8.34	−11.80	−33.72	−84.57	−803.58
$CrH \rightarrow Cr+H$	45.7	11.72	11.72	6.75	6.06	2.41	−8.65
$MnH \rightarrow Mn+H$	32.3	20.04	20.07	3.19	1.77	2.06	3.43
$CoH \rightarrow Co+H$	46.6	17.87	17.88	14.41	16.47	13.87	2.91
$TiO \rightarrow Ti+O$	158.8	17.37	17.37	0.40	−3.28	−9.85	−49.01
$MnO \rightarrow Mn+O$	91.1	29.21	29.21	−6.01	−20.00	−35.52	−107.22
$CuO \rightarrow Cu+O$	63.7	9.49	9.49	−0.90	−5.91	−17.75	−71.73
$ScF \rightarrow Sc+F$	143.0	8.44	8.44	−6.00	−5.65	−7.20	−20.11
$CrF \rightarrow Cr+F$	105.1	12.82	12.83	1.71	1.72	−0.84	−15.39
$CuF \rightarrow Cu+F$	102.5	−2.91	−2.90	−11.73	−10.02	−12.23	−27.84
$Fe_2Cl_4 \rightarrow 2FeCl_2$	35.0	−8.29	−6.42	−3.79	−1.86	−0.07	4.09
$CoCl_3 \rightarrow \frac{1}{2}Cl_2+CoCl_2$	16.7	9.48	10.50	1.71	−9.78	−21.24	−90.46
$Fe(CO)_5 \rightarrow Fe(CO)_4+CO$	42.2	4.31	6.00	−3.07	−2.73	1.50	15.97
$Ni(CO)_4 \rightarrow Ni(CO)_3+CO$	24.9	3.95	5.17	−0.36	−2.75	−2.71	−14.08
$\frac{1}{2}CrBz_2 \rightarrow \frac{1}{2}Cr+Bz$	31.8	6.90	10.06	8.75	3.13	−2.72	−37.84
$\frac{1}{2}FeCp_2 \rightarrow \frac{1}{2}Fe+Cp$	80.1	14.67	18.61	11.88	8.25	8.62	6.65
ME		8.65	9.38	−1.70	−6.96	−15.30	−92.51
MAE		10.75	11.26	7.12	11.12	18.46	96.19
MXE		29.21	29.21	19.70	34.60	84.57	803.58
			3-4 CBS limit				
$Sc_2 \rightarrow 2Sc$	39.8			−20.52	−32.57	−48.04	
$V_2 \rightarrow 2V$	64.6			−16.88	−28.71	−55.50	
$Ni_2 \rightarrow 2Ni$	49.7			−11.42	−32.15	−82.81	
$CrH \rightarrow Cr+H$	45.7			4.01	5.46	2.18	
$MnH \rightarrow Mn+H$	32.3			3.23	1.45	1.76	
$CoH \rightarrow Co+H$	46.6			15.54	18.52	13.23	
$TiO \rightarrow Ti+O$	158.8			2.51	−0.62	−7.01	
$MnO \rightarrow Mn+O$	91.1			−3.63	−16.73	−32.16	
$CuO \rightarrow Cu+O$	63.7			−2.09	−5.80	−17.46	
$ScF \rightarrow Sc+F$	143.0			−5.33	−4.68	−6.09	
$CrF \rightarrow Cr+F$	105.1			0.56	2.27	0.05	
$CuF \rightarrow Cu+F$	102.5			−11.36	−9.25	−11.35	
$Fe_2Cl_4 \rightarrow 2FeCl_2$	35.0			−1.94	0.13	1.47	
$CoCl_3 \rightarrow \frac{1}{2}Cl_2+CoCl_2$	16.7			0.67	−10.39	−21.75	
$Fe(CO)_5 \rightarrow Fe(CO)_4+CO$	42.2			−4.37	−3.54	0.81	
$Ni(CO)_4 \rightarrow Ni(CO)_3+CO$	24.9			−4.56	−5.64	−5.37	
$\frac{1}{2}CrBz_2 \rightarrow \frac{1}{2}Cr+Bz$	31.8			0.32	−0.66	−5.70	
$\frac{1}{2}FeCp_2 \rightarrow \frac{1}{2}Fe+Cp$	80.1			8.53	6.82	7.41	
ME				−2.60	−6.45	−14.80	
MAE				6.53	10.30	17.79	
MXE				20.52	32.57	48.04	

2.6 Discussion

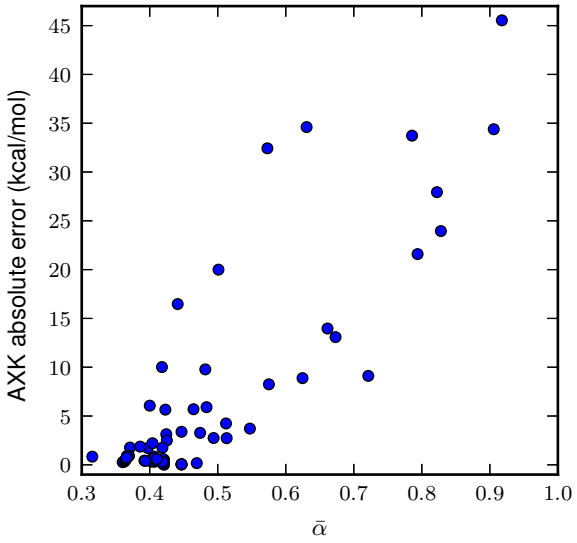

Figure 2.4: Correlation between the absolute error of AXK and the $\bar{\alpha}$ value for all the QZVPP energy difference calculations for the BHDIV10, DARC, ADIM6, and SIE4x4 benchmark sets [135] as well as the $3d$ transition-metal reference set [123]. Reprinted with permission from Reference [78], Copyright 2018 American Chemical Society.

The above results suggest a simple explanation for when and why perturbative corrections to RPA break down: At higher coupling strength, any low-order corrections and RPA itself eventually become unphysical. A qualitative measure of correlation strength is the relative difference between the AXK and SOX beyond-RPA correlation energies,

$$\bar{\alpha} = \frac{\Delta E^{\text{C SOX}} - \Delta E^{\text{C AXK}}}{\Delta E^{\text{C SOX}}}. \tag{2.13}$$

$\bar{\alpha}$ is non-negative and goes to zero as AXK approaches SOX for small coupling. With increasing coupling strength, AXK but not SOX is screened, giving rise to more positive $\bar{\alpha}$ values. $\bar{\alpha}$ may be understood as an effective average coupling strength for beyond-RPA correlation. This concept may be extended to energy differences by defining $\bar{\alpha}$ as the maximum of the individual $\bar{\alpha}$ values of all involved species.

Figure 2.4 shows that $\bar{\alpha}$ is positively correlated with the absolute error of AXK. When $\bar{\alpha}$

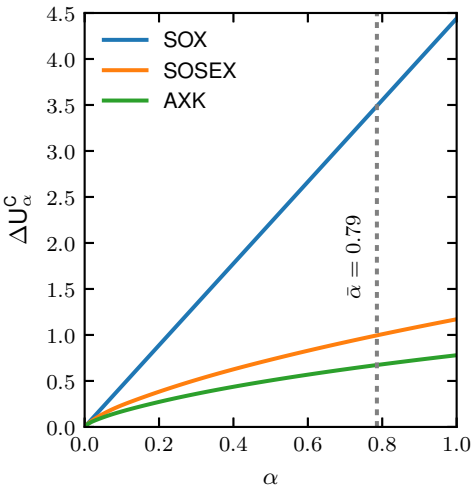

Figure 2.5: Coupling-strength dependence of $\Delta U_\alpha^{\mathrm{C\ AXK}}$, $\Delta U_\alpha^{\mathrm{C\ SOSEX}}$, and $\Delta U_\alpha^{\mathrm{C\ SOX}}$ for Ni_2. The area under each curve is the beyond-RPA correlation energy of the corresponding method. The AXK and SOSEX calculations were performed with a 7-point Gauss–Legendre coupling-strength quadrature using the QZVPP basis set. The effective coupling strength $\bar{\alpha}$ equals the relative difference of the area under the SOX and AXK curves. Reprinted with permission from Reference [78], Copyright 2018 American Chemical Society.

is greater than 0.5, the SOX beyond-RPA correlation energy is more than twice of that of AXK. For such systems, AXK typically does not deliver acceptable accuracy. This suggests that $\bar{\alpha}$ may be used as a diagnostic for the reliability of AXK.

Large $\bar{\alpha}$ values, however, do not always imply incorrect results: For the first CO dissociation of $Fe(CO)_5$ and the homolytic dissociation of ferrocene, the $\bar{\alpha}$ values are 0.51 and 0.58, but the AXK errors are -2.71 kcal/mol and 8.62 kcal/mol, respectively. This unexpectedly good accuracy of AXK for these two reactions may be attributed to error cancellation between the reactants and the products.

Ni_2 exhibits an $\bar{\alpha}$ value of 0.79, the largest among all species in the $3d$ transition-metal reference set. (Even higher $\bar{\alpha}$ values are observed for charged dimers in the SIE4x4 benchmark set, but not at equilibrium distances.) The coupling-strength integrands $\Delta U_\alpha^{\mathrm{C}}$ of the beyond-RPA correlation energy of Ni_2 for SOX, SOSEX, and AXK are plotted in Figure 2.5; the

total beyond-RPA correlation energy is the coupling strength average [13, 158]

$$\Delta E^{\mathrm{C}} = \int_0^1 \mathrm{d}\alpha \Delta U_\alpha^{\mathrm{C}}. \tag{2.14}$$

Although the $\Delta U_\alpha^{\mathrm{C\,AXK}}$ curve tends to the linear SOX integrand at $\alpha = 0$, it is rapidly screened at larger coupling strength, which is reflected in the high value of $\bar{\alpha}$. Figure 2.5 also reveals a simple geometrical meaning of $\bar{\alpha}$: It measures the relative difference of the area under the SOX and AXK coupling strength integrands. For Ni_2, even the strong AXK screening is insufficient, as reflected in the large AXK error of the Ni_2 binding energy.

2.7 Conclusions

Two efficient and robust implementations of the AXK methods using the RI approximation and numerical frequency integration were presented: The AO based $\mathcal{O}(N^4 \ln N)$ algorithm is fast for molecules of over 200 atoms with small basis sets, while the MO based $\mathcal{O}(N^5 \ln N)$ algorithm enables calculations on a single workstation computer for molecules of around 100 atoms with triple- and quadruple-ζ basis sets, which are necessary for accurate energy difference predictions. The bare SOX and SOSEX beyond-RPA correlation energies can also be computed using these algorithms, facilitating comparison of these methods for large systems.

The AXK method yields improved accuracy for ground-state energy differences of systems with relatively weak correlation: Systematic improvement over RPA is observed for reaction barrier heights, reaction energies, and noncovalent interaction energies of main-group compounds. In these benchmarks, AXK reduces RPA errors by 25-50% and outperforms SOSEX. In particular, for the DARC benchmark, the AXK errors are less than half of the RPA errors on average and are an order of magnitude lower than those of SOSEX. These systems

are characterized by relatively small average coupling strengths $\bar{\alpha}$, and thus perturbative corrections are viable. For these weakly correlated systems, including higher-order terms in the geometric series expansion of Equation (1.33), along the lines recently proposed by Bates and co-workers [158], is likely to yield further accuracy gains. The increased computational effort of AXK compared with bare RPA may be particularly worthwhile for systems with small but non-negligible $\bar{\alpha}$ values, where bare perturbation theory such as MP2 is insufficient and coupled cluster methods are too costly.

For systems with strong correlation, indicated by effective coupling strength values of 0.5 or above, perturbative beyond-RPA corrections break down, because the underlying assumption that "XC kernel corrections" are small is no longer justified. Indeed, RPA itself relies on this assumption, and becomes an increasingly unphysical reference with increasing coupling strength. Such strongly correlated systems include transition metal compounds exhibiting strong static correlations or metallic systems at low electron density.

An additional source of errors independent of the effective coupling strength is inaccuracies in the KS input orbitals, or "density-driven errors" [159]. These types of errors are addressed by variational self-consistent approaches such as generalized KS RPA [152].

Chapter 3

Computational Studies of Rare-Earth and Actinide Complexes with Unconventional Oxidation States

This chapter contains verbatim excerpts from several published works. Sections 3.1 and 3.4 contain excerpts, reprinted with permission, from C. J. Windorff, G. P. Chen, J. N. Cross, W. J. Evans, F. Furche, A. J. Gaunt, M. T. Janicke, S. A. Kozimor, and B. L. Scott, *J. Am. Chem. Soc.* **139**, 3970–3973, 2017. Section 3.2 consists of excerpts, reprinted with permission, from D. H. Woen, G. P. Chen, J. W. Ziller, T. J. Boyle, F. Furche, and W. J. Evans, *Angew. Chem. Int. Ed.* **56**, 2050–2053, 2017. Section 3.3 consists of excerpts, reprinted with permission, from D. H. Woen, G. P. Chen, J. W. Ziller, T. J. Boyle, F. Furche, and W. J. Evans, *J. Am. Chem. Soc.* **139**, 14861–14864, 2017. The material in this chapter is based upon work supported by the National Science Foundation under CHE-1464828.

3.1 Introduction

One critical step in characterizing the chemical behavior of any element involves establishing its range of accessible oxidation states. Such understanding provides crucial information for predicting chemical behavior and physical properties. Oxidation state diversity is central to the chemistry and physics of an element. Studies defining accessible oxidation states have been pursued for over 100 years. Indeed, the boundaries of oxidation states are often presumed to be established, and new oxidation states are not expected.

Lanthanide (Ln) elements typically occur in the +3 oxidation state with $4f^n$ electron configurations [160]. The compact and low-lying $4f$ orbitals in the Ln^{3+} ions are only weakly perturbed by the chemical environment, leading to mostly ionic bonding [161]. This traditional view of lanthanides was overturned by Lappert and co-workers [162] and by Evans and co-workers [163, 164], as Ln^{2+} complexes were discovered for the entire lanthanide series, excluding promethium. Unlike the previously known Ln^{2+} ions with $4f^{n+1}$ configurations, the newly discovered Ln^{2+} ions, La^{2+}, Ce^{2+}, Pr^{2+}, Gd^{2+}, Tb^{2+}, Ho^{2+}, Er^{2+}, Lu^{2+}, are stabilized by the occupation of a $5d_{z^2}$ orbital in tris(cyclopentadienyl) coordination environment [162–166]. Consequently, these new Ln^{2+} ions are more transition-metal-like and exhibit unique physical and chemical properties [167].

The discovery of the non-traditional lanthanide +2 ions has raised interest in the search of new oxidation states of other metals. This chapter presents two new ions, Sc^{2+} and Pu^{2+}, with a focus on the role electronic structure calculations played in their identification. In Section 3.2, the first crystallographically characterized Sc^{2+} complex, $[Sc(NR_2)_3]^-$ ($R = SiMe_3$), is introduced. Consistent with the experimental EPR spectrum, DFT calculations indicate a $3d^1$ ground state, which is analogous to the Ln^{2+} complexes with $4f^n5d^1$ metal valence configurations. The $[Sc(NR_2)_3]^-$ complex exhibits unusual chemical reactivity, e.g., the reduction of N_2 to form an end-on $(N{=}N)^{2-}$ complex of Sc^{3+}, $\{[(R_2N)_3Sc]_2[\mu\text{-}\eta^1{:}\eta^1\text{-}N_2]\}^{2-}$, as

shown in Section 3.3. Section 3.4 presents the first crystallographically characterized Pu^{2+} complex, $[PuCp"_3]^-$, Cp" = $C_5H_3(SiMe_3)_2$. Evidence provided by DFT calculations is important for the identification of the formal +2 oxidation state of Pu. This discovery, along with the more recent discovery of Np^{2+} [168], expands the examples of actinide (An) analogs of the new Ln^{2+} complexes. Theoretical calculations indicate more variable $6d$ occupations in these An^{2+} complexes [168–172], providing opportunities for richer redox chemistry. The applicability of RPA and beyond-RPA methods is discussed in Section 3.5. Concluding remarks are given in Section 3.6.

3.2 A Tris(amide) $\{Sc[N(SiMe_3)_2]_3\}^-$ Complex of Non-traditional +2 Scandium Ion

3.2.1 Introduction

Scandium is attractive for theoretical studies since it has the lowest atomic number of any transition metal. However, the understanding of scandium chemistry often lags behind the other transition metals due to the experimental difficulty of working with this small electropositive element [173–184]. The +3 oxidation state is predominant for Sc in molecular complexes in solution with only six examples reported in other oxidation states: one Sc^0 complex, $Sc(\eta^6\text{-}C_6H_3{}^tBu_3)_2$ [179, 180], three Sc^+ complexes, $[\{(\eta^5\text{-}P_3C_2{}^tBu_2)Sc\}_2(\mu\text{-}\eta^6\text{:}\eta^6\text{-}P_3C_3{}^tBu_3)]$ [181], $[Sc(\eta^5\text{-}P_3C_2{}^tBu_2)(\mu\text{-}\eta^2\text{:}\eta^5\text{-}P_3C_2{}^tBu_2)Sc(\eta^5\text{-}P_3C_2{}^tBu_2)]$ [182], and $(LMgBr)_2ScBr$ (L = $Et_2NCH_2CH_2NC(Me)CHC(Me)NCH_2CH_2NEt_2$) [183], and two Sc^{2+} complexes, $Sc(\eta^6\text{-}C_6H_3{}^tBu_3)[\eta^6,\eta^1\text{-}{}^tBu_2(CMe_2CH_2)C_6H_3]H$ [179], and $Sc(\eta^5\text{-}P_2C_3{}^tBu_3)_2$ [184], both of which were obtained via electron beam vaporization of Sc^0 into cryogenic matrices. Structural characterization was only possible on the Sc^0 and Sc^+ complexes; no Sc^{2+} complexes characterized by X-ray diffraction are in the literature.

Recently, the +2 oxidation state has been successfully identified in molecular complexes of all the other rare earth metals, that is, Y and the lanthanides (except radioactive Pm) [162, 164–167]. This has been accomplished by LnA_3/M reactions (Ln = rare earth metal; A = anionic ligand; M = alkali metal) involving reductions of tris(silylcyclopentadienyl) complexes, that is, A=$C_5H_4SiMe_3$ and $C_5H_3(SiMe_3)_2$, as shown in Figure 3.1.

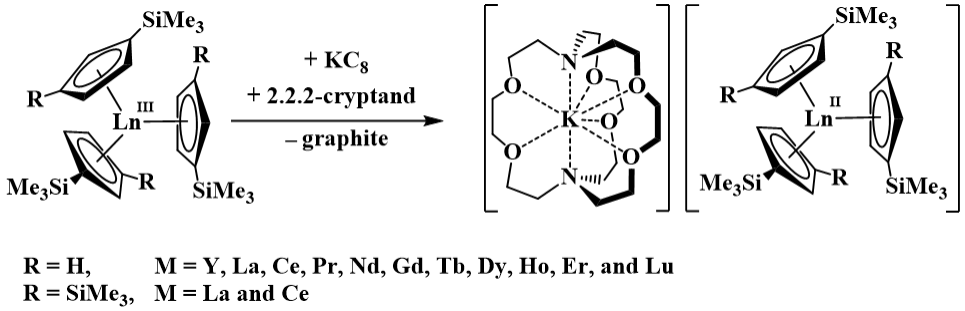

R = H, M = Y, La, Ce, Pr, Nd, Gd, Tb, Dy, Ho, Er, and Lu
R = $SiMe_3$, M = La and Ce

Figure 3.1: Synthesis of tris(silylcyclopentadienyl) complexes of Ln^{2+}.

It was of interest to extend the series of structurally characterized complexes of these new Ln^{2+} ions to the one remaining rare earth metal ion which had not yet been identified crystallographically, Sc^{2+}. However, accessing the analogous "$Sc(C_5H_4SiMe_3)_3$" and "$Sc[C_5H_3(SiMe_3)_2]_3$" precursors could be problematic since the ionic radius of Sc^{3+} is 0.107 Å shorter than that of Lu^{3+} [185] and the preparation of $Lu(C_5H_4SiMe_3)_3$ is already challenging due to steric crowding [186]. Moreover, the structure of the tris(cyclopentadienyl) Sc^{3+} complex, $[(\eta^5\text{-}C_5H_5)_2Sc(\mu\text{-}\eta^1\text{:}\eta^1\text{-}C_5H_5)]_n$ [187], suggests that "$Sc(C_5H_4SiMe_3)_3$" and "$Sc[C_5H_3(SiMe_3)_2]_3$" may not form the same trigonal coordination environment of all the examples in Figure 3.1.

The bis(trimethylsilyl)amide complex, $Sc(NR_2)_3$ (R=$SiMe_3$) [188], was not initially considered as a precursor to Sc^{2+} since previous LnA_3/M reactions with A=NR_2 did not allow isolation of Ln^{2+} complexes. Instead, these $Ln(NR_2)_3$ reduction reactions generated reduced dinitrogen complexes containing $(N{=}N)^{2-}$, Figure 3.2, and $N_2{}^{3-}$ moieties [166, 167, 189–192].

Although DFT studies of $Y(NR_2)_3$ showed that both the LUMO of the trivalent complex,

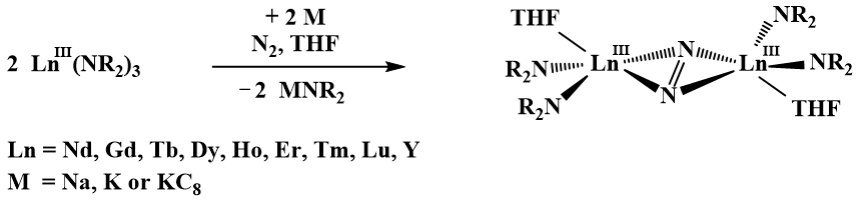

Figure 3.2: Generation of side-on $(N{=}N)^{2-}$ complexes of Ln^{3+}.

$Y(NR_2)_3$, and the HOMO of the reduced species, $[Y(NR_2)_3]^-$, have primarily d_{z^2} character [193], only EPR data were obtainable on a transient Y^{2+} species [194]. The reduction of the Sc analog, $Sc(NR_2)_3$, on the other hand, yielded X-ray quality crystals of $[K(crypt)][Sc(NR_2)_3]$, $[K(18\text{-}c\text{-}6)][Sc(NR_2)_3]$, and $[Cs(crypt)][Sc(NR_2)_3]$. The reactions are summarized in Figure 3.3. The synthesis and experimental characterization of $[Sc(NR_2)_3]^-$ are detailed in Reference [195]. This section focuses on the computational characterization of $[Sc(NR_2)_3]^-$.

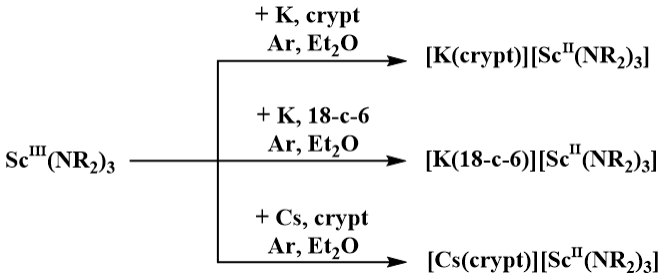

Figure 3.3: Reduction reactions of $Sc(NR_2)_3$.

3.2.2 Computational Details

DFT calculations were performed using the hybrid meta-GGA functional TPSSh [122] with Grimme's D3 dispersion correction [7] and basis sets of triple-zeta plus polarization (def2-TZVP) quality [61]. Fine numerical grids of size m4 [64] were used. The $Sc(NR_2)_3$ and $[Sc(NR_2)_3]^-$ structures were optimized in C_1 and D_3 symmetry, respectively. The maximum norm of the Cartesian coordinate gradient was converged to $\leq 10^{-4}$ a.u. Vibrational normal mode analyses using numerical second derivatives were carried out to confirm that the op-

timized structures are minima on the ground-state potential energy surface. The electronic ground state of $Sc(NR_2)_3$ is closed-shell. For the spin-unrestricted calculation on the $^2A_1$ ground state of $[Sc(NR_2)_3]^-$, the expectation value of $\hat{S}^2$ is 0.752, indicating negligible spin contamination. Solvent effects were included by the continuum solvation model (COSMO) [196] with dielectric constant 7.52 [197] and index of refraction 1.4050 [198] of THF. All calculations were performed using TURBOMOLE 7.0 and 7.1 [25].

The UV-visible spectrum of $[Sc(NR_2)_3]^-$ was simulated using TDDFT with the latest implementation of nonorthonormal Krylov subspace methods [199]. The gauge-invariant implementation of the TPSSh functional was employed [200]. def2-TZVP basis sets were used without diffuse functions because test calculations showed that a diffuse p function on Sc produced spurious unoccupied a_2 orbitals extending outside the COSMO cavity. def2-TZVP has been shown to provide accurate excitation energies in previous benchmark calculations [201]. Very fine numerical grid of size 5 [64] was used in the TDDFT calculations. The absorption spectrum was simulated by superimposing Gaussian functions with a standard deviation of 0.34 eV (Figure 3.5).

3.2.3 Results and Discussions

Table 3.1: Comparison of structural parameters for $Sc(NR_2)_3$ and $[Sc(NR_2)_3]^-$ (in Å). **1a** and **1b** are single crystals of $Sc(NR_2)_3$ grown by slow evaporation of the Et_2O solution at room temperature overnight and by sublimation at 80 °C under 10^{-3} torr over 2 days, respectively. **2-K(crypt)** is the [K(crypt)][$Sc(NR_2)_3$] single crystal. The Sc–plane distance is the distance between the Sc atom and the plane of the three N atoms.

Complex	Structure	Average Sc–N distance	Sc–plane distance
$Sc(NR_2)_3$	**1a**	2.049	0.520
	1b	2.052	0.487
	DFT	2.047	0.482
$[Sc(NR_2)_3]^-$	**2-K(crypt)**	2.134	0.014
	DFT	2.135	0.000

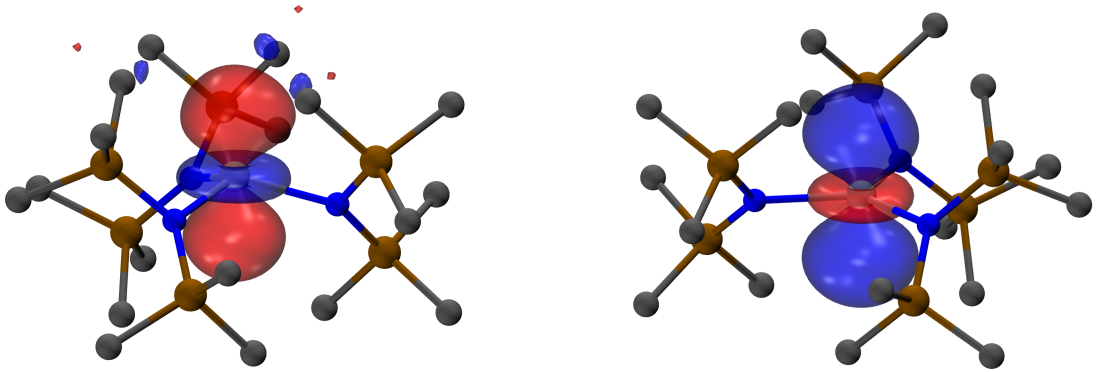

Figure 3.4: (a) LUMO of $Sc(NR_2)_3$ and (b) HOMO of $[Sc(NR_2)_3]^-$ with a contour value of 0.045. Hydrogen atoms are omitted for clarity.

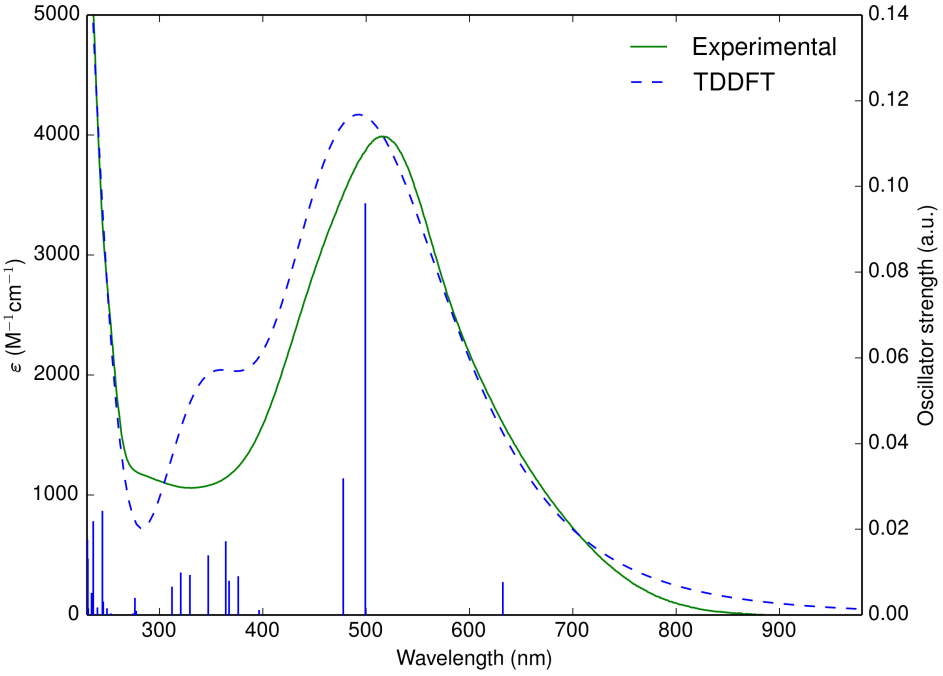

Figure 3.5: Experimental (solid) and simulated (dash) UV-visible spectra of [K(crypt)][$Sc(NR_2)_3$] in ∼3 mM THF solution at room temperature. TDDFT excitations are shown as vertical lines.

DFT geometry optimizations were performed on $Sc(NR_2)_3$ and $[Sc(NR_2)_3]^-$ and the calculated structural parameters match the pyramidal structure for $Sc(NR_2)_3$ and the planar D_3 structure for $[Sc(NR_2)_3]^-$ (Table 3.1). The frontier molecular orbitals are similar to those of the Y analogs [193]: the LUMO of the Sc^{3+} precursor and the HOMO of the reduced Sc2+

product both have d_{z^2} character (Figure 3.4). The $(3d_{z^2})^1$ ground state for $[Sc(NR_2)_3]^-$ is consistent with the experimental EPR data (see Reference [195]). The UV-visible spectra of each variant of $[Sc(NR_2)_3]^-$ exhibit an intense absorption at 516 nm with $\epsilon = 4000\ M^{-1}cm^{-1}$ similar to the spectra of the Ln^{2+} complexes shown in Figure 3.1. TDDFT calculations on $[Sc(NR_2)_3]^-$ with D_3 symmetry gave a nearly quantitative reproduction of the experimental spectrum with the observed absorption band attributed to electronic excitations at 499 nm, 478 nm, and 633 nm, in descending order of oscillator strength (Figure 3.5). These excitations correspond to transitions from the Sc-based HOMO ($27a_1$ α) to low-lying unoccupied orbitals of a_2 and e irreducible representations (Table 3.2). The weak transition at 633 nm is predominantly $d \rightarrow d$ while the more intense ones at 499 nm and 478 nm have significant $d \rightarrow$ligand character (Figure 3.6). This assignment is consistent with previous studies on $[(C_5H_4SiMe_3)_3Ln]^-$ [164, 165] showing strong absorptions due to transitions from the metal-based HOMO to ligand-based orbitals.

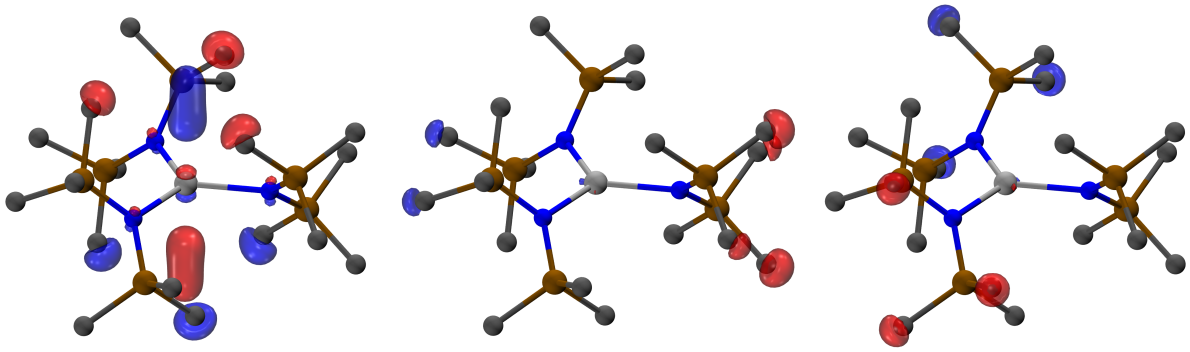

Figure 3.6: (a) $25a_2$ α and (b)(c) 49e α unoccupied orbitals of $[Sc(NR_2)_3]^-$ with a contour value of 0.045. Hydrogen atoms are omitted for clarity.

Table 3.2: Lowest electronic excitations of $[Sc(NR_2)_3]^-$ computed using TPSSh functional and def2-TZVP basis sets. Oscillator strengths are in length representation.

State	Wavelength (nm)	Oscillator Strength (10^{-2} a.u.)	Dominant contributions			Assignment
			occupied	unoccupied	contribution	
1^2E	1221	0.005	$27a_1$ α	48e α	93.4%	3d→3d
2^2E	633	0.75	$27a_1$ α	50e α	91.9%	3d→3d
1^2A_2	499	9.59	$27a_1$ α	$25a_2$ α	98.9%	3d→ligand/4p
3^2E	478	3.17	$27a_1$ α	49e α	98.8%	3d→ligand

3.3 End-On Bridging Dinitrogen Complex of Scandium

3.3.1 Introduction

The activation of small molecules such as N_2, CO_2, CO, NO, and H_2 is a crucial component of many biological, atmospheric, and industrial processes and is an active area of research for sustainable energy. The coordination chemistry of these substrates has been heavily studied in efforts to define the initial steps in the mechanisms of activation. Historically, dinitrogen activation typically involved end-on coordination of N_2 to metals in either monometallic or bimetallic complexes [202–211]. Side-on bridging was known in a few bimetallic complexes with a nonplanar butterfly geometry that allowed each metal to interact with one of the two perpendicular multiple bonds of N_2 [212–214]. In 1988, the first example of planar side-on bridging of dinitrogen was reported in the rare-earth metal complex, $[(C_5Me_5)_2Sm]_2[\mu\text{-}\eta^2\text{:}\eta^2\text{-}N_2]$ [215]. This unusual planar side-on structure became a hallmark of rare-earth metal dinitrogen chemistry with over 40 complexes reported in the Cambridge Structural Database (CSD) [178, 216–220]. Subsequently, the $M_2(\mu\text{-}\eta^2\text{:}\eta^2\text{-}N_2)$ motif was found in over 35 transition metal complexes [211] and three uranium complexes [221–223], but the end-on mode still remains more common. The relationship between reactivity and end-on vs side-on bonding of dinitrogen has been examined in several systems [203, 208, 224, 225] but not with rare-earth metals since no examples of end-on bridging dinitrogen complexes of these metals were in the literature. This section presents the first example of end-on dinitrogen coordination with a rare-earth metal and its surprising photochemistry to form a rare example of a Sc^{2+} complex. The structure and photoreactivity of the end-on dinitrogen complex are explained by DFT and TDDFT calculations. Experimental details are reported in Reference [226].

3.3.2 Computational Details

Ground-state DFT calculations were carried out using the TPSS [63] meta-generalized-gradient-approximation (meta-GGA) functional with Grimme's D3 dispersion correction [7, 227]. Two different basis sets (def2-SV(P) [228] and def2-TZVP [61]) were used for $\{[(R_2N)_3Sc]_2[\mu\text{-}\eta^1\text{:}\eta^1\text{-}N_2]\}^{2-}$; The differences in the optimized bond distances are within 0.01 Å. Density grids of m4 or larger [64] were employed. The structure of $\{[(R_2N)_3Sc]_2[\mu\text{-}\eta^1\text{:}\eta^1\text{-}N_2]\}^{2-}$ was optimized in D_3 symmetry with convergence criterion for maximum norm of Cartesian energy gradient set to 10^{-4} a.u. Spin-unrestricted calculations suggest a triplet ($^3A_2$) ground state with a squared total spin expectation value of 2.003, which indicates negligible spin contamination. For comparison, hypothetical side-on complexes $\{[(R_2N)_3Sc]_2[\mu\text{-}\eta^2\text{:}\eta^2\text{-}N_2]\}^{2-}$ and $\{[(R_2N)_2Sc(THF)]_2[\mu\text{-}\eta^2\text{:}\eta^2\text{-}N_2]\}$ were optimized in C_2 and C_i symmetries, respectively, using def2-SV(P) basis set. For the anionic complexes, the COSMO continuum solvation model [196] was employed to account for the THF solvent using dielectric constant of 7.52 [197] and refractive index of 1.4050 [198]. The COSMO cavity was constructed using atomic radii of 1.300 Å, 2.000 Å, 1.830 Å, 2.200 Å, and 2.223 Å for H, C, N, Si, and Sc, respectively, and solvent radius of 3.18 Å. Structure optimization of the neutral complex $\{[(R_2N)_2Sc(THF)]_2[\mu\text{-}\eta^2\text{:}\eta^2\text{-}N_2]\}$ was performed in gas phase due to numerical instability of optimization with COMSO. Vibrational normal mode analyses were performed to confirm that the optimized structures are minima on the respective ground-state potential energy surfaces. Hessians were determined numerically for COSMO calculations and analytically [229] for gas-phase calculations. The computed vibrational frequencies were scaled by 0.98 to account for anharmonicity [230]. The ground-state energy difference between $\{[(R_2N)_3Sc]_2[\mu\text{-}\eta^1\text{:}\eta^1\text{-}N_2]\}^{2-}$ and $\{[(R_2N)_3Sc]_2[\mu\text{-}\eta^2\text{:}\eta^2\text{-}N_2]\}^{2-}$ was obtained from single-point calculations using the def2-TZVP basis set based on structures optimized using the def2-SV(P) basis set. The UV-visible spectrum of $\{[(R_2N)_3Sc]_2[\mu\text{-}\eta^1\text{:}\eta^1\text{-}N_2]\}^{2-}$ was simulated using TDDFT and nonorthonormal Krylov subspace method [199] with 25 and 40 exited states in A_1 and E

irreducible representations, respectively. The calculation was performed using PBE0 functional [155, 231] and def2-SVPD basis set [232] based on the structure optimized using the def2-TZVP basis set. The simulated spectrum was obtained by superimposing Gaussian functions with an RMS width of 0.25 eV (Figure 3.8). All calculations were performed using TURBOMOLE 7.0 and 7.1 [25].

3.3.3 Results and Discussions

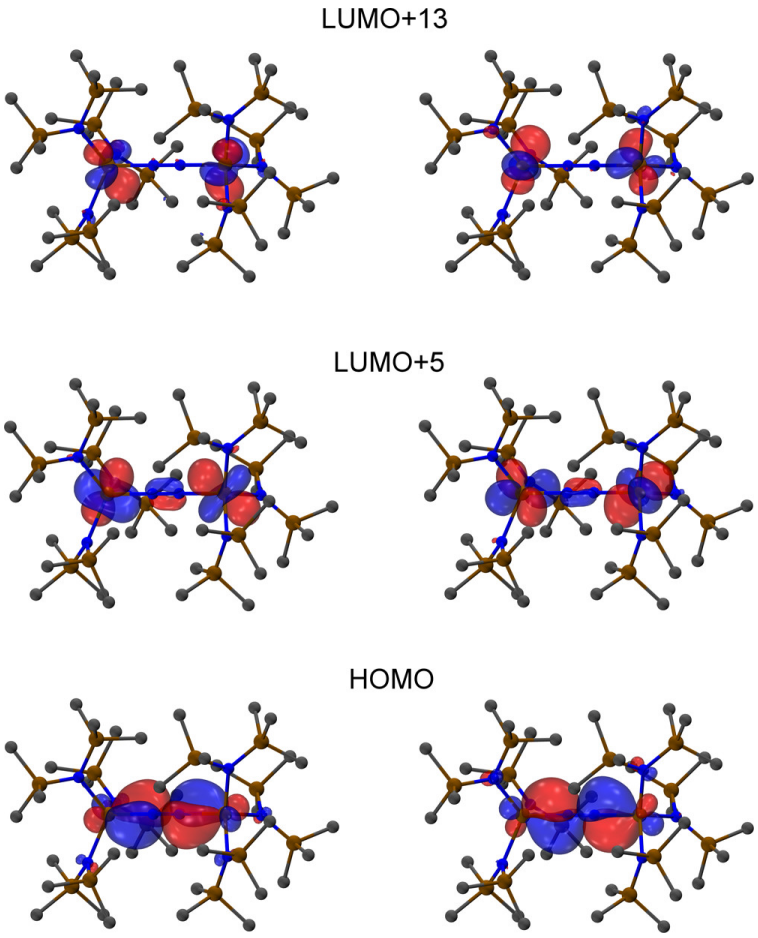

Figure 3.7: HOMO, LUMO+5, and LUMO+13 of $\{[(R_2N)_3Sc]_2[\mu\text{-}\eta^1\text{:}\eta^1\text{-}N_2]\}^{2-}$ with a contour value of 0.035. Hydrogen atoms are omitted for clarity. Reprinted with permission from Reference [226], Copyright 2017 American Chemical Society.

DFT calculations on the dianion $\{[(R_2N)_3Sc]_2[\mu\text{-}\eta^1\text{:}\eta^1\text{-}N_2]\}^{2-}$ reproduced the experimentally observed structure of $\{K(crypt)\}_2\{[(R_2N)_3Sc]_2[\mu\text{-}\eta^1\text{:}\eta^1\text{-}N_2]\}$ with an N–N distance of 1.202

Table 3.3: (Average) bond distances (in Å) and N–N stretching frequencies (in cm^{-1}) of bridging dinitrogen complexes of Sc.

Compound	Method	N–N	Sc–N(N_2)	Sc–N(NR_2)	freq.
$\{[(R_2N)_3Sc]_2[\mu\text{-}\eta^1\text{:}\eta^1\text{-}N_2]\}^{2-}$	Expt.	1.221	2.031	2.150	1644
	TPSS/def2-SV(P)	1.207	2.044	2.160	1724
	TPSS/def2-TZVP	1.202	2.045	2.160	1676
$\{[(R_2N)_3Sc]_2[\mu\text{-}\eta^2\text{:}\eta^2\text{-}N_2]\}^{2-}$	TPSS/def2-SV(P)	1.240	2.229	2.195	1542
$\{[(R_2N)_2Sc(THF)]_2[\mu\text{-}\eta^2\text{:}\eta^2\text{-}N_2]\}$	TPSS/def2-SV(P)	1.245	2.182	2.079	1520

Å (Table 3.3). The calculations indicate a triplet ($^3A_2$) ground state in D_3 symmetry with two unpaired electrons in the HOMOs consisting of two degenerate orbitals that are mainly N_2 π^* in character, but have Sc–N_2–Sc π bonding components, Figure 3.7.

The UV-visible spectrum of $\{K(crypt)\}_2\{[(R_2N)_3Sc]_2[\mu\text{-}\eta^1\text{:}\eta^1\text{-}N_2]\}$ exhibits an intense absorption at 406 nm (ε = 14000 $M^{-1}cm^{-1}$), Figure 3.8. TDDFT calculations attribute this absorption to electronic excitations at 364 and 408 nm, Figure 3.8. Both of these contain large contributions due to transitions from the degenerate Sc–N_2–Sc π bonding orbitals (96e α, HOMO) to the Sc–N_2–Sc π antibonding orbitals (99e α, LUMO+5) and two degenerate orbitals that are of Sc d character (104e α, LUMO+13).

Brief exposure of $\{K(crypt)\}_2\{[(R_2N)_3Sc]_2[\mu\text{-}\eta^1\text{:}\eta^1\text{-}N_2]\}$ to UV light (365 nm), even at −78 °C, results in the loss of N_2 to form the previously reported dark maroon $3d^1$ Sc^{2+} complex, $[K(crypt)][Sc(NR_2)_3]$ [195]. his is not commonly observed in rare-earth metal dinitrogen chemistry: with the exception of Sm^{3+} dinitrogen complexes [189, 190, 202–211], once an $(N{=}N)^{2-}$ complex of a Ln^{3+} ion is formed, it does not revert to Ln^{2+} and N_2. This photoconversion is consistent with the TDDFT calculations, which show that the transitions populate Sc–N_2–Sc antibonding orbitals and Sc 3d orbitals. The fact that $\{K(crypt)\}_2[(R_2N)_3Sc]_2[\mu\text{-}\eta^1\text{:}\eta^1\text{-}N_2]\}$ can easily revert to $[K(crypt)][Sc(NR_2)_3]$ under light explains why dinitrogen reduction reactivity was not initially observed during the reduction of $Sc(NR_2)_3$ [195]. In contrast, $[(C_5Me_4H)_2Sc]_2[\mu\text{-}\eta^2\text{:}\eta^2\text{-}N_2]$ [178], synthesized by the reduction of $(C_5Me_4H)_2Sc(\mu\text{-}\eta^1\text{-}$

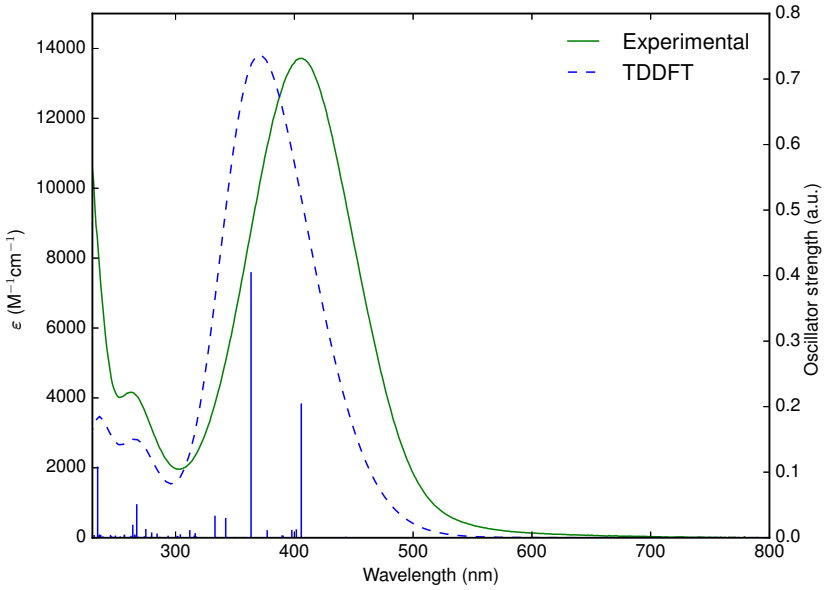

Figure 3.8: Experimental (green solid-line) and TDDFT calculated (blue dashed-line) UV-visible spectra of $\{K(crypt)\}_2\{[(R_2N)_3Sc]_2[\mu\text{-}\eta^1\text{:}\eta^1\text{-}N_2]\}$ collected from a ca. 1 mM THF solution. Reprinted with permission from Reference [226], Copyright 2017 American Chemical Society.

Ph)BPh_3 under dinitrogen, has only weak absorptions in its UV-visible spectrum at 592 nm (ε = 60 $M^{-1}cm^{-1}$) and 447 nm (ε = 200 $M^{-1}cm^{-1}$) and does not form a Sc^{2+} complex photochemically. Complexes $[(Ar[^tBu]N)_3Mo]_2(\mu\text{-}\eta^1\text{:}\eta^1\text{-}N_2)$ [233] and $(L^{Me}Fe)_2(\mu\text{-}\eta^1\text{:}\eta^1\text{-}N_2)$ (L^{Me} = β-diketiminate) [234] also extrude dinitrogen upon photolysis [233, 234].

Table 3.4: Electronic excitations of $\{[(R_2N)_3Sc]_2[\mu\text{-}\eta^1\text{:}\eta^1\text{-}N_2]\}^{2-}$ with significant intensity. Oscillator strengths are in length representation. All listed excitations are from the 96e α HOMO. Transitions with contributions larger than 10% are listed.

State	Wavelength (nm)	Oscillator Strength (10^{-2} a.u.)	Dominant contributions		Assignment
			unoccupied	contribution	
1^3A_1	406	0.203	99e α	53.4%	Sc–N_2–Sc $\pi\rightarrow$Sc–N_2–Sc π^*
			104e α	11.1%	Sc–N_2–Sc $\pi\rightarrow$Sc d
4^3A_1	364	0.404	99e α	35.7%	Sc–N_2–Sc $\pi\rightarrow$Sc–N_2–Sc π^*
			104e α	28.0%	Sc–N_2–Sc $\pi\rightarrow$Sc d
			103e α	19.9%	Sc–N_2–Sc $\pi\rightarrow$Sc d

The light sensitivity of $\{K(crypt)\}_2[(R_2N)_3Sc]_2[\mu\text{-}\eta^1\text{:}\eta^1\text{-}N_2]\}$ was also observed during Raman

measurements. A Raman spectrum of $\{K(crypt)\}_2[(R_2N)_3Sc]_2[\mu\text{-}\eta^1\text{:}\eta^1\text{-}N_2]\}$ could not be obtained due to sample decomposition using the 532 nm laser previously used to analyze over 20 other rare-earth metal dinitrogen complexes [220]. However, the use of a lower-energy 785 nm laser provided a Raman scattering signal at 1644 cm^{-1} for $\{K(crypt)\}_2[(R_2N)_3Sc]_2[\mu\text{-}\eta^1\text{:}\eta^1\text{-}N_2]\}$. The DFT calculated value of 1676 cm^{-1} (Table 3.3) matches the experimental value at the level previously observed for rare-earth metal dinitrogen complexes [220]. This stretching frequency is noticeably higher than the 1413–1473 cm^{-1} range observed for the side-on dinitrogen bridged complexes of rare-earth metals, which indicates a lower degree of dinitrogen activation. DFT calculations were also carried out on the hypothetical neutral side-on bound dinitrogen complex with two amide ligands per metal, i.e., $\{[(R_2N)_2Sc(THF)]_2[\mu\text{-}\eta^2\text{:}\eta^2\text{-}N_2]\}$ and $\{[(R_2N)_3Sc]_2[\mu\text{-}\eta^2\text{:}\eta^2\text{-}N_2]\}^{2-}$, the dianionic side-on analog of $\{[(R_2N)_3Sc]_2[\mu\text{-}\eta^1\text{:}\eta^1\text{-}N_2]\}^{2-}$. The calculations suggest that the N–N stretching frequencies should be below 1550 cm^{-1} for these side-on complexes (Table 3.3).

These calculations also reveal that the hypothetical $\{[(R_2N)_3Sc]_2[\mu\text{-}\eta^2\text{:}\eta^2\text{-}N_2]\}^{2-}$ is 12 kcal/mol higher in energy than $\{[(R_2N)_3Sc]_2[\mu\text{-}\eta^1\text{:}\eta^1\text{-}N_2]\}^{2-}$ The preference for the end-on binding motif is likely caused by the steric constraint of the three ancillary ligands. The influence of ancillary ligand size on the binding mode of $(N{=}N)^{2-}$ has previously been observed with cyclopentadienyl Ti and Zr complexes. The pair $[(C_5Me_4H)_2Ti]_2[\mu\text{-}\eta^1\text{:}\eta^1\text{-}N_2]$ [235] and $[(C_5Me_3H_2)_2Ti]_2[\mu\text{-}\eta^2\text{:}\eta^2\text{-}N_2]$ [236, 237] as well as $[(C_5Me_5)_2Zr(N_2)]_2[\mu\text{-}\eta^1\text{:}\eta^1\text{-}N_2]$ [238] and $[(C_5Me_4H)_2Zr]_2[\mu\text{-}\eta^2\text{:}\eta^2\text{-}N_2]$ [239] illustrate this point. The small size and high Lewis acidity of Sc^{3+} could be responsible for the retainment of all three ancillary anionic amide ligands per metal. This ligand environment is sterically more crowded than the bis(amide)(THF) coordination in $\{[(R_2N)_2Ln(THF)]_2[\mu\text{-}\eta^2\text{:}\eta^2\text{-}N_2]\}$ and an end-on structure results in $\{K(crypt)\}_2[(R_2N)_3Sc]_2[\mu\text{-}\eta^1\text{:}\eta^1\text{-}N_2]\}$.

3.4 $\{Pu[C_5H_3(SiMe_3)_2]_3\}^-$: The First Isolable Pu^{2+} Complex

3.4.1 Introduction

Since Seaborg, McMillan, Kennedy, and Wahl's discovery of plutonium in 1940 [240, 241] Pu has emerged as one of the most high-profile elements in the periodic table. The recognition that Pu chemistry is pivotal in a wide range of long-term global challenges is reflected in a recent renaissance in actinide chemistry. Motivated by this realization, international efforts are underway to provide fundamental understanding that underlies actinide processing and applications [242–246]. Unfortunately, advances in uncovering new properties for Pu have been slow compared with the $4f$ elements, Th, and U. The slower progress stems from the high specific radioactivity and limited accessibility of Pu. Consequently, chemical research with Pu needs to be conducted in specialized radiological facilities. Usually, synthetic chemistry with Pu is performed on a small scale (milligrams) for reasons of both safety and security [242, 247]. These constraints render synthetic work and characterization methods technically challenging, especially when targeting molecules that are reactive toward air/moisture. In fact, it is rare to find laboratories equipped with modern structural tools for fundamental air- and moisture-sensitive Pu chemistry. To date there are less than 25 structural records in the Cambridge Structural Database (CSD) that contain anhydrous molecular Pu compounds prepared under inert atmospheres [248]. No records with full structural details contain Pu–C bonds.

Recent advances in lanthanide chemistry resulted in a new series of complexes that contained all of the $4f$ elements (excluding Pm) in the formal +2 oxidation state [162, 167]. Among this series, eight elements (La, Ce, Pr, Gd, Tb, Ho, Er, and Lu) were reported to have unusual $4f^n5d^1$ ground-state electron configurations, as opposed to the typical

$4f^{n+1}5d^0$ configuration. It was proposed that in these unusual compounds, the C_3-symmetric tris(cyclopentadienyl) environment stabilized population of the $5d$ orbitals (over the $4f$ orbitals). On the basis of these results, efforts to use the same ligand system to stabilize actinide(II) compounds through population of analogous $6d$ orbitals was investigated. Indeed, the first U^{2+} and Th^{2+} complexes were prepared [169, 170] and shown to exhibit the rare $5f^36d^1$ (U^{2+}) and $5f^06d^2$ (Th^{2+}) electron configurations. Inspired by these foundational compounds, we set out to explore (1) whether a formal +2 oxidation state is stable and isolable for transuranic elements (specifically for Pu) and (2) whether the stable $5f^n6d^1$ (as opposed to $5f^{n+1}6d^0$) configurations would continue across the actinide series.

The new Ln^{2+}, U^{2+}, and Th^{2+} compounds were discovered by reduction of organometallic complexes containing metals in the +3 oxidation state. Success in preparing these compounds appeared to rely on encapsulation of the potassium cation with 2.2.2-cryptand (crypt) and f-element ligation by three sterically bulky cyclopentadienyl rings, namely the trimethylsilyl-substituted rings $C_5H_4SiMe_3$ (Cp') or $C_5H_3(SiMe_3)_2$-1,3 (Cp"). The successful identification of U^{2+} and Th^{2+} sparked a renewed interest in organometallic transuranic chemistry. Plutonium in the formal +2 oxidation state was reported in PuH_2 and PuE (E = S, Se, Te), and Pu^{2+} compounds were identified in molten salts or the gas phase [249–251]. However, the identities of these Pu^{2+} compounds were not substantiated through single-crystal X-ray diffraction. This section presents the computational characterization of the first isolable and crystallographically identified Pu^{2+} complex, namely [K(crypt)][PuCp"$_3$]. The synthesis, isolation, and experimental characterization of this Pu^{2+} complex are detailed in Reference [172].

3.4.2 Computational Details

Structures of $[AnCp"_3]^-$ and $AnCp"_3$ (An = Th–Cm) were optimized in C_1 symmetry using DFT. The non-empirical meta-GGA functional, TPSS [63], were used in all geometry optimizations, while its global hybrid version, TPSSh [122], were used for $[PuCp"_3]^-$ to further validate the results. The performance of these functionals for low-valent lanthanide and actinide compounds is well documented [163–165, 170]. Basis sets of valence triple-zeta plus polarization quality (def2-TZVP) were used for light atoms [61], and Stuttgart-Cologne scalar-relativistic effective core potentials (ECPs) [252] and the corresponding valence basis set [253] with 3 additional g polarization functions were used for actinide atoms. Fine density grids of at least m4 quality were employed for numerical integration [64]. Solvent effects were included by the COSMO continuum solvation model [196] using the dielectric constant of THF, 7.52 [197]. The maximum norm of the Cartesian coordinate gradient was converged to $\leq 10^{-4}$ a.u. in all geometry optimizations. Numerical vibrational normal mode analyses were performed for optimized structures except for the TPSSh optimizations and the TPSS optimization for the $5f^5 6d^1$ $[PuCp"_3]^-$. Energy minima were confirmed for the analyzed structures except for $AnCp"_3$ (An = Pa, Np, Am) and $[AmCp"_3]^-$. For the neutral complexes $AnCp"_3$ (An = Pa, Np, Am), we performed a new two-step optimization: we first optimized the structures in gas phase and confirmed that they were local minima on the gas-phase potential energy surface using analytic second-order derivatives; subsequent optimizations were performed with COSMO and without additional normal mode analyses. For $[AmCp"_3]^-$, numerical normal mode analysis showed a small imaginary frequency of $16i$ cm^{-1}, which can be ascribed to numerical inaccuracy of the COSMO implementation and the structure can still be considered as being at an approximate energy minimum.

High-spin states were confirmed to be the ground states of $[AnCp"_3]^-$ and $AnCp"_3$ (An = Pa – Cm) [170, 254], while the ground state of $[ThCp"_3]^-$ was confirmed to be a singlet spin state [169]. The relative stability of the electronic states of $5f^6 6d^0$ versus $5f^5 6d^1$ Pu^{2+}

configurations in $[PuCp"_3]^-$ was assessed by ΔSCF calculations at optimized geometries using TPSS and TPSSh. The calculations showed that the $5f^6 6d^0$ state is favorable by 6.0 kcal/mol using TPSS and 4.4 kcal/mol using TPSSh.

The UV-visible spectra of $[PuCp"_3]^-$, $PuCp"_3$, and $[HPuCp"_3]^-$ were simulated using TDDFT [53]. Property-optimized basis sets, def2-SVPD [232] were used for light atoms, and the Stuttgart-Cologne ECPs and corresponding valence basis sets were used for Pu. Gauge-invariant implementations of TPSS and TPSSh were employed. COSMO were used to model the solvent effects in THF solution. All calculations were performed using TURBOMOLE 6.6, 7.0, and 7.1 [25].

3.4.3 Results and Discussions

Geometry optimizations using DFT predicted trigonal-planar structures for both $PuCp"_3$ and the $[PuCp"_3]^-$ anion. The computational results are in good agreement with the crystallographic data, e.g., the calculated metal-(ring centroid) average distance for $[PuCp"_3]^-$ is within 0.01 Å of the X-ray result. The calculated 0.05 Å difference in metal-(ring centroid) distance between $PuCp"_3$ and $[K(crypt)][PuCp"_3]$ is larger than that observed between $ThCp"_3$/UCp'_3 and $[ThCp"_3]^-$/$[UCp'_3]^-$ (∼0.02 Å) but less than the anticipated ∼0.1 Å change in ionic radius from Pu^{3+} to Pu^{2+}. Mulliken population analysis suggests that the HOMO of $[PuCp"_3]^-$ (Figure 3.9a) is predominantly a Pu–Cp" nonbonding f_{z^3} orbital. However, the HOMO also possesses appreciable (7%) d_{z^2} character. The mixing of $5f$ and $6d$

Table 3.5: Computed metal-(ring centroid) distances (in Å) of $[An^{II}Cp"_3]^-$ and $An^{III}Cp"_3$ (An = Th–Cm) using TPSS functional and def2-TZVP basis sets.

	Th	Pa	U	Np	Pu	Am	Cm
$[An^{II}Cp"_3]^-$	2.529	2.481	2.519	2.505	2.531	2.615	2.541
$An^{III}Cp"_3$	2.540	2.475	2.501	2.496	2.480	2.493	2.507
Difference	−0.011	0.009	0.019	0.009	0.051	0.122	0.034

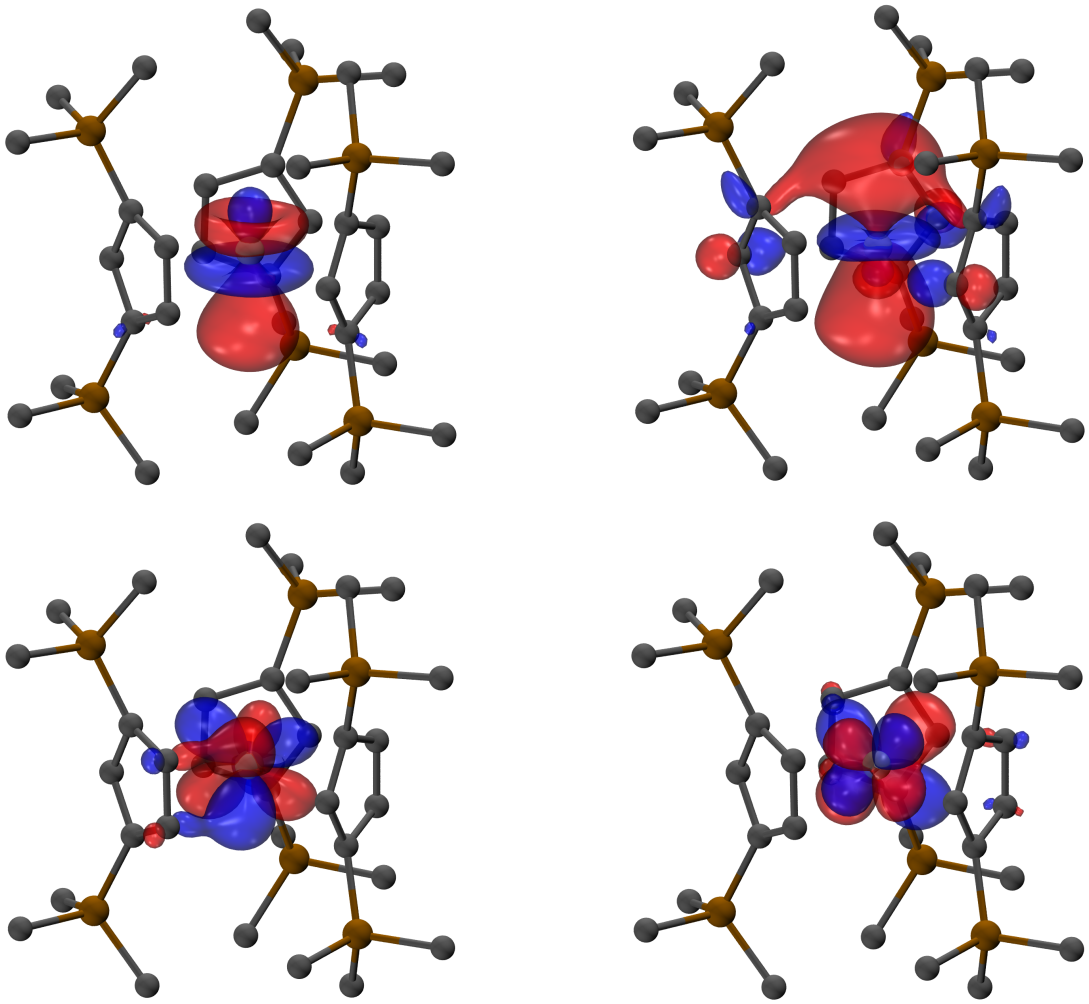

Figure 3.9: (a) HOMO, (b) LUMO, (c) HOMO-3, and (d) HOMO-4 of $[PuCp"_3]^-$ with a contour value of 0.035. Hydrogen atoms are omitted for clarity. Reprinted with permission from Reference [172], Copyright 2017 American Chemical Society.

orbitals is consistent with the slight $C_{3h} \rightarrow C_3$ pseudo-Jahn–Teller distortion of the complex due to the near degeneracy of the Pu^{2+} $5f^5 6d^1$ and $5f^6 6d^0$ configurations. Thus, the calculations suggest that $[PuCp"_3]^-$ is a borderline case between the traditional $4f^{n+1}5d^0$ Ln^{2+} compounds and the new Ln^{2+}, U^{2+}, and Th^{2+} compounds which manifest d occupation. Our calculations on $[AnCp"_3]^-$ (An = Th–Cm; Figure 3.10 and Table 3.5) and earlier results on $[AnCp'_3]^-$ (An = Th–Am) [254] also suggest that the $5f^n 6d^1$ to $5f^{n+1}6d^0$ crossover occurs near Pu.

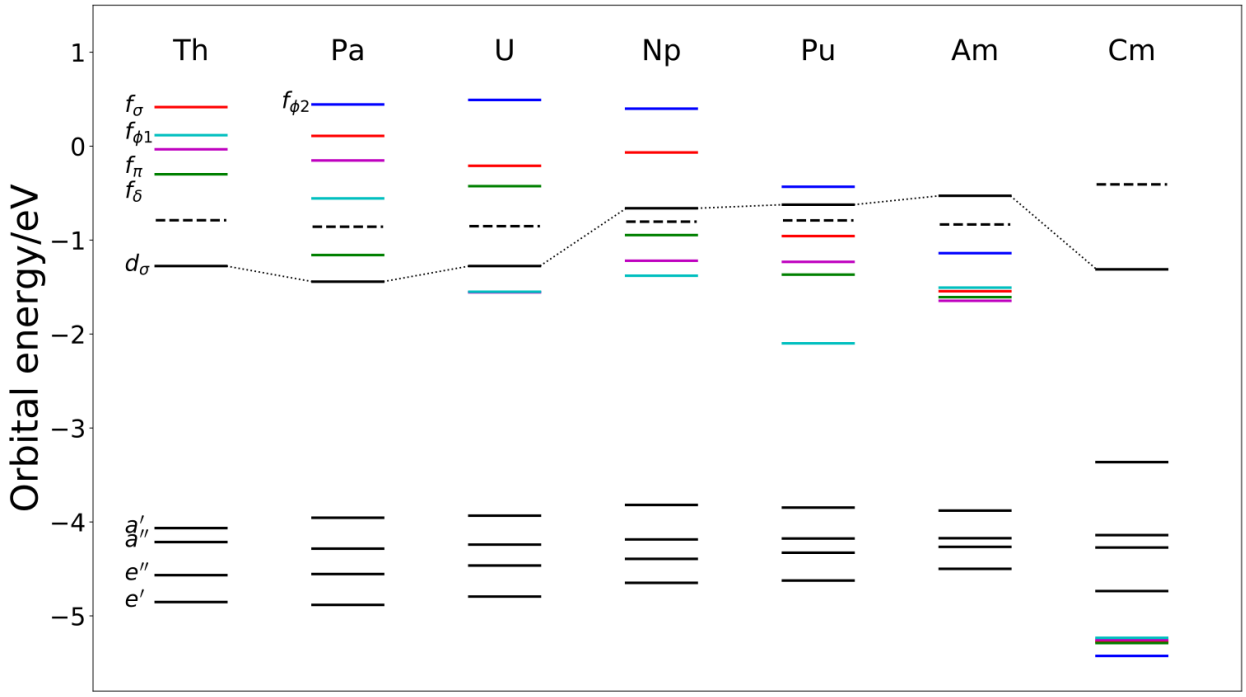

Figure 3.10: Frontier orbital level diagram of $[AnCp"_3]^-$ (An = Th–Cm) using α orbitals energies of semilocal DFT (TPSS) calculations. Doubly occupied ligand π_2-based orbitals are labeled using pseudo-C_{3h} symmetry. The e', e", f_π, f_δ orbitals are doubly degenerate. The Fermi levels (average of HOMO and LUMO energies) are denoted by dashed lines. Reprinted with permission from Reference [172], Copyright 2017 American Chemical Society.

The UV/vis/NIR absorption spectrum of $PuCp"_3$ in hexane contains a broad and intense band around 17153 cm^{-1} (~600 $M^{-1}cm^{-1}$), which is not typical in the visible spectra of complexes containing Pu^{3+} ions [241, 242, 255]. Our TDDFT calculations suggest that this band predominantly originates from a $5f \rightarrow 6d$ transition. The band is observable in the visible region because of the strong stabilization of the $6d_{z^2}$ orbital in the trigonal-planar ligand field. Numerous weak absorptions between 20000 and 7700 cm^{-1} are assigned to Laporte-forbidden $5f \rightarrow 5f$ transitions characteristic of Pu^{3+} [241]. Reduction of $PuCp"_3$ to $[PuCp"_3]^-$ imparts substantial changes in the UV/vis/NIR spectrum. The $5f \rightarrow 5f$ transitions characteristic of $PuCp"_3$ are detected as an impurity only in the solution-phase UV/vis/NIR spectrum of $[K(crypt)][PuCp"_3]$ and were not detected in the solid-state spectrum. Both the solution (Figure 3.11) and solid-state spectra of $[K(crypt)][PuCp"_3]$ are dominated by very broad

bands with maxima at ∼21300 cm^{-1} and extending past 12500 cm^{-1}. With an approximate molar absorptivity of 2700 $M^{-1}cm^{-1}$, this band is considerably more intense than $5f \rightarrow 5f$ transitions typically observed in this region.

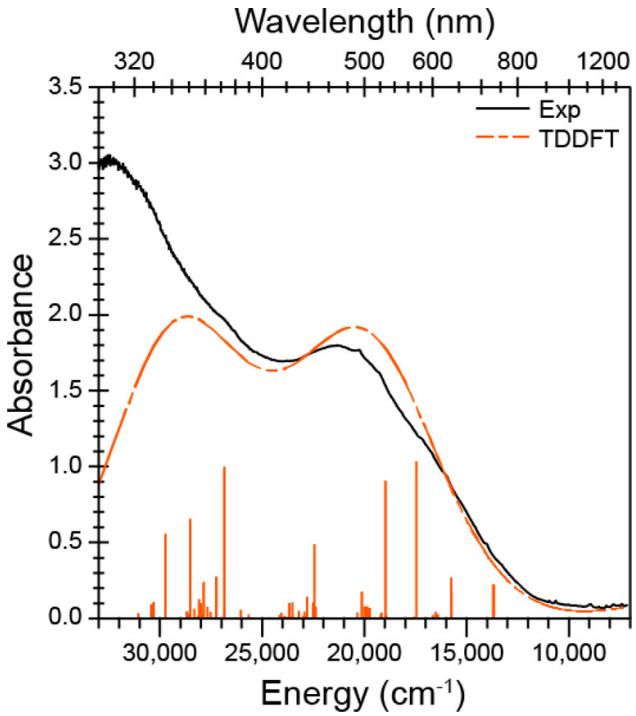

Figure 3.11: Solution-phase (in THF) UV/vis/NIR experimental data for $[PuCp"_3]^-$ (black trace). The orange bars represent the energies and oscillator strengths in the TDDFT-calculated UV/vis/NIR spectrum (orange dashed trace). Reprinted with permission from Reference [172], Copyright 2017 American Chemical Society.

TDDFT calculations on $[PuCp"_3]^-$ attribute these strong absorptions to metal-to-ligand charge transfer (MLCT) excitations originating from Pu $5f$ orbitals (See the Supporting Information in Reference [172]). The unusually high intensity of these transitions compared with that in $PuCp"_3$ may be rationalized by an increase in $5f$ orbital energy and radial extent, likely caused by increased electron repulsion in the $5f^6$ configuration in $[PuCp"_3]^-$ compared with the $5f^5$ Pu^{3+} configuration. These factors red-shift the MLCT transitions into the visible region and lead to larger transition dipole moments involving coupling between $5f$ and ligand orbitals, ultimately providing a mechanism to increase the absorption intensities. In contrast, the $4f$ orbitals in traditional Ln^{2+} compounds with $4f^{n+1}5d^0$ configurations, such

as $[SmCp'_3]^-$ are considerably lower in energy and more contracted than the $5f$ orbitals in [K(crypt)][PuCp"$_3$]. Hence, these compounds do not exhibit strong MLCT transitions in the visible spectrum [162, 167]. The calculations also suggest that the high energy of the $5f$ orbitals and stabilized $6d_{z^2}$ orbital results in low-energy $5f \rightarrow 6d$ transitions in $[PuCp"_3]^-$ The calculated energy of this transition is near 2600 cm^{-1}, outside the range of the conventional UV/vis/NIR spectrum provided in Figure 3.11. While some of the intensity of the visible transitions in [K(crypt)][PuCp"$_3$] may be attributable to configuration mixing in the ground state and/or thermal population of the low-lying $5f^5 6d^1$ excited state, more sophisticated measurements and computations are needed for verification.

3.5 Discussions

Due to their large sizes, small HOMO-LUMO gaps, and multiconfigurational nature, rare-earth and actinide complexes are challenging for present-day electronic structure methods. Bulky ligands are commonly used to impose steric constraints or to "trap" electrons at the metal center, stabilizing charged species [256]. Computationally, the presence of bulky ligands requires proper treatment of not only covalent but also noncovalent interactions such as dispersion. The near-degeneracy of the $4f$ manifold and low-lying $5d$ orbitals in specific ligand fields leads to small HOMO-LUMO gaps and multiconfigurational character of lanthanide complexes. A similar situation is encountered in actinides, where near degeneracy amongst $5f$ and $6d$ subshells is observed [245, 257–261]. Single-reference many-body perturbation theory such as MP2 is incapable of even qualitatively describing these systems, while multireference calculations are typically attempted for model systems only (see, e.g., Reference [168]). Moreover, the demand for geometry optimizations and vibrational normal mode analyses renders routine multireference calculations impractical. Consequently, semilocal and hybrid DFT is still the method of choice for most rare-earth and actinide

applications [262]. This is supported by the success of DFT in predicting and characterizing unconventional rare-earth and actinide complexes presented herein. However, density functional approximations sometimes lead to different qualitative results (see, e.g., Reference [168]), which severely limits the predictive power of DFT calculations.

Exploratory RPA calculations on lanthanide and actinide complexes [263, 264] suggested that RPA and its perturbative corrections may be used to improve or validate semilocal DFT results. Nevertheless, one may wonder whether the static correlation in rare-earth and actinide complexes are too strong, as in the case of metal dimers presented in Section 2.5.5. The $[PuCp"_3]^-$ complex is a good test case for the RPA methods because of its multiconfigurational character indicated by the existence of low-lying excited states. Using the MO based RI implementation discussed in Chapter 2, the AXK and SOX beyond-RPA correlation energies for $[PuCp"_3]^-$ were computed with def2-TZVP basis and 50 frequency points. Following Section 2.6, we obtained an $\bar{\alpha}$ value of 0.41, indicating moderately strong correlation, which is within the applicable range of RPA and AXK. This result suggests that RPA with AXK correction could be a useful computational method for rare-earth and actinide chemistry despite its failure on metal dimers. More thorough benchmark calculations still need to be carried out before a conclusive statement is made, and the success of routine applications also relies on the development of basis sets, analytic gradients [265], and approximations for relativistic effects [266].

3.6 Conclusions

The first examples of isolable Sc^{2+} and Pu^{2+} complexes have been identified. The experimental characterization of these unconventional complexes were aided by DFT and TDDFT calculations. These calculations predicted observables, such as structural parameters, vibrational frequencies, and UV-visible spectra, which were directly compared with experimental

measurements. They also provided analytical tools such as molecular orbitals and transition density matrices, which shed light on the electronic structures, reactivities, and spectroscopic properties of these compounds.

The new $[Sc(NR_2)_3]^-$ and $[PuCp"_3]^-$ complexes share similarities with their yttrium and lanthanide tris(silylcyclopentadienyl) analogs, such as the trigonal planar geometry and strong absorptions in the visible spectrum. But they also show their own uniqueness, possibly due to the small size of scandium and the larger radial extent of Pu $5f$ orbitals versus Ln $4f$ orbitals. The recent discovery of $[Ln(NR_2)_3]^-$ complexes [267] provides a new series of Ln^{2+} ions that can be directly compared with the Sc^{2+} ion in $[Sc(NR_2)_3]^-$. Experimental and theoretical investigations of this series may further reveal similarities and differences between these metals.

The computational results presented in this chapter also suggest that modern semilocal and hybrid density functional approximations are semiquantitative for d- and f-block metal complexes. Preliminary calculations show that the RPA methods, particularly the AXK method, may be suitable for these systems. The balanced treatment of long-range and short-range interactions provided by the AXK method may offer improvements upon and validations of DFT calculations.

Bibliography

[1] K. Burke: Perspective on Density Functional Theory, *J. Chem. Phys.* **136**, 150901, 2012.

[2] A. J. Cohen, P. Mori-Sánchez, and W. Yang: Challenges for Density Functional Theory, *Chem. Rev.* **112**, 289–320, 2012.

[3] A. Pribram-Jones, D. A. Gross, and K. Burke: DFT: A Theory Full of Holes?, *Annu. Rev. Phys. Chem.* **66**, 283–304, 2015.

[4] O. V. Gritsenko, P. R. T. Schipper, and E. J. Baerends: Exchange and Correlation Energy in Density Functional Theory: Comparison of Accurate Density Functional Theory Quantities with Traditional Hartree–Fock Based Ones and Generalized Gradient Approximations for the Molecules Li_2, N_2, F_2, *J. Chem. Phys.* **107**, 5007–5015, 1997.

[5] M. Ernzerhof, K. Burke, and J. P. Perdew: Density Functional Theory, the Exchange Hole, and the Molecular Bond, in J. M. Seminario, editor, Recent Developments in Density Functional Theory, volume 4, chapter 6, pp. 207–238, Elsevier, Amsterdam, 1996.

[6] M. Fuchs, Y.-M. Niquet, X. Gonze, and K. Burke: Describing Static Correlation in Bond Dissociation by Kohn-Sham Density Functional Theory, *J. Chem. Phys.* **122**, 094116, 2005.

[7] S. Grimme, J. Antony, S. Ehrlich, and H. Krieg: A Consistent and Accurate Ab Initio Parametrization of Density Functional Dispersion Correction (DFT-D) for the 94 Elements H-Pu, *J. Chem. Phys.* **132**, 154104, 2010.

[8] E. Caldeweyher, C. Bannwarth, and S. Grimme: Extension of the D3 Dispersion Coefficient Model, *J. Chem. Phys.* **147**, 034112, 2017.

[9] A. Heßelmann and A. Görling: Random-Phase Approximation Correlation Methods for Molecules and Solids, *Mol. Phys.* **109**, 2473–2500, 2011.

[10] H. Eshuis, J. E. Bates, and F. Furche: Electron Correlation Methods Based on the Random Phase Approximation, *Theor. Chem. Acc.* **131**, 1084, 2012.

[11] X. Ren, P. Rinke, C. Joas, and M. Scheffler: Random-Phase Approximation and Its Applications in Computational Chemistry and Materials Science, *J. Mater. Sci.* **47**, 7447–7471, 2012.

[12] G. P. Chen, V. K. Voora, M. M. Agee, S. G. Balasubramani, and F. Furche: Random-Phase Approximation Methods, *Annu. Rev. Phys. Chem.* **68**, 421–445, 2017.

[13] D. C. Langreth and J. P. Perdew: The Exchange-Correlation Energy of a Metallic Surface, *Solid State Commun.* **17**, 1425–1429, 1975.

[14] D. Langreth and J. Perdew: Exchange-Correlation Energy of a Metallic Surface: Wave-Vector Analysis, *Phys. Rev. B* **15**, 2884–2901, 1977.

[15] M. Gell-Mann and K. A. Brueckner: Correlation energy of an electron gas at high density, *Phys. Rev.* **106**, 364–368, 1957.

[16] K. Sawada: Correlation Energy of an Electron Gas at High Density, *Phys. Rev.* **106**, 372–383, 1957.

[17] F. Furche: Molecular Tests of the Random Phase Approximation to the Exchange-Correlation Energy Functional, *Phys. Rev. B* **64**, 195120, 2001.

[18] T. M. Henderson and G. E. Scuseria: The connection between self-interaction and static correlation: a random phase approximation perspective, *Mol. Phys.* **108**, 2511–2517, 2010.

[19] J. F. Dobson, J. Wang, B. P. Dinte, K. McLennan, and H. M. Le: Soft cohesive forces, *Int. J. Quantum Chem.* **101**, 579–598, 2005.

[20] J. F. Dobson and T. Gould: Calculation of dispersion energies, *J. Phys. Condens. Matter* **24**, 073201, 2012.

[21] H. Eshuis, J. Yarkony, and F. Furche: Fast Computation of Molecular Random Phase Approximation Correlation Energies Using Resolution of the Identity and Imaginary Frequency Integration, *J. Chem. Phys.* **132**, 234114, 2010.

[22] X. Ren, P. Rinke, G. E. Scuseria, and M. Scheffler: Renormalized Second-Order Perturbation Theory for the Electron Correlation Energy: Concept, Implementation, and Benchmarks, *Phys. Rev. B* **88**, 035120, 2013.

[23] D. L. Freeman: Coupled-Cluster Expansion Applied to the Electron Gas: Inclusion of Ring and Exchange Effects, *Phys. Rev. B* **15**, 5512–5521, 1977.

[24] G. E. Scuseria, T. M. Henderson, and D. C. Sorensen: The ground state correlation energy of the random phase approximation from a ring coupled cluster doubles approach, *J. Chem. Phys.* **129**, 231101, 2008.

[25] F. Furche, R. Ahlrichs, C. Hättig, W. Klopper, M. Sierka, and F. Weigend: Turbomole, *WIREs Comput. Mol. Sci.* **4**, 91–100, 2014.

[26] C. Waitt, N. M. Ferrara, and H. Eshuis: Thermochemistry and Geometries for Transition-Metal Chemistry from the Random Phase Approximation, *J. Chem. Theory Comput.* **12**, 5350–5360, 2016.

[27] H. Eshuis and F. Furche: A Parameter-Free Density Functional That Works for Noncovalent Interactions, *J. Phys. Chem. Lett.* **2**, 983–989, 2011.

[28] J. Paier, X. Ren, P. Rinke, G. E. Scuseria, A. Grüneis, G. Kresse, and M. Scheffler: Assessment of Correlation Energies Based on the Random-Phase Approximation, *New J. Phys.* **14**, 043002, 2012.

[29] D. Bohm and D. Pines: A Collective Description of Electron Interactions. I. Magnetic Interactions, *Phys. Rev.* **82**, 625–634, 1951.

[30] D. Pines and D. Bohm: A Collective Description of Electron Interactions: II. Collective vs Individual Particle Aspects of the Interactions, *Phys. Rev.* **85**, 338–353, 1952.

[31] D. Bohm and D. Pines: A Collective Description of Electron Interactions: III. Coulomb Interactions in a Degenerate Electron Gas, *Phys. Rev.* **92**, 609–625, 1953.

[32] D. Pines: A Collective Description of Electron Interactions: IV. Electron Interaction in Metals, *Phys. Rev.* **92**, 626–636, 1953.

[33] G. E. Scuseria, T. M. Henderson, and I. W. Bulik: Particle-particle and quasiparticle random phase approximations: connections to coupled cluster theory, *J. Chem. Phys.* **139**, 104113, 2013.

[34] J. Oddershede, P. Jørgensen, and D. L. Yeager: Polarization Propagator Methods in Atomic and Molecular Calculations, *Comput. Phys. Rep.* **2**, 33–92, 1984.

[35] J. Oddershede: Propagator Methods, in K. P. Lawley, editor, Advances in Chemical Physics: Ab Initio Methods in Quantum Chemistry II, volume 69, chapter 3, pp. 201–239, John Wiley & Sons, Inc., 1987.

[36] G. Onida, L. Reining, and A. Rubio: Electronic Excitations: Density-Functional versus Many-Body Green's-Function Approaches, *Rev. Mod. Phys.* **74**, 601–659, 2002.

[37] D. J. Rowe: Equations-of-Motion Method and the Extended Shell Model, *Rev. Mod. Phys.* **40**, 153–166, 1968.

[38] K. Singwi, M. Tosi, R. Land, and A. Sjölander: Electron Correlations at Metallic Densities, *Phys. Rev.* **176**, 589–599, 1968.

[39] A. Grüneis, M. Marsman, J. Harl, L. Schimka, and G. Kresse: Making the random phase approximation to electronic correlation accurate, *J. Chem. Phys.* **131**, 154115, 2009.

[40] G. Jansen, R.-F. Liu, and J. G. Ángyán: On the Equivalence of Ring-Coupled Cluster and Adiabatic Connection Fluctuation-Dissipation Theorem Random Phase Approximation Correlation Energy Expressions, *J. Chem. Phys.* **133**, 154106, 2010.

[41] J. G. Ángyán, R.-F. Liu, J. Toulouse, and G. Jansen: Correlation Energy Expressions from the Adiabatic-Connection Fluctuation–Dissipation Theorem Approach, *J. Chem. Theory Comput.* **7**, 3116–3130, 2011.

[42] J. E. Bates and F. Furche: Communication: Random Phase Approximation Renormalized Many-Body Perturbation Theory, *J. Chem. Phys.* **139**, 171103, 2013.

[43] W. Kohn and L. J. Sham: Self-Consistent Equations Including Exchange and Correlation Effects, *Phys. Rev.* **140**, A1133–A1138, 1965.

[44] O. Gunnarsson and B. I. Lundqvist: Exchange and Correlation in Atoms, Molecules, and Solids by Spin-Density Functional Formalism, *Phys. Rev. B* **13**, 4274–4298, 1976.

[45] P. Hohenberg and W. Kohn: Inhomogeneous Electron Gas, *Phys. Rev.* **136**, B864–B871, 1964.

[46] A. Görling and M. Levy: Correlation-energy functional and its high-density limit obtained from a coupling-constant perturbation expansion, *Phys. Rev. B* **47**, 13105–13113, 1993.

[47] H. B. Callen and T. A. Welton: Irreversibility and Generalized Noise, *Phys. Rev.* **83**, 34–40, 1951.

[48] E. Runge and E. K. U. Gross: Density-Functional Theory for Time-Dependent Systems, *Phys. Rev. Lett.* **52**, 997–1000, 1984.

[49] C. A. Ullrich: Time-Dependent Density-Functional Theory: Concepts and Applications, Oxford Graduate Texts, Oxford University Press, 2012.

[50] J. Linderberg and Y. Öhrn: Propagators in Quantum Chemistry, Academic Press, London, 1973.

[51] M. E. Casida: Time-Dependent Density Functional Response Theory for Molecules, in D. P. Chong, editor, Recent Advances in Density Functional Methods (Part I), volume 1 of *Recent Advances in Computational Chemistry*, pp. 155–192, World Scientific, Singapore, 1995.

[52] R. Bauernschmitt and R. Ahlrichs: Treatment of electronic excitations within the adiabatic approximation of time dependent density functional theory, *Chem. Phys. Lett.* **256**, 454–464, 1996.

[53] F. Furche: On the density matrix based approach to time-dependent density functional response theory, *J. Chem. Phys.* **114**, 5982, 2001.

[54] A. L. Fetter and J. D. Walecka: Quantum theory of many-particle systems, International series in pure and applied physics, MacGraw-Hill, New York, 1971.

[55] M. Petersilka, U. Gossmann, and E. Gross: Excitation Energies from Time-Dependent Density-Functional Theory, *Phys. Rev. Lett.* **76**, 1212–1215, 1996.

[56] L. Reining: Linear Response and More: the Bethe-Salpeter Equation, in E. Pavarini, E. Koch, J. van den Brink, and G. Sawatzky, editors, Quantum Materials: Experiments and Theory, volume 6 of *Modeling and Simulation*, chapter 10, Forschungszentrum Jülich, 2016.

[57] D. Pines: Elementary excitations in solids, chapter Appendix C, Benjamin, New York, 1963.

[58] F. Furche: Developing the random phase approximation into a practical post-Kohn-Sham correlation model, *J. Chem. Phys.* **129**, 114105, 2008.

[59] C. M. Krauter, S. Bernadotte, C. R. Jacob, M. Pernpointner, and A. Dreuw: Identification of Plasmons in Molecules with Scaled Ab Initio Approaches, *J. Phys. Chem. C* **119**, 24564–24573, 2015.

[60] J. Wang, G. Wang, and J. Zhao: Structures and electronic properties of Cu20, Ag20, and Au20 clusters with density functional method, *Chem. Phys. Lett.* **380**, 716–720, 2003.

[61] F. Weigend and R. Ahlrichs: Balanced basis sets of split valence, triple zeta valence and quadruple zeta valence quality for H to Rn: Design and assessment of accuracy, *Phys. Chem. Chem. Phys.* **7**, 3297–3305, 2005.

[62] D. Andrae, U. Häußermann, M. Dolg, H. Stoll, and H. Preuß: Energy-adjusted ab initio pseudopotentials for the second and third row transition elements, *Theor. Chim. Acta* **77**, 123–141, 1990.

[63] J. Tao, J. Perdew, V. Staroverov, and G. Scuseria: Climbing the Density Functional Ladder: Nonempirical Meta-Generalized Gradient Approximation Designed for Molecules and Solids, *Phys. Rev. Lett.* **91**, 146401, 2003.

[64] O. Treutler and R. Ahlrichs: Efficient molecular numerical integration schemes, *J. Chem. Phys.* **102**, 346, 1995.

[65] F. Sottile, V. Olevano, and L. Reining: Parameter-free calculation of response functions in time-dependent density-functional theory, *Phys. Rev. Lett.* **91**, 056402, 2003.

[66] E. E. Salpeter and H. A. Bethe: A Relativistic Equation for Bound-State Problems, *Phys. Rev.* **84**, 1232–1242, 1951.

[67] R. P. Feynman: Space-Time Approach to Quantum Electrodynamics, *Phys. Rev.* **76**, 769–789, 1949.

[68] F. J. Dyson: The Radiation Theories of Tomonaga, Schwinger, and Feynman, *Phys. Rev.* **75**, 486–502, 1949.

[69] J. Goldstone: Derivation of the Brueckner Many-Body Theory, *Proc. Roy. Soc. A* **239**, 267–279, 1957.

[70] H. van Aggelen, Y. Yang, and W. Yang: Exchange-correlation energy from pairing matrix fluctuation and the particle-particle random phase approximation, *J. Chem. Phys.* **140**, 18A511, 2014.

[71] J. Paier, B. G. Janesko, T. M. Henderson, G. E. Scuseria, A. Grüneis, and G. Kresse: Hybrid Functionals Including Random Phase Approximation Correlation and Second-Order Screened Exchange, *J. Chem. Phys.* **132**, 094103, 2010.

[72] M. A. Woodbury: Inverting Modified Matrices, Technical Report 42, Statistical Research Group, Princeton University, Princeton, 1950.

[73] W. W. Hager: Updating the Inverse of a Matrix, *SIAM Rev.* **31**, 221–239, 1989.

[74] J. P. Boyd: Exponentially Convergent Fourier-Chebshev Quadrature Schemes on Bounded and Infinite Intervals, *J. Sci. Comput.* **2**, 99–109, 1987.

[75] L. N. Trefethen and J. A. C. Weideman: The Exponentially Convergent Trapezoidal Rule, *SIAM Rev.* **56**, 385–458, 2014.

[76] J. L. Whitten: Coulombic Potential Energy Integrals and Approximations, *J. Chem. Phys.* **58**, 4496–4501, 1973.

[77] B. I. Dunlap, J. W. D. Connolly, and J. R. Sabin: On Some Approximations in Applications of Xα Theory, *J. Chem. Phys.* **71**, 3396–3402, 1979.

[78] G. P. Chen, M. M. Agee, and F. Furche: Performance and Scope of Perturbative Corrections to Random-Phase Approximation Energies, *J. Chem. Theory Comput.* **14**, 5701–5714, 2018.

[79] F. Weigend, A. Köhn, and C. Hättig: Efficient use of the correlation consistent basis sets in resolution of the identity MP2 calculations, *J. Chem. Phys.* **116**, 3175–3183, 2002.

[80] E. J. Baerends, D. E. Ellis, and P. Ros: Self-Consistent Molecular Hartree-Fock-Slater Calculations I. The Computational Procedure, *Chem. Phys.* **2**, 41–51, 1973.

[81] O. Vahtras, J. Almlöf, and M. W. Feyereisen: Integral Approximations for LCAO-SCF Calculations, *Chem. Phys. Lett.* **213**, 514–518, 1993.

[82] Y. Jung, A. Sodt, P. M. W. Gill, and M. Head-Gordon: Auxiliary Basis Expansions for Large-Scale Electronic Structure Calculations, *Proc. Natl. Acad. Sci.* **102**, 6692–6697, 2005.

[83] S. Reine, E. Tellgren, A. Krapp, T. Kjaergaard, T. Helgaker, B. Jansik, S. Host, and P. Salek: Variational and Robust Density Fitting of Four-Center Two-Electron Integrals in Local Metrics, *J. Chem. Phys.* **129**, 104101, 2008.

[84] D. P. Tew: Communication: Quasi-Robust Local Density Fitting, *J. Chem. Phys.* **148**, 011102, 2018.

[85] M. Kaltak, J. Klimeš, and G. Kresse: Low Scaling Algorithms for the Random Phase Approximation: Imaginary Time and Laplace Transformations, *J. Chem. Theory Comput.* **10**, 2498–2507, 2014.

[86] H. F. Schurkus and C. Ochsenfeld: Communication: An effective linear-scaling atomic-orbital reformulation of the random-phase approximation using a contracted double-Laplace transformation, *J. Chem. Phys.* **144**, 031101, 2016.

[87] J. E. Moussa: Cubic-Scaling Algorithm and Self-Consistent Field for the Random-Phase Approximation with Second-Order Screened Exchange, *J. Chem. Phys.* **140**, 014107, 2014.

[88] E. G. Hohenstein, R. M. Parrish, and T. J. Martinez: Tensor hypercontraction density fitting. I. Quartic scaling second- and third-order Moller-Plesset perturbation theory, *J. Chem. Phys.* **137**, 044103, 2012.

[89] M. Kallay: Linear-scaling implementation of the direct random-phase approximation, *J. Chem. Phys.* **142**, 204105, 2015.

[90] C. Møller and M. S. Plesset: Note on an Approximation Treatment for Many-Electron Systems, *Phys. Rev.* **46**, 618–622, 1934.

[91] J. Harl and G. Kresse: Accurate Bulk Properties from Approximate Many-Body Techniques, *Phys. Rev. Lett.* **103**, 056401, 2009.

[92] J. F. Dobson and J. Wang: Successful Test of a Seamless van der Waals Density Functional, *Phys. Rev. Lett.* **82**, 2123–2126, 1999.

[93] S. Lebègue, J. Harl, T. Gould, J. G. Ángyán, G. Kresse, and J. F. Dobson: Cohesive Properties and Asymptotics of the Dispersion Interaction in Graphite by the Random Phase Approximation, *Phys. Rev. Lett.* **105**, 196401, 2010.

[94] S. Kurth and J. Perdew: Density-Functional Correction of Random-Phase-Approximation Correlation with Results for Jellium Surface Energies, *Phys. Rev. B* **59**, 10461–10468, 1999.

[95] Z. Yan, J. Perdew, and S. Kurth: Density Functional for Short-Range Correlation: Accuracy of the Random-Phase Approximation for Isoelectronic Energy Changes, *Phys. Rev. B* **61**, 16430–16439, 2000.

[96] B. G. Janesko, T. M. Henderson, and G. E. Scuseria: Long-Range-Corrected Hybrids Including Random Phase Approximation Correlation, *J. Chem. Phys.* **130**, 081105, 2009.

[97] B. G. Janesko, T. M. Henderson, and G. E. Scuseria: Long-Range-Corrected Hybrid Density Functionals Including Random Phase Approximation Correlation: Application to Noncovalent Interactions, *J. Chem. Phys.* **131**, 034110, 2009.

[98] J. Toulouse, I. C. Gerber, G. Jansen, A. Savin, and J. G. Ángyán: Adiabatic-Connection Fluctuation-Dissipation Density-Functional Theory Based on Range Separation, *Phys. Rev. Lett.* **102**, 096404, 2009.

[99] J. Toulouse, W. Zhu, J. G. Ángyán, and A. Savin: Range-Separated Density-Functional Theory with the Random-Phase Approximation: Detailed Formalism and Illustrative Applications, *Phys. Rev. A* **82**, 032502, 2010.

[100] A. Ruzsinszky, J. P. Perdew, and G. I. Csonka: The RPA Atomization Energy Puzzle, *J. Chem. Theory Comput.* **6**, 127–134, 2010.

[101] A. Ruzsinszky, J. P. Perdew, and G. I. Csonka: A Simple but Fully Nonlocal Correction to the Random Phase Approximation, *J. Chem. Phys.* **134**, 114110, 2011.

[102] J. F. Dobson, J. Wang, and T. Gould: Correlation Energies of Inhomogeneous Many-Electron Systems, *Phys. Rev. B* **66**, 081108, 2002.

[103] F. Furche and T. Van Voorhis: Fluctuation-Dissipation Theorem Density-Functional Theory, *J. Chem. Phys.* **122**, 164106, 2005.

[104] J. F. Dobson and J. Wang: Energy-Optimized Local Exchange-Correlation Kernel for the Electron Gas: Application to van der Waals Forces, *Phys. Rev. B* **62**, 10038–10045, 2000.

[105] J. E. Bates, S. Laricchia, and A. Ruzsinszky: Nonlocal Energy-Optimized Kernel: Recovering Second-Order Exchange in the Homogeneous Electron Gas, *Phys. Rev. B* **93**, 045119, 2016.

[106] A. Ruzsinszky, L. A. Constantin, and J. M. Pitarke: Kernel-Corrected Random-Phase Approximation for the Uniform Electron Gas and Jellium Surface Energy, *Phys. Rev. B* **94**, 165155, 2016.

[107] T. Olsen and K. S. Thygesen: Extending the Random-Phase Approximation for Electronic Correlation Energies: The Renormalized Adiabatic Local Density Approximation, *Phys. Rev. B* **86**, 081103, 2012.

[108] T. Olsen and K. S. Thygesen: Accurate Ground-State Energies of Solids and Molecules from Time-Dependent Density-Functional Theory, *Phys. Rev. Lett.* **112**, 203001, 2014.

[109] L. A. Constantin and J. M. Pitarke: Simple Dynamic Exchange-Correlation Kernel of a Uniform Electron Gas, *Phys. Rev. B* **75**, 245127, 2007.

[110] P. E. Trevisanutto, A. Terentjevs, L. A. Constantin, V. Olevano, and F. D. Sala: Optical Spectra of Solids Obtained by Time-Dependent Density Functional Theory with the Jellium-With-Gap-Model Exchange-Correlation Kernel, *Phys. Rev. B* **87**, 205143, 2013.

[111] B. Mussard, D. Rocca, G. Jansen, and J. G. Ángyán: Dielectric Matrix Formulation of Correlation Energies in the Random Phase Approximation: Inclusion of Exchange Effects, *J. Chem. Theory Comput.* **12**, 2191–2202, 2016.

[112] A. Dixit, J. G. Ángyán, and D. Rocca: Improving the Accuracy of Ground-State Correlation Energies within a Plane-Wave Basis Set: The Electron-Hole Exchange Kernel, *J. Chem. Phys.* **145**, 104105, 2016.

[113] A. Dixit, J. Claudot, S. Lebègue, and D. Rocca: Improving the Efficiency of Beyond-RPA Methods within the Dielectric Matrix Formulation: Algorithms and Applications to the A24 and S22 Test Sets, *J. Chem. Theory Comput.* **13**, 5432–5442, 2017.

[114] M. Beuerle, D. Graf, H. F. Schurkus, and C. Ochsenfeld: Efficient Calculation of Beyond RPA Correlation Energies in the Dielectric Matrix Formalism, *J. Chem. Phys.* **148**, 204104, 2018.

[115] U. von Barth and L. Hedin: A Local Exchange-Correlation Potential for the Spin Polarized Case: I, *J. Phys. C* **5**, 1629–1642, 1972.

[116] Y. Wang and J. P. Perdew: Correlation Hole of the Spin-Polarized Electron Gas, with Exact Small-Wave-Vector and High-Density Scaling, *Phys. Rev. B* **44**, 13298–13307, 1991.

[117] P. Gori-Giorgi and J. P. Perdew: Pair Distribution Function of the Spin-Polarized Electron Gas: A First-Principles Analytic Model for All Uniform Densities, *Phys. Rev. B* **66**, 165118, 2002.

[118] C. L. Lawson, R. J. Hanson, D. R. Kincaid, and F. T. Krogh: Basic Linear Algebra Subprograms for Fortran Usage, *ACM Trans. Math. Softw.* **5**, 308–323, 1979.

[119] J. Almlöf, K. Faegri, and K. Korsell: Principles for a Direct SCF Approach to LCAO-MO Ab-Initio Calculations, *J. Comput. Chem.* **3**, 385–399, 1982.

[120] M. Häser and R. Ahlrichs: Improvements on the Direct SCF Method, *J. Comput. Chem.* **10**, 104–111, 1989.

[121] L. Dagum and R. Menon: OpenMP: An Industry Standard API for Shared-Memory Programming, *IEEE Comput. Sci. Eng.* **5**, 46–55, 1998.

[122] V. N. Staroverov, G. E. Scuseria, J. Tao, and J. P. Perdew: Comparative Assessment of a New Nonempirical Density Functional: Molecules and Hydrogen-Bonded Complexes, *J. Chem. Phys.* **119**, 12129, 2003.

[123] F. Furche and J. P. Perdew: The Performance of Semilocal and Hybrid Density Functionals in 3d Transition-Metal Chemistry, *J. Chem. Phys.* **124**, 044103, 2006.

[124] F. Weigend, F. Furche, and R. Ahlrichs: Gaussian Basis Sets of Quadruple zeta Valence Quality for Atoms H-Kr, *J. Chem. Phys.* **119**, 12753, 2003.

[125] F. Weigend, M. Häser, H. Patzelt, and R. Ahlrichs: RI-MP2: Optimized Auxiliary Basis Sets and Demonstration of Efficiency, *Chem. Phys. Lett.* **294**, 143–152, 1998.

[126] C. Hättig: Optimization of Auxiliary Basis Sets for RI-MP2 and RI-CC2 Calculations: Core–Valence and Quintuple-ζ Basis Sets for H to Ar and QZVPP Basis Sets for Li to Kr, *Phys. Chem. Chem. Phys.* **7**, 59–66, 2005.

[127] T. Helgaker, W. Klopper, H. Koch, and J. Noga: Basis-Set Convergence of Correlated Calculations on Water, *J. Chem. Phys.* **106**, 9639, 1997.

[128] A. Halkier, T. Helgaker, P. Jørgensen, W. Klopper, H. Koch, J. Olsen, and A. K. Wilson: Basis-Set Convergence in Correlated Calculations on Ne, N_2, and H_2O, *Chem. Phys. Lett.* **286**, 243–252, 1998.

[129] T. H. Dunning: Gaussian Basis Sets for Use in Correlated Molecular Calculations. I. The Atoms Boron Through Neon and Hydrogen, *J. Chem. Phys.* **90**, 1007, 1989.

[130] D. E. Woon and T. H. Dunning: Gaussian Basis Sets for Use in Correlated Molecular Calculations. III. The Atoms Aluminum Through Argon, *J. Chem. Phys.* **98**, 1358, 1993.

[131] N. B. Balabanov and K. A. Peterson: Systematically Convergent Basis Sets for Transition Metals. I. All-Electron Correlation Consistent Basis Sets for the 3d Elements Sc-Zn, *J. Chem. Phys.* **123**, 64107, 2005.

[132] F. Weigend, A. Köhn, and C. Hättig: Efficient Use of the Correlation Consistent Basis Sets in Resolution of the Identity MP2 Calculations, *J. Chem. Phys.* **116**, 3175–3183, 2002.

[133] D. H. Bross, J. G. Hill, H.-J. Werner, and K. A. Peterson: Explicitly Correlated Composite Thermochemistry of Transition Metal Species, *J. Chem. Phys.* **139**, 094302, 2013.

[134] S. Ito, S. Hiroto, S. Lee, M. Son, I. Hisaki, T. Yoshida, D. Kim, N. Kobayashi, and H. Shinokubo: Synthesis of Highly Twisted and Fully π-Conjugated Porphyrinic Oligomers, *J. Am. Chem. Soc.* **137**, 142–145, 2015.

[135] L. Goerigk, A. Hansen, C. Bauer, S. Ehrlich, A. Najibi, and S. Grimme: A Look at the Density Functional Theory Zoo with the Advanced GMTKN55 Database for General Main Group Thermochemistry, Kinetics and Noncovalent Interactions, *Phys. Chem. Chem. Phys.* **19**, 32184–32215, 2017.

[136] GMTKN55 database, `http://www.thch.uni-bonn.de/GMTKN55`, (accessed Sep 2, 2018).

[137] R. Latała: Some Estimates of Norms of Random Matrices, *Proc. Amer. Math. Soc.* **133**, 1273–1282, 2005.

[138] E. R. Johnson, P. Mori-Sánchez, A. J. Cohen, and W. Yang: Delocalization Errors in Density Functionals and Implications for Main-Group Thermochemistry, *J. Chem. Phys.* **129**, 204112, 2008.

[139] L. Goerigk and S. Grimme: A General Database for Main Group Thermochemistry, Kinetics, and Noncovalent Interactions – Assessment of Common and Reparameterized (meta-)GGA Density Functionals, *J. Chem. Theory Comput.* **6**, 107–126, 2010.

[140] H. Nakano, K. Nakayama, K. Hirao, and M. Dupuis: Transition State Barrier Height for the Reaction $H_2CO \rightarrow H_2 + CO$ Studied by Multireference Møller–Plesset Perturbation Theory, *J. Chem. Phys.* **106**, 4912–4917, 1997.

[141] Y. Zhang and W. Yang: A Challenge for Density Functionals: Self-Interaction Error Increases for Systems with a Noninteger Number of Electrons, *J. Chem. Phys.* **109**, 2604–2608, 1998.

[142] Y. Zhao, N. Gonzalez-Garcia, and D. G. Truhlar: Benchmark Database of Barrier Heights for Heavy Atom Transfer, Nucleophilic Substitution, Association, and Unimolecular Reactions and Its Use to Test Theoretical Methods, *J. Phys. Chem. A* **109**, 2012–2018, 2005.

[143] J. Zheng, Y. Zhao, and D. G. Truhlar: The DBH24/08 Database and Its Use to Assess Electronic Structure Model Chemistries for Chemical Reaction Barrier Heights, *J. Chem. Theory Comput.* **5**, 808–821, 2009.

[144] A. Ruzsinszky, I. Y. Zhang, and M. Scheffler: Insight into Organic Reactions from the Direct Random Phase Approximation and Its Corrections, *J. Chem. Phys.* **143**, 144115, 2015.

[145] M. K. Hartley, S. Vine, E. Walsh, S. Avrantinis, G. W. Daub, and R. J. Cave: Comparison of Relative Activation Energies Obtained by Density Functional Theory and the Random Phase Approximation for Several Claisen Rearrangements, *J. Phys. Chem. B* **120**, 1486–1496, 2016.

[146] D. J. Tao, M. Muuronen, Y. Slutskyy, A. Le, F. Furche, and L. E. Overman: Diastereoselective Coupling of Chiral Acetonide Trisubstituted Radicals with Alkenes, *Chem. Eur. J.* **22**, 8786–8790, 2016.

[147] H. Eshuis and F. Furche: Basis Set Convergence of Molecular Correlation Energy Differences within the Random Phase Approximation, *J. Chem. Phys.* **136**, 084105, 2012.

[148] B. Braïda, P. C. Hiberty, and A. Savin: A Systematic Failing of Current Density Functionals: Overestimation of Two-Center Three-Electron Bonding Energies, *J. Phys. Chem. A* **102**, 7872–7877, 1998.

[149] A. J. Cohen, P. Mori-Sánchez, and W. Yang: Insights into Current Limitations of Density Functional Theory, *Science* **321**, 792–794, 2008.

[150] P. Mori-Sánchez, A. J. Cohen, and W. Yang: Many-Electron Self-Interaction Error in Approximate Density Functionals, *J. Chem. Phys.* **125**, 201102, 2006.

[151] A. Ruzsinszky, J. P. Perdew, G. I. Csonka, O. A. Vydrov, and G. E. Scuseria: Density Functionals That Are One- and Two- Are Not Always Many-Electron Self-Interaction-Free, as Shown for H_2^+, He_2^+, LiH^+, and Ne_2^+, *J. Chem. Phys.* **126**, 104102, 2007.

[152] V. K. Voora, S. G. Balasubramani, and F. Furche: Variational generalized Kohn-Sham approach combining the random-phase-approximation and Green's-function methods, *Phys. Rev. A* **99**, 012518, 2019.

[153] C. A. Jimenez-Hoyos, B. G. Janesko, and G. E. Scuseria: Evaluation of Range-Separated Hybrid and Other Density Functional Approaches on Test Sets Relevant for Transition Metal-Based Homogeneous Catalysts, *J. Phys. Chem. A* **113**, 11742–11749, 2009.

[154] W. Jiang, N. J. DeYonker, and A. K. Wilson: Multireference Character for 3d Transition-Metal-Containing Molecules, *J. Chem. Theory Comput.* **8**, 460–468, 2012.

[155] J. P. Perdew, M. Ernzerhof, and K. Burke: Rationale for Mixing Exact Exchange with Density Functional Approximations, *J. Chem. Phys.* **105**, 9982, 1996.

[156] C. J. Stein, V. von Burg, and M. Reiher: The Delicate Balance of Static and Dynamic Electron Correlation, *J. Chem. Theory Comput.* **12**, 3764–3773, 2016.

[157] W. Klopper and H. P. Lüthi: Towards the Accurate Computation of Properties of Transition Metal Compounds: The Binding Energy of Ferrocene, *Chem. Phys. Lett.* **262**, 546–552, 1996.

[158] J. E. Bates, N. Sengupta, J. Sensenig, and A. Ruzsinszky: Adiabatic Connection without Coupling Constant Integration, *J. Chem. Theory Comput.* **14**, 2979–2990, 2018.

[159] M.-C. Kim, E. Sim, and K. Burke: Understanding and Reducing Errors in Density Functional Calculations, *Phys. Rev. Lett.* **111**, 073003, 2013.

[160] R. E. Connick: Oxidation states of the rare-earth and actinide elements, *J. Chem. Soc.* pp. S235–S241, 1949.

[161] A. J. Freeman and R. E. Watson: Theoretical Investigation of Some Magnetic and Spectroscopic Properties of Rare-Earth Ions, *Phys. Rev.* **127**, 2058–2075, 1962.

[162] P. B. Hitchcock, M. F. Lappert, L. Maron, and A. V. Protchenko: Lanthanum does form stable molecular compounds in the +2 oxidation state, *Angew. Chem. Int. Ed.* **47**, 1488–1491, 2008.

[163] M. R. MacDonald, J. E. Bates, M. E. Fieser, J. W. Ziller, F. Furche, and W. J. Evans: Expanding Rare-Earth Oxidation State Chemistry to Molecular Complexes of Holmium(II) and Erbium(II), *J. Am. Chem. Soc.* **134**, 8420–8423, 2012.

[164] M. R. MacDonald, J. E. Bates, J. W. Ziller, F. Furche, and W. J. Evans: Completing the Series of +2 Ions for the Lanthanide Elements: Synthesis of Molecular Complexes of Pr^{2+}, Gd^{2+}, Tb^{2+}, and Lu^{2+}, *J. Am. Chem. Soc.* **135**, 9857–9868, 2013.

[165] M. E. Fieser, M. R. MacDonald, B. T. Krull, J. E. Bates, J. W. Ziller, F. Furche, and W. J. Evans: Structural, spectroscopic, and theoretical comparison of traditional vs recently discovered Ln^{2+} ions in the [K(2.2.2-cryptand)][$(C_5H_4SiMe_3)_3Ln$] complexes: the variable nature of Dy^{2+} and Nd^{2+}, *J. Am. Chem. Soc.* **137**, 369–382, 2015.

[166] D. H. Woen and W. J. Evans: Handbook on the Physics and Chemistry of Rare Earths, volume 50, pp. 337–394, Elsevier, Amsterdam, 2016.

[167] W. J. Evans: Tutorial on the Role of Cyclopentadienyl Ligands in the Discovery of Molecular Complexes of the Rare-Earth and Actinide Metals in New Oxidation States, *Organometallics* **35**, 3088–3100, 2016.

[168] J. Su, C. J. Windorff, E. R. Batista, W. J. Evans, A. J. Gaunt, M. T. Janicke, S. A. Kozimor, B. L. Scott, D. H. Woen, and P. Yang: Identification of the Formal +2 Oxidation State of Neptunium: Synthesis and Structural Characterization of $\{Np^{II}[C_5H_3(SiMe_3)_2]_3\}^{1-}$, *J. Am. Chem. Soc.* **140**, 7425–7428, 2018.

[169] R. R. Langeslay, M. E. Fieser, J. W. Ziller, F. Furche, and W. J. Evans: Synthesis, structure, and reactivity of crystalline molecular complexes of the $\{[C_5H_3(SiMe_3)_2]_3Th\}^{1-}$ anion containing thorium in the formal +2 oxidation state, *Chem. Sci.* **6**, 517–521, 2015.

[170] M. R. MacDonald, M. E. Fieser, J. E. Bates, J. W. Ziller, F. Furche, and W. J. Evans: Identification of the +2 Oxidation State for Uranium in a Crystalline Molecular Complex, [K(2.2.2-cryptand)][$(C_5H_4SiMe_3)_3U$], *J. Am. Chem. Soc.* **135**, 13310–13313, 2013.

[171] H. S. La Pierre, A. Scheurer, F. W. Heinemann, W. Hieringer, and K. Meyer: Synthesis and characterization of a uranium(II) monoarene complex supported by delta backbonding, *Angew. Chem. Int. Ed.* **53**, 7158–7162, 2014.

[172] C. J. Windorff, G. P. Chen, J. N. Cross, W. J. Evans, F. Furche, A. J. Gaunt, M. T. Janicke, S. A. Kozimor, and B. L. Scott: Identification of the Formal +2 Oxidation State of Plutonium: Synthesis and Characterization of $\{Pu^{II}[C_5H_3(SiMe_3)_2]_3\}^{-}$, *J. Am. Chem. Soc.* **139**, 3970–3973, 2017.

[173] B. J. Burger, M. E. Thompson, W. D. Cotter, and J. E. Bercaw: Ethylene insertion and β-hydrogen elimination for permethylscandocene alkyl complexes. A study of the chain propagation and termination steps in Ziegler-Natta polymerization of ethylene, *J. Am. Chem. Soc.* **112**, 1566–1577, 1990.

[174] P. J. Shapiro, W. P. Schaefer, J. A. Labinger, J. E. Bercaw, and W. D. Cotter: Model Ziegler-Natta α-Olefin Polymerization Catalysts Derived from [{(η^5-C_5Me_4)$SiMe_2$(η^1-$NCMe_3$)}$(PMe_3)Sc(\mu_2\text{-}H)]_2$ and [{(η^5-C_5Me_4)$SiMe_2$(η^1-$NCMe_3$)}$Sc(\mu_2\text{-}CH_2CH_2CH_3)]_2$. Synthesis, Structures, and Kinetic and Equilibrium Investigations of the Catalytically Active Species in Solution, *J. Am. Chem. Soc.* **116**, 4623–4640, 1994.

[175] A. D. Sadow and T. D. Tilley: Homogeneous catalysis with methane. A strategy for the hydromethylation of olefins based on the nondegenerate exchange of alkyl groups and sigma-bond metathesis at scandium, *J. Am. Chem. Soc.* **125**, 7971–7977, 2003.

[176] A. D. Sadow and T. D. Tilley: Synthesis and Characterization of Scandium Silyl Complexes of the Type $Cp^*_2ScSiHRR'$. σ-Bond Metathesis Reactions and Catalytic Dehydrogenative Silation of Hydrocarbons, *J. Am. Chem. Soc.* **127**, 643–656, 2005.

[177] N. Barros, O. Eisenstein, L. Maron, and T. D. Tilley: DFT Investigation of the Catalytic Hydromethylation of Olefins by Scandocenes. 2. Influence of the Ansa Ligand on Propene and Isobutene Hydromethylation, *Organometallics* **27**, 2252–2257, 2008.

[178] S. Demir, S. E. Lorenz, M. Fang, F. Furche, G. Meyer, J. W. Ziller, and W. J. Evans: Synthesis, structure, and density functional theory analysis of a scandium dinitrogen complex, $[(C_5Me_4H)_2Sc]_2(\mu\text{-}\eta^2\text{:}\eta^2\text{-}N_2)$, *J. Am. Chem. Soc.* **132**, 11151–11158, 2010.

[179] F. G. N. Cloke, K. Khan, and R. N. Perutz: η-Arene complexes of scandium(0) and scandium(II), *J. Chem. Soc., Chem. Commun.* pp. 1372–1373, 1991.

[180] K. D. Khan: Sandwich Compounds of Scandium and the Early Transition Metals, dissertation, University of Sussex, UK, 1992.

[181] P. L. Arnold, F. G. N. Cloke, P. B. Hitchcock, and J. F. Nixon: The First Example of a Formal Scandium(I) Complex:Synthesis and Molecular Structure of a 22-Electron Scandium Triple Decker Incorporating the Novel 1,3,5-Triphosphabenzene Ring, *J. Am. Chem. Soc.* **118**, 7630–7631, 1996.

[182] G. K. B. Clentsmith, F. G. N. Cloke, J. C. Green, J. Hanks, P. B. Hitchcock, and J. F. Nixon: Stabilization of Low-Oxidation-State Early Transition-Metal Complexes Bearing 1,2,4-Triphosphacyclopentadienyl Ligands: Structure of $[\{Sc(P_3C_2tBu_2)_2\}_2]$; Sc^{II} or Mixed Oxidation State?, *Angew. Chem. Int. Ed.* **42**, 1038–1041, 2003.

[183] A. M. Neculai, D. Neculai, H. W. Roesky, J. Magull, M. Baldus, O. Andronesi, and M. Jansen: Stabilization of a Diamagnetic Sc^IBr Molecule in a Sandwich-Like Structure, *Organometallics* **21**, 2590–2592, 2002.

[184] P. L. Arnold, F. G. N. Cloke, and J. F. Nixon: The First Stable Scandocene: Synthesis and Characterisation of Bis(η-2,4,5-Tri-Tert-Butyl-1,3-Diphosphacyclopentadienyl)Scandium(II), *Chem. Commun.* **0**, 797–798, 1998.

[185] R. D. Shannon: Revised effective ionic radii and systematic studies of interatomic distances in halides and chalcogenides, *Acta Crystallogr. Sect. A* **32**, 751–767, 1976.

[186] J. K. Peterson, M. R. MacDonald, J. W. Ziller, and W. J. Evans: Synthetic Aspects of $(C_5H_4SiMe_3)_3Ln$ Rare-Earth Chemistry: Formation of $(C_5H_4SiMe_3)_3Lu$ via $[(C_5H_4SiMe_3)_2Ln]^+$Metallocene Precursors, *Organometallics* **32**, 2625–2631, 2013.

[187] J. L. Atwood and K. D. Smith: Nature of the scandium-carbon bond. II. Crystal and molecular structure of tricyclopentadienylscandium, *J. Am. Chem. Soc.* **95**, 1488–1491, 1973.

[188] J. S. Ghotra, M. B. Hursthouse, and A. J. Welch: Three-co-ordinate scandium(III) and europium(III); crystal and molecular structures of their trishexamethyldisilylamides, *J. Chem. Soc., Chem. Commun.* pp. 669–670, 1973.

[189] W. J. Evans, D. S. Lee, and J. W. Ziller: Reduction of dinitrogen to planar bimetallic $M_2(\mu\text{-}\eta^2\text{:}\eta^2\text{-}N_2)$ complexes of Y, Ho, Tm, and Lu using the $K/Ln[N(SiMe_3)_2]_3$ reduction system, *J. Am. Chem. Soc.* **126**, 454–455, 2004.

[190] W. J. Evans, D. S. Lee, D. B. Rego, J. M. Perotti, S. A. Kozimor, E. K. Moore, and J. W. Ziller: Expanding Dinitrogen Reduction Chemistry to Trivalent Lanthanides via the LnZ_3/Alkali Metal Reduction System: Evaluation of the Generality of Forming $Ln_2(\mu\text{-}\eta^2\text{:}\eta^2\text{-}N_2)$ Complexes via LnZ_3/K, *J. Am. Chem. Soc.* **126**, 14574–14582, 2004.

[191] W. J. Evans, D. B. Rego, and J. W. Ziller: Synthesis, Structure, and ^{15}N NMR Studies of Paramagnetic Lanthanide Complexes Obtained by Reduction of Dinitrogen, *Inorg. Chem.* **45**, 10790–10798, 2006.

[192] M. Fang, J. E. Bates, S. E. Lorenz, D. S. Lee, D. B. Rego, J. W. Ziller, F. Furche, and W. J. Evans: $(N_2)^{3-}$ Radical Chemistry via Trivalent Lanthanide Salt/Alkali Metal Reduction of Dinitrogen: New Syntheses and Examples of $(N_2)^{2-}$ and $(N_2)^{3-}$ Complexes and Density Functional Theory Comparisons of Closed Shell Sc^{3+}, Y^{3+}, and Lu^{3+} Versus $4f^9$ Dy^{3+}, *Inorg. Chem.* **50**, 1459–1469, 2011.

[193] M. E. Fieser: Spectroscopic and Computational Analysis of Rare Earth and Actinide Complexes in Unusual Coordination Environments and Oxidation States, dissertation, University of California, Irvine, 2015.

[194] M. Fang, D. S. Lee, J. W. Ziller, R. J. Doedens, J. E. Bates, F. Furche, and W. J. Evans: Synthesis of the $(N_2)^{3-}$ radical from Y^{2+} and its protonolysis reactivity to form $(N_2H_2)^{2-}$ via the $Y[N(SiMe_3)_2]_3/KC_8$ reduction system, *J. Am. Chem. Soc.* **133**, 3784–3787, 2011.

[195] D. H. Woen, G. P. Chen, J. W. Ziller, T. J. Boyle, F. Furche, and W. J. Evans: Solution Synthesis, Structure, and CO_2 Reduction Reactivity of a Scandium(II) Complex, $\{Sc[N(SiMe_3)_2]_3\}^-$, *Angew. Chem. Int. Ed.* **56**, 2050–2053, 2017.

[196] A. Klamt and G. Schüürmann: COSMO: A New Approach to Dielectric Screening in Solvents With Explicit Expressions for the Screening Energy and Its Gradient, *J. Chem. Soc., Perkin Trans. 2* pp. 799–805, 1993.

[197] D. R. Lide, editor: CRC Handbook of Chemistry and Physics, volume 88, chapter 8, p. 136, CRC Press, Boca Raton, Fl, 2008.

[198] D. R. Lide, editor: CRC Handbook of Chemistry and Physics, volume 88, chapter 3, p. 474, CRC Press, Boca Raton, Fl, 2008.

[199] F. Furche, B. T. Krull, B. D. Nguyen, and J. Kwon: Accelerating molecular property calculations with nonorthonormal Krylov space methods, *J. Chem. Phys.* **144**, 174105, 2016.

[200] J. E. Bates and F. Furche: Harnessing the meta-generalized gradient approximation for time-dependent density functional theory, *J. Chem. Phys.* **137**, 164105, 2012.

[201] R. Send, M. Kühn, and F. Furche: Assessing Excited State Methods by Adiabatic Excitation Energies, *J. Chem. Theory Comput.* **7**, 2376–2386, 2011.

[202] J. Chatt, J. R. Dilworth, and R. L. Richards: Recent advances in the chemistry of nitrogen fixation, *Chem. Rev.* **78**, 589–625, 1978.

[203] P. J. Chirik: Dinitrogen functionalization with bis(cyclopentadienyl) complexes of zirconium and hafnium, *Dalton Trans.* pp. 16–25, 2007.

[204] R. R. Schrock: Catalytic reduction of dinitrogen to ammonia by molybdenum: theory versus experiment, *Angew. Chem. Int. Ed.* **47**, 5512–5522, 2008.

[205] M. D. Fryzuk: Side-on end-on bound dinitrogen: an activated bonding mode that facilitates functionalizing molecular nitrogen, *Acc. Chem. Res.* **42**, 127–133, 2009.

[206] J. L. Crossland and D. R. Tyler: Iron–dinitrogen coordination chemistry: Dinitrogen activation and reactivity, *Coord. Chem. Rev.* **254**, 1883–1894, 2010.

[207] Y. Tanabe and Y. Nishibayashi: Developing more sustainable processes for ammonia synthesis, *Coord. Chem. Rev.* **257**, 2551–2564, 2013.

[208] A. J. Keane, B. L. Yonke, M. Hirotsu, P. Y. Zavalij, and L. R. Sita: Fine-tuning the energy barrier for metal-mediated dinitrogen N identical withN bond cleavage, *J. Am. Chem. Soc.* **136**, 9906–9909, 2014.

[209] S. F. McWilliams and P. L. Holland: Dinitrogen binding and cleavage by multinuclear iron complexes, *Acc. Chem. Res.* **48**, 2059–2065, 2015.

[210] R. J. Burford, A. Yeo, and M. D. Fryzuk: Dinitrogen activation by group 4 and group 5 metal complexes supported by phosphine-amido containing ligand manifolds, *Coord. Chem. Rev.* **334**, 84–99, 2017.

[211] R. J. Burford and M. D. Fryzuk: Examining the Relationship Between Coordination Mode and Reactivity of Dinitrogen, *Nat. Rev. Chem.* **1**, 0026, 2017.

[212] K. Jonas: π-Bonded Nitrogen in a Crystalline Nickel-Lithium Complex, *Angew. Chem. Int. Ed.* **12**, 997–998, 1973.

[213] K. Jonas, D. J. Brauer, C. Krueger, P. J. Roberts, and Y. H. Tsay: ''Side-On'' Dinitrogen-Transition Metal Complexes. The Molecular Structure of $\{C_6H_5[Na.O(C_2H_5)_2]_2[(C_6H_5)_2Ni]_2N_2NaLi_6(OC_2H_5)_4.O(C_2H_5)_2\}_2$, *J. Am. Chem. Soc.* **98**, 74–81, 1976.

[214] C. Krüger and Y.-H. Tsay: Molecular Structure of a π-Dinitrogen-Nickel-Lithium Complex, *Angew. Chem. Int. Ed.* **12**, 998–999, 1973.

[215] W. J. Evans, T. A. Ulibarri, and J. W. Ziller: Isolation and X-Ray Crystal Structure of the First Dinitrogen Complex of an F-Element Metal, $[(C_5Me_5)_2Sm]_2N_2$, *J. Am. Chem. Soc.* **110**, 6877–6879, 1988.

[216] W. J. Evans and D. S. Lee: Early developments in lanthanide-based dinitrogen reduction chemistry, *Can. J. Chem.* **83**, 375–384, 2005.

[217] E. Campazzi, E. Solari, C. Floriani, and R. Scopelliti: The fixation and reduction of dinitrogen using lanthanides: praseodymium and neodymium meso-octaethylporphyrinogen–dinitrogen complexes, *Chem. Commun.* pp. 2603–2604, 1998.

[218] J. Guan, Dubé, S. Gambarotta, and G. P. A. Yap: Dinitrogen Labile Coordination versus Four-Electron Reduction, THF Cleavage, and Fragmentation Promoted by a (calix-tetrapyrrole)Sm(II) Complex, *Organometallics* **19**, 4820–4827, 2000.

[219] F. Jaroschik, A. Momin, F. Nief, X.-F. Le Goff, G. B. Deacon, and P. C. Junk: Dinitrogen Reduction and C–H Activation by the Divalent Organoneodymium Complex $[(C_5H_2t\mathrm{Bu}_3)_2\mathrm{Nd}(\mu\text{-I})\mathrm{K}([18]\text{crown-6})]$, *Angew. Chem. Int. Ed.* **48**, 1117–1121, 2009.

[220] M. E. Fieser, D. H. Woen, J. F. Corbey, T. J. Mueller, J. W. Ziller, and W. J. Evans: Raman spectroscopy of the N–N bond in rare earth dinitrogen complexes, *Dalton Trans.* **45**, 14634–14644, 2016.

[221] S. M. Mansell, J. H. Farnaby, A. I. Germeroth, and P. L. Arnold: Thermally Stable Uranium Dinitrogen Complex with Siloxide Supporting Ligands, *Organometallics* **32**, 4214–4222, 2013.

[222] F. G. N. Cloke and P. B. Hitchcock: Reversible Binding and Reduction of Dinitrogen by a Uranium(III) Pentalene Complex, *J. Am. Chem. Soc.* **124**, 9352–9353, 2002.

[223] P. Roussel and P. Scott: σ-Complex of Dinitrogen with Trivalent Uranium, *J. Am. Chem. Soc.* **120**, 1070–1071, 1998.

[224] B. A. MacKay and M. D. Fryzuk: Dinitrogen coordination chemistry: on the biomimetic borderlands, *Chem. Rev.* **104**, 385–401, 2004.

[225] V. M. E. Bates, G. K. B. Clentsmith, F. G. N. Cloke, J. C. Green, and H. D. L. Jenkin: Theoretical investigation of the pathway for reductive cleavage of dinitrogen by a vanadium diamidoamine complex, *Chem. Commun.* pp. 927–928, 2000.

[226] D. H. Woen, G. P. Chen, J. W. Ziller, T. J. Boyle, F. Furche, and W. J. Evans: End-On Bridging Dinitrogen Complex of Scandium, *J. Am. Chem. Soc.* **139**, 14861–14864, 2017.

[227] S. Grimme: Semiempirical GGA-type density functional constructed with a long-range dispersion correction, *J. Comput. Chem.* **27**, 1787–1799, 2006.

[228] A. Schäfer, H. Horn, and R. Ahlrichs: Fully optimized contracted Gaussian basis sets for atoms Li to Kr, *J. Chem. Phys.* **97**, 2571, 1992.

[229] P. Deglmann, K. May, F. Furche, and R. Ahlrichs: Nuclear second analytical derivative calculations using auxiliary basis set expansions, *Chem. Phys. Lett.* **384**, 103–107, 2004.

[230] D. O. Kashinski, G. M. Chase, R. G. Nelson, O. E. Di Nallo, A. N. Scales, D. L. VanderLey, and E. F. C. Byrd: Harmonic Vibrational Frequencies: Approximate Global Scaling Factors for TPSS, M06, and M11 Functional Families Using Several Common Basis Sets, *J. Phys. Chem. A* **121**, 2265–2273, 2017.

[231] C. Adamo and V. Barone: Toward reliable density functional methods without adjustable parameters: The PBE0 model, *J. Chem. Phys.* **110**, 6158–6170, 1999.

[232] D. Rappoport and F. Furche: Property-optimized gaussian basis sets for molecular response calculations, *J. Chem. Phys.* **133**, 134105, 2010.

[233] J. J. Curley, T. R. Cook, S. Y. Reece, P. Muller, and C. C. Cummins: Shining light on dinitrogen cleavage: structural features, redox chemistry, and photochemistry of the key intermediate bridging dinitrogen complex, *J. Am. Chem. Soc.* **130**, 9394–9405, 2008.

[234] J. M. Smith, A. R. Sadique, T. R. Cundari, K. R. Rodgers, G. Lukat-Rodgers, R. J. Lachicotte, C. J. Flaschenriem, J. Vela, and P. L. Holland: Studies of low-coordinate iron dinitrogen complexes, *J. Am. Chem. Soc.* **128**, 756–769, 2006.

[235] J. M. de Wolf, R. Blaauw, A. Meetsma, J. H. Teuben, R. Gyepes, V. Varga, K. Mach, N. Veldman, and A. L. Spek: Bis(tetramethylcyclopentadienyl)titanium Chemistry. Molecular Structures of $[(C_5HMe_4)(\mu\text{-}\eta^1{:}\eta^5\text{-}C_5Me_4)Ti]_2$and $[(C_5HMe_4)_2Ti]_2N_2$, *Organometallics* **15**, 4977–4983, 1996.

[236] T. E. Hanna, W. H. Bernskoetter, M. W. Bouwkamp, E. Lobkovsky, and P. J. Chirik: Bis(cyclopentadienyl) Titanium Dinitrogen Chemistry: Synthesis and Characterization of a Side-on Bound Haptomer, *Organometallics* **26**, 2431–2438, 2007.

[237] S. P. Semproni, C. Milsmann, and P. J. Chirik: Side-on Dinitrogen Complexes of Titanocenes with Disubstituted Cyclopentadienyl Ligands: Synthesis, Structure, and Spectroscopic Characterization, *Organometallics* **31**, 3672–3682, 2012.

[238] J. M. Manriquez and J. E. Bercaw: Preparation of a dinitrogen complex of bis(pentamethylcyclopentadienyl)zirconium(II). Isolation and protonation leading to stoichiometric reduction of dinitrogen to hydrazine, *J. Am. Chem. Soc.* **96**, 6229–6230, 1974.

[239] J. A. Pool and P. J. Chirik: The importance of cyclopentadienyl substituent effects in group 4 metallocene dinitrogen chemistry, *Can. J. Chem.* **83**, 286–295, 2005.

[240] G. T. Seaborg, E. M. Mcmillan, J. W. Kennedy, and A. C. Wahl: Radioactive Element 94 from Deuterons on Uranium, *Phys. Rev.* **69**, 366–367, 1946.

[241] L. R. Morss, N. M. Edelstein, J. Fuger, J. J. Katz, and L. Morss: The chemistry of the actinide and transactinide elements, volume 1, Springer, 2006.

[242] M. B. Jones and A. J. Gaunt: Recent developments in synthesis and structural chemistry of nonaqueous actinide complexes, *Chem. Rev.* **113**, 1137–1198, 2013.

[243] T. W. Hayton: Recent developments in actinide-ligand multiple bonding, *Chem. Commun.* **49**, 2956–2973, 2013.

[244] S. A. Johnson and S. C. Bart: Achievements in uranium alkyl chemistry: celebrating sixty years of synthetic pursuits, *Dalton Trans.* **44**, 7710–7726, 2015.

[245] S. T. Liddle: The Renaissance of Non-Aqueous Uranium Chemistry, *Angew. Chem. Int. Ed.* **54**, 8604–8641, 2015.

[246] M. Ephritikhine: The vitality of uranium molecular chemistry at the dawn of the XXIst century, *Dalton Trans.* pp. 2501–2516, 2006.

[247] A. J. Gaunt and M. P. Neu: Recent developments in nonaqueous plutonium coordination chemistry, *C. R. Chim.* **13**, 821–831, 2010.

[248] Information about the Cambridge Structural Database can be found at `http://ccdc.cam.ac.uk/products/csd/`. This citation is based on depositions up to and including the November 2016 update.

[249] J. W. Ward: Electronic structure and bonding in transuranics: Comparison with lanthanides, *Less-Common Met.* **93**, 279–292, 1983.

[250] N. B. Mikheev: Divalent plutonium: certain properties, *Inorg. Chim. Acta* **140**, 177–180, 1987.

[251] J. K. Gibson, R. G. Haire, M. Santos, J. Marcalo, and A. Pires de Matos: Oxidation Studies of Dipositive Actinide Ions, An^{2+} (An = Th, U, Np, Pu, Am) in the Gas Phase: Synthesis and Characterization of the Isolated Uranyl, Neptunyl, and Plutonyl Ions UO_2^{2+}(g), NpO_2^{2+}(g), and PuO_2^{2+}(g), *J. Phys. Chem. A* **109**, 2768–2781, 2005.

[252] W. Küchle, M. Dolg, H. Stoll, and H. Preuss: Energy-adjusted pseudopotentials for the actinides. Parameter sets and test calculations for thorium and thorium monoxide, *J. Chem. Phys.* **100**, 7535, 1994.

[253] X. Cao and M. Dolg: Segmented contraction scheme for small-core actinide pseudopotential basis sets, *J. Mol. Struct. (Theochem)* **673**, 203–209, 2004.

[254] Q.-Y. Wu, J.-H. Lan, C.-Z. Wang, Z.-P. Cheng, Z.-F. Chai, J. K. Gibson, and W.-Q. Shi: Paving the way for the synthesis of a series of divalent actinide complexes: a theoretical perspective, *Dalton Trans.* **45**, 3102–3110, 2016.

[255] L. R. Avens, S. G. Bott, D. L. Clark, A. P. Sattelberger, J. G. Watkin, and B. D. Zwick: A Convenient Entry into Trivalent Actinide Chemistry: Synthesis and Characterization of $AnI_3(THF)_4$ and $An[N(SiMe_3)_2]_3$ (An = U, Np, Pu), *Inorg. Chem.* **33**, 2248–2256, 1994.

[256] G. Meyer: Superbulky ligands and trapped electrons: new perspectives in divalent lanthanide chemistry, *Angew. Chem. Int. Ed.* **47**, 4962–4964, 2008.

[257] M. Pepper and B. E. Bursten: The electronic structure of actinide-containing molecules: a challenge to applied quantum chemistry, *Chem. Rev.* **91**, 719–741, 1991.

[258] B. O. Roos and P.-Å. Malmqvist: Relativistic quantum chemistry: the multiconfigurational approach, *Phys. Chem. Chem. Phys.* **6**, 2919–2927, 2004.

[259] N. Kaltsoyannis: Does Covalency Increase or Decrease across the Actinide Series? Implications for Minor Actinide Partitioning, *Inorg. Chem.* **52**, 3407–3413, 2013.

[260] M. L. Neidig, D. L. Clark, and R. L. Martin: Covalency in *f*-element complexes, *Coord. Chem. Rev.* **257**, 394 – 406, 2013.

[261] J.-B. Liu, G. P. Chen, W. Huang, D. L. Clark, W. H. E. Schwarz, and J. Li: Bonding trends across the series of tricarbonato-actinyl anions $[(AnO_2)(CO_3)_3]^{4-}$ (An = U–Cm): the plutonium turn, *Dalton Trans.* **46**, 2542–2550, 2017.

[262] N. Kaltsoyannis: Transuranic Computational Chemistry, *Chem. Eur. J.* **24**, 2815–2825, 2018.

[263] M. E. Fieser, T. J. Mueller, J. E. Bates, J. W. Ziller, F. Furche, and W. J. Evans: Differentiating Chemically Similar Lewis Acid Sites in Heterobimetallic Complexes: The Rare-Earth Bridged Hydride $(C_5Me_5)_2Ln(\mu\text{-}H)_2Ln'(C_5Me_5)_2$ and Tuckover Hydride $(C_5Me_5)_2Ln(\mu\text{-}H)(\mu\text{-}\eta^1{:}\eta^5\text{-}CH_2C_5Me_4)Ln'(C_5Me_5)$ Systems, *Organometallics* **33**, 3882–3890, 2014.

[264] J. E. Bates: Random Phase Approximation Renormalization: Theory, Implementation, and Applications to Lanthanide Chemistry, dissertation, University of California, Irvine, 2013.

[265] A. M. Burow, J. E. Bates, F. Furche, and H. Eshuis: Analytical First-Order Molecular Properties and Forces within the Adiabatic Connection Random Phase Approximation, *J. Chem. Theory Comput.* **10**, 180–194, 2014.

[266] M. Kühn: Correlation Energies from the Two-Component Random Phase Approximation, *J. Chem. Theory Comput.* **10**, 623–633, 2014.

[267] A. J. Ryan, L. E. Darago, S. G. Balasubramani, G. P. Chen, J. W. Ziller, F. Furche, J. R. Long, and W. J. Evans: Synthesis, Structure, and Magnetism of Tris(amide) $[Ln\{N(SiMe_3)_2\}_3]^{1-}$ Complexes of the Non-traditional +2 Lanthanide Ions, *Chem. Eur. J.* **24**, 7702–7709, 2018.

[268] N. J. Higham: Functions of Matrices: Theory and Computation, Society for Industrial and Applied Mathematics, Philadelphia, 2008.

[269] K. Löwner: Über monotone Matrixfunktionen, *Math. Z.* **38**, 177–216, 1934.

[270] R. Bhatia: Matrix Analysis, Graduate Texts in Mathematics, Springer, New York, 1997.

[271] H. Heuser: Functional Analysis, John Wiley & Sons, Inc., New York, 1982.

Appendix A

Analysis of the Plasmonic Hessian

A.1 Definition of T

As stated in Section 1.3.2, $\mathbf{T}$ is defined as the first-order term of $(\mathbf{M}_\alpha^{\mathrm{RPA}})^{1/2}$ with respect to α,

$$\mathbf{T} = \left.\frac{\mathrm{d}(\mathbf{M}_\alpha^{\mathrm{RPA}})^{1/2}}{\mathrm{d}\alpha}\right|_{\alpha=0}. \tag{A.1}$$

To derive the expression of $\mathbf{T}$, it is convenient to introduce a few notations.

Definition A.1.

$$\mathbf{F} : \mathbb{R} \to \mathbb{C}^{N_h N_p \times N_h N_p}$$
$$\alpha \mapsto \mathbf{M}_\alpha^{RPA}.$$

Definition A.2. *The matrix square root function,*

$$g : \mathbb{C}^{N_h N_p \times N_h N_p} \to \mathbb{C}^{N_h N_p \times N_h N_p}$$
$$\mathbf{X} \mapsto \mathbf{X}^{1/2}.$$

Therefore, $g \circ \mathbf{F} : \alpha \mapsto (\mathbf{M}_\alpha^{\mathrm{RPA}})^{1/2}$. We use the symbol D to denote derivatives or Fréchet derivatives in the case of matrix functions, i.e.,

$$D\mathbf{F} = \frac{\mathrm{d}\mathbf{F}}{\mathrm{d}\alpha},$$

and

$$Dg : \mathbb{C}^{N_\mathrm{h} N_\mathrm{p} \times N_\mathrm{h} N_\mathrm{p}} \to \mathcal{L}(\mathbb{C}^{N_\mathrm{h} N_\mathrm{p} \times N_\mathrm{h} N_\mathrm{p}}, \mathbb{C}^{N_\mathrm{h} N_\mathrm{p} \times N_\mathrm{h} N_\mathrm{p}})$$
$$\mathbf{X} \mapsto Dg(\mathbf{X}),$$

where $\mathcal{L}(U, V)$ denotes the set of linear mappings from U to V.

By the properties of the Fréchet derivative of the matrix square root function (see, e.g., Reference [268]), it is readily shown that

$$\mathbf{X}^{1/2} Dg(\mathbf{X})(\mathbf{E}) + Dg(\mathbf{X})(\mathbf{E})\mathbf{X}^{1/2} = \mathbf{E}, \tag{A.2}$$

where $\mathbf{E} \in \mathbb{C}^{N_\mathrm{h} N_\mathrm{p} \times N_\mathrm{h} N_\mathrm{p}}$. Moreover, by the chain rule,

$$\left.\frac{\mathrm{d}(\mathbf{M}_\alpha^{\mathrm{RPA}})^{1/2}}{\mathrm{d}\alpha}\right|_{\alpha=0} = D(g \circ \mathbf{F})(0) = Dg(\mathbf{F}(0))(D\mathbf{F}(0)). \tag{A.3}$$

By definition,

$$\mathbf{F}(0) = \mathbf{M}_\alpha^{\mathrm{RPA}}\big|_{\alpha=0} = \mathbf{D}^2, \tag{A.4}$$

and

$$D\mathbf{F}(0) = 2\mathbf{D}^{1/2}\mathbf{B}^{\mathrm{H}}\mathbf{D}^{1/2}. \tag{A.5}$$

Combining Equations (A.1)–(A.5), we have

$$\mathbf{DT} + \mathbf{TD} = 2\mathbf{D}^{1/2}\mathbf{B}^{\mathrm{H}}\mathbf{D}^{1/2}. \tag{A.6}$$

Given that $\mathbf{D}$ is diagonal, we arrive at the following expression of $\mathbf{T}$,

$$T_{iajb} = \frac{2D_{iaia}^{1/2}B_{iajb}^{\mathrm{H}}D_{jbjb}^{1/2}}{D_{iaia} + D_{jbjb}} \tag{A.7}$$

A.2 Positive Definiteness of the Plasmonic Hessian

$\mathbf{M}^{\mathrm{RPA}}$, $\mathbf{D}$, $\mathbf{T}$ and the plasmonic Hessian $\mathbf{W}^{\mathrm{p}}$ are matrices defined in Section 1.3.2. For Hermitian matrices $\mathbf{X}$ and $\mathbf{Y}$, we use $\mathbf{X} > \mathbf{Y}$ to denote that $\mathbf{X} - \mathbf{Y}$ is positive definite.

Theorem A.1. *if* $\mathbf{X} > \mathbf{Y} > \mathbf{0}$*, then* $\mathbf{X}^{1/2} > \mathbf{Y}^{1/2}$

Proof. This is a corollary of the Löwner–Heinz inequality [269]. See also Section V.1 in Reference [270]. □

Theorem A.2. $(\mathbf{D} + \mathbf{T})^2 > \mathbf{M}^{RPA} > \mathbf{0}$.

Proof. It is readily shown that $\mathbf{M}^{\mathrm{RPA}}$, $\mathbf{D}$, and $\mathbf{T}$ are all positive definite. By Equation (A.6) and the definition of $\mathbf{M}^{\mathrm{RPA}}$, we have

$$(\mathbf{D} + \mathbf{T})^2 = \mathbf{D}^2 + \mathbf{DT} + \mathbf{TD} + \mathbf{T}^2 = \mathbf{M}^{\mathrm{RPA}} + \mathbf{T}^2. \tag{A.8}$$

Since $\mathbf{T}$ is Hermitian, $\mathbf{T}^2 > 0$. Therefore, $(\mathbf{D} + \mathbf{T})^2 > \mathbf{M}^{\mathrm{RPA}}$. □

Theorem A.3. *The plasmonic Hessian* $\mathbf{W}^p$ *is positive definite.*

Proof. By Theorems A.1 and A.2,

$$\mathbf{D} + \mathbf{T} > (\mathbf{M}^{\mathrm{RPA}})^{1/2}. \tag{A.9}$$

Thus, $\mathbf{W}^{\mathrm{p}} = \mathbf{D} + \mathbf{T} - (\mathbf{M}^{\mathrm{RPA}})^{1/2} > \mathbf{0}$. □

Appendix B

Variational Boundedness of RI-RPA Correlation Energy

In this appendix, we prove without neglecting the RI error in the direct ring-CCD amplitude that the RI-RPA correlation energy $\tilde{E}^{\text{C RPA}}$ is an upper bound of the exact RPA correlation energy $E^{\text{C RPA}}$. Throughout the proof, tildes denote quantities with the RI approximation, while quantities without tildes are associated with the full-rank representation.

The RI counterpart of Equation (1.35) can be written as

$$\tilde{\mathbf{B}}^{\text{H}} = \tilde{\mathbf{S}}\tilde{\mathbf{S}}^{\text{T}}, \tag{B.1}$$

where

$$\tilde{S}_{iaP} = (ia|\bar{P}) = \sum_{Q}(ia|Q)[\mathbf{L}^{-1}]_{QP}. \tag{B.2}$$

$P, Q, \ldots$ denote auxiliary basis functions of dimension N_{aux}; the bar notation denotes orthogonalized vectors in the space with an inner product defined by the Coulomb integrals.

$\tilde{\mathbf{S}}$ is related to the full-rank $\mathbf{S}$ defined in Equation (1.35) through a matrix $\mathbf{U}$:

$$\tilde{\mathbf{S}} = \mathbf{S}\mathbf{U}. \tag{B.3}$$

Using the singular value decomposition of $\mathbf{S}$, it is readily shown that

$$\mathbf{U}^{\mathrm{T}}\mathbf{U} = \tilde{\mathbf{S}}^{\mathrm{T}}(\mathbf{B}^{\mathrm{H}})^{-1}\tilde{\mathbf{S}}. \tag{B.4}$$

Defining

$$|\bar{ia}) = \sum_{jb} |jb)[\mathbf{S}^{-1}]_{jbia}, \tag{B.5}$$

we see that

$$[\mathbf{U}^{\mathrm{T}}\mathbf{U}]_{PQ} = \sum_{ia} (\bar{P}|\bar{ia})(\bar{ia}|\bar{Q}). \tag{B.6}$$

Lemma B.1. *For any N_{aux}-dimensional unit vector $\mathbf{v}$,*

$$\mathbf{v}^{\mathrm{T}}\mathbf{U}^{\mathrm{T}}\mathbf{U}\mathbf{v} \leq 1. \tag{B.7}$$

Proof. Since the $\{|\bar{P})\}$ are orthonormal,

$$\begin{aligned}
\mathbf{v}^{\mathrm{T}}\mathbf{U}^{\mathrm{T}}\mathbf{U}\mathbf{v} &= \sum_{PQ}\sum_{ia} v_P(\bar{P}|\bar{ia})(\bar{ia}|\bar{Q})v_Q && \text{(B.8)}\\
&\leq \sum_{PQ} v_P(\bar{P}|\bar{Q})v_Q && \text{(B.9)}\\
&= \sum_{P} v_P v_P && \text{(B.10)}\\
&= 1 && \text{(B.11)}
\end{aligned}$$

□

Theorem B.2. *Let* $q_1(\omega) \leq \cdots \leq q_{N_h N_p}(\omega)$ *and* $\tilde{q}_1(\omega) \leq \cdots \leq \tilde{q}_{N_{aux}}(\omega)$ *be the eigenvalues of* $\mathbf{Q}(\omega)$ *and* $\tilde{\mathbf{Q}}(\omega)$*, respectively. They satisfy*

$$0 \leq \tilde{q}_P(\omega) \leq q_{N_h N_p - N_{aux} + P}(\omega) \tag{B.12}$$

for $1 \leq P \leq N_{aux}$.

Proof. By definition, Equation (1.41), $\tilde{\mathbf{Q}}(\omega)$ is related to $\mathbf{Q}(\omega)$ through

$$\tilde{\mathbf{Q}}(\omega) = \mathbf{U}^{\mathrm{T}} \mathbf{Q}(\omega) \mathbf{U}. \tag{B.13}$$

Denote the eigenvectors of $\tilde{\mathbf{Q}}(\omega)$ corresponding to $\{\tilde{q}_P(\omega)\}_{1 \leq P \leq N_{\mathrm{aux}}}$ as $\{\tilde{\mathbf{v}}_P\}_{1 \leq P \leq N_{\mathrm{aux}}}$, which are orthonormal. Define $\tilde{\mathcal{V}}_P = \operatorname{span}\{\tilde{\mathbf{v}}_P, \ldots, \tilde{\mathbf{v}}_{N_{\mathrm{aux}}}\}$. By the Courant–Fischer min-max theorem (see, e.g. Reference [271]), for $1 \leq P \leq N_{\mathrm{aux}}$,

$$\begin{aligned}
q_{N_{\mathrm{h}} N_{\mathrm{p}} - N_{\mathrm{aux}} + P}(\omega) &= \max_{\mathcal{V}} \left\{ \min_{\mathbf{v}} \left\{ \frac{\mathbf{v}^{\mathrm{T}} \mathbf{Q}(\omega) \mathbf{v}}{\mathbf{v}^{\mathrm{T}} \mathbf{v}} \middle| \mathbf{v} \neq \mathbf{0},\, \mathbf{v} \in \mathcal{V} \right\} \middle| \dim \mathcal{V} = N_{\mathrm{aux}} - P + 1 \right\} \\
&\geq \min_{\tilde{\mathbf{v}}} \left\{ \frac{(\mathbf{U}\tilde{\mathbf{v}})^{\mathrm{T}} \mathbf{Q}(\omega) (\mathbf{U}\tilde{\mathbf{v}})}{(\mathbf{U}\tilde{\mathbf{v}})^{\mathrm{T}} (\mathbf{U}\tilde{\mathbf{v}})} \middle| \tilde{\mathbf{v}} \neq \mathbf{0},\, \tilde{\mathbf{v}} \in \tilde{\mathcal{V}}_P \right\} \\
&\geq \min_{\tilde{\mathbf{v}}} \left\{ \tilde{\mathbf{v}}^{\mathrm{T}} \mathbf{U}^{\mathrm{T}} \mathbf{Q}(\omega) \mathbf{U} \tilde{\mathbf{v}} \middle| \tilde{\mathbf{v}} \neq \mathbf{0},\, \tilde{\mathbf{v}} \in \tilde{\mathcal{V}}_P \right\} \\
&= \min_{\tilde{\mathbf{v}}} \left\{ \tilde{\mathbf{v}}^{\mathrm{T}} \tilde{\mathbf{Q}}(\omega) \tilde{\mathbf{v}} \middle| \tilde{\mathbf{v}} \neq \mathbf{0},\, \tilde{\mathbf{v}} \in \tilde{\mathcal{V}}_P \right\} \\
&= \tilde{q}_P(\omega)
\end{aligned}$$

Moreover, since $\tilde{\mathbf{Q}}(\omega)$ is positive semidefinite, $\tilde{q}_P(\omega) \geq 0$ for $1 \leq P \leq N_{\mathrm{aux}}$. □

Theorem B.3. $E^{C\ RPA} \leq \tilde{E}^{C\ RPA}$.

Proof. The RPA correlation energy, Equation (1.46), may be rewritten as

$$E^{\text{C RPA}} = \frac{1}{2\pi} \int_0^\infty d\omega \sum_{P=1}^{N_\text{h} N_\text{p}} g(q_P(\omega)), \tag{B.14}$$

where g is defined on $[0, \infty)$ by $g(x) = \ln(1+x) - x$. Since g is non-positive and monotonically decreasing, we see that

$$\begin{aligned} E^{\text{C RPA}} &\leq \frac{1}{2\pi} \int_0^\infty d\omega \sum_{P=1}^{N_\text{aux}} g(q_{N_\text{h} N_\text{p} - N_\text{aux} + P}(\omega)) && \text{(B.15)} \\ &\leq \frac{1}{2\pi} \int_0^\infty d\omega \sum_{P=1}^{N_\text{aux}} g(\tilde{q}_P(\omega)) && \text{(B.16)} \\ &= \tilde{E}^{\text{C RPA}}. && \text{(B.17)} \end{aligned}$$

□